

Spring 2010

# A micro-transponder for precision tracking of underwater targets

Albert Whitaker Franzheim III.  
*University of New Hampshire, Durham*

Follow this and additional works at: <https://scholars.unh.edu/thesis>

---

## Recommended Citation

Franzheim, Albert Whitaker III., "A micro-transponder for precision tracking of underwater targets" (2010). *Master's Theses and Capstones*. 544.  
<https://scholars.unh.edu/thesis/544>

This Thesis is brought to you for free and open access by the Student Scholarship at University of New Hampshire Scholars' Repository. It has been accepted for inclusion in Master's Theses and Capstones by an authorized administrator of University of New Hampshire Scholars' Repository. For more information, please contact [nicole.hentz@unh.edu](mailto:nicole.hentz@unh.edu).

**A MICRO-TRANSPONDER  
FOR PRECISION TRACKING OF UNDERWATER TARGETS**

BY

ALBERT WHITAKER FRANZHEIM, III  
BS in Electrical Engineering, University of New Hampshire, 2006

THESIS

Submitted to the University of New Hampshire  
in Partial Fulfillment of  
the Requirements for the Degree of

Master of Science  
in  
Electrical Engineering

May, 2010

UMI Number: 1485424

All rights reserved

**INFORMATION TO ALL USERS**

The quality of this reproduction is dependent upon the quality of the copy submitted.

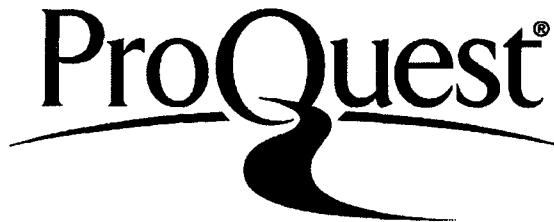
In the unlikely event that the author did not send a complete manuscript and there are missing pages, these will be noted. Also, if material had to be removed, a note will indicate the deletion.



UMI 1485424

Copyright 2010 by ProQuest LLC.

All rights reserved. This edition of the work is protected against unauthorized copying under Title 17, United States Code.



ProQuest LLC  
789 East Eisenhower Parkway  
P.O. Box 1346  
Ann Arbor, MI 48106-1346

ALL RIGHTS RESERVED

© 2010

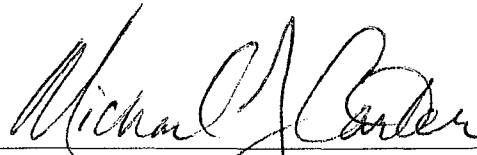
Albert Whitaker Franzheim, III

This thesis has been examined and approved.




---

Thesis Director, Dr. Christian de Moustier  
Professor of Electrical and Computer Engineering



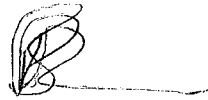
---

Dr. Michael J. Carter  
Associate Professor of Electrical and Computer Engineering



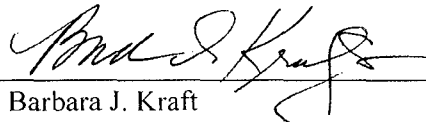
---

Dr. Paul W. Latham, II  
Affiliate Professor of Electrical and Computer Engineering



---

Peter B. Runciman  
Chief Technical Officer, L-3 Communications Klein Associates, Inc.



---

Dr. Barbara J. Kraft  
Affiliate Professor of Electrical and Computer Engineering

MAY 7, 2010  
Date

## DEDICATION

*I dedicate the body of this work to my Mother, my Father, George, Joan, my Grandparents, my second family: Denis and Billie, and my life-long friends: Landon, Sarah, and Fred.*

## ACKNOWLEDGMENTS

Every Master's candidate succeeds only with the advice, assistance, guidance, and counsel of an array of committed colleagues and associates who invest time and effort in keeping the candidate on track. I am particularly fortunate to have had a superbly talented and helpful thesis committee comprised of Christian de Moustier, Mike Carter, Paul Latham, Peter Runciman, Barbara Kraft, and, unofficially, the estimable Lloyd Huff. I hereby gratefully acknowledge their collective and individual contributions to this project. Additionally, I recognize and welcome the aid provided by Richard Wanat and Marc Parent of L-3 Klein Associates, Inc.; the technical advice freely given by Stewart Kenly and Andras Ferkete; and the valuable mechanical assistance provided by Paul Lavoie, as well as that of Tom Weber of CCOM/JHC. Further, I thank the National Marine Mammal Laboratory at the Alaska Fisheries Science Center for Grant #NFFS7300-5-00091 and Ward Testa for helping to fund this project, and the UNH / NOAA Joint Hydrographic Center for Grant #NA05NOS400115. I also acknowledge the travel funding provided by CCOM/JHC at UNH that enabled me to participate in the 2010 AGU Ocean Sciences Meeting in Portland, Oregon. Lastly, I would be remiss if I did not acknowledge the constant encouragement and unstinting patience given me by my entire family and close friends. Their support has been instrumental in helping me reach this point in my journey.

## TABLE OF CONTENTS

DEDICATION.....	iv
ACKNOWLEDGMENTS .....	v
LIST OF TABLES.....	ix
LIST OF FIGURES .....	x
ACRONYMS.....	xiii
SYMBOLS.....	xvii
ABSTRACT.....	xix
CHAPTER	PAGE
I. INTRODUCTION.....	1
1.1 Problem Statement .....	1
1.2 The Mixed Signal Approach .....	4
1.3 Summary of the Design.....	6
II. DESIGN AND CONSTRAINT ANALYSIS .....	9
2.1 Utility of the Transponder .....	9
2.2 Design Constraints and the Performance Matrix.....	11
2.3 Initial Analysis .....	14
2.3.1 Operating Frequency, Bandwidth, and Position Precision.....	14
2.3.2 Interrogation Rate and Range Resolution .....	15
2.3.3 Acoustic Range and Power Budget.....	16
III. ANALOG DESIGN – FRONT-END ELECTRONICS .....	18
3.1 Overview of the Analog Design.....	18
3.2 The Transducer.....	19
3.2.1 Overview of the Assembly.....	19



3.2.2	Admittance / Impedance Characteristics.....	21
3.2.3	Electro-Acoustic Response .....	26
3.2.4	Directivity .....	29
3.3	The Microcontroller .....	31
3.4	Switching between RX and TX Modes and the Function of the Grounding FET.....	32
3.5	The Receiver.....	33
3.5.1	Isolation of the Receiver’s Power Supply .....	34
3.5.2	The Low-Noise Amplifier / Bandpass Filter.....	37
3.5.3	Interfacing the Receiver with the ADC Input of the Microcontroller.....	43
3.6	The Transmitter .....	44
3.7	The Battery Supply.....	50
3.8	The Printed Circuit Board .....	53
IV.	DIGITAL DESIGN – EMBEDDED FIRMWARE.....	54
4.1	Overview of the Digital Design and Signal Processing Methodology .....	54
4.2	Receiver Digital Design .....	59
4.2.1	Using the MSP430 to Generate Precise Timing of Samples .....	59
4.2.2	Bandpass Sub-Sampling Scheme for Frequency Translation .....	62
4.2.3	Real-Time Demodulation and Detection of Sampled Signals .....	73
4.3	Transmitter Digital Design .....	80
4.4	Turnaround Time Latency and Uncertainty .....	84
V.	INITIAL RESULTS AND FUTURE DIRECTIONS.....	87
5.1	Proof of Concept .....	87
5.2	Performance Specifications of the Prototype Micro-Transponder .....	91
5.3	Future Directions.....	92
5.4	Final Conclusions .....	93
	LIST OF REFERENCES.....	94

APPENDICES .....	96
A. THE PROTOTYPE MICRO-TRANSPONDER .....	97
A.1 Potted Transducer Interfaced with the PCB Design .....	97
A.2 The Pressure Housing for Prototype Development .....	99
B. THE TRANSDUCER ASSEMBLY .....	100
B.1 Piezoelectric Ceramic .....	100
B.2 Construction of the Assembly .....	100
B.3 Potting .....	104
C. CONFIGURATION OF CALIBRATION EXPERIMENTS .....	106
C.1 TVR / Beam Pattern Measurement Test Setup .....	106
C.2 Data Acquisition Methodology and Self-Reciprocity Test Setup .....	107
D. THE MSP430 MICROCONTROLLER .....	108
E. PRINTED CIRCUIT BOARD LAYOUT .....	109
E.1 Component Placement .....	109
E.2 Four Layer PCB Design .....	111
E.3 Fabricated PCB .....	113

## LIST OF TABLES

Table 3.1: Measured Performance Summary of the LNA / BPF Analog Receiver .....	37
Table 4.1: Current Consumption of the MCU at Applicable Clock Frequencies .....	55
Table 5.1: Power-Demand of the Transponder's Sub-Systems for TX and RX Modes .....	91

## LIST OF FIGURES

Figure 1.1: System Level Block Diagram of the Micro-Transponder .....	5
Figure 1.2: Overview of the Prototype Micro-Transponder .....	7
Figure 2.1: Canonical Flow Chart of the Mixed-Signal Transponder .....	10
Figure 2.2: Illustration of the Performance Matrix .....	13
Figure 2.3: System Requirements of Source Level vs. Slant Range .....	17
Figure 3.1: Overview of the Transducer Assembly .....	20
Figure 3.2: Vector Admittance Measurements of the Transducer .....	22
Figure 3.3: Equivalent Circuit Model of the Transducer .....	25
Figure 3.4: Transmit and Receive Responses of the Transducer .....	27
Figure 3.5: Measured Beam Pattern of the Potted Transducer, $F_0 = 160$ kHz .....	30
Figure 3.6: Grounding FET Topology Implemented in the Design .....	33
Figure 3.7: Circuit Topology of the Receiver's Isolated Power Supply .....	35
Figure 3.8: Transient Operation of the LDO $V_{REF}$ .....	36
Figure 3.9: Overview of the Analog Receiver Design .....	38
Figure 3.10: Measured Frequency Response of the Receiver's Cascaded Sections .....	39
Figure 3.11: Transient Response of the Final Analog LNA / BPF Section .....	42
Figure 3.12: Observed Effects of the SAR ADC Sampling the Received Waveform .....	44
Figure 3.13: Circuit Topology of the Transmit Amplifier .....	45
Figure 3.14: Operation of the Boost Converter when Transmitting a Coded Signal .....	48
Figure 3.15: Operation of the Full-Bridge Driver when Transmitting a Coded Signal .....	49
Figure 3.16: Power Supply Topology .....	51
Figure 3.17: Power Supply Transient Response on Startup .....	52
Figure 4.1: Flow Chart of the Micro-Transponder's Digital (Embedded) Design .....	58

Figure 4.2: Configuration of Timer A to Trigger the Sampling of the SAR ADC .....	60
Figure 4.3: Sample Timing including Conversion and Latency Constraints .....	61
Figure 4.4: Received Signal Collected within the Test Tank, Sampled at 413.8 kHz .....	64
Figure 4.5: Frequency Response of Received Signal(s), Sampled at $F_S = 413.8$ kHz .....	67
Figure 4.6: Received Signal Collected within the Test Tank, Sampled at 49.08 kHz .....	70
Figure 4.7: Frequency Response of Received Signal(s), Sampled at $F_{SS} = 49.08$ kHz .....	72
Figure 4.8: Block Diagram of the Quadrature Digital Demodulator .....	74
Figure 4.9: Timing Constraints when Processing Samples in Real-Time .....	78
Figure 4.10: Flow Chart of a Coded-Signal Transmission .....	81
Figure 4.11: Producing a 50% Duty Cycle 160 kHz Signal with Timer A .....	82
Figure 5.1: Data Acquisition Methodology for Testing the Functionality of the Transponder .....	88
Figure 5.2: Query Waveform used to Interrogate the Micro-Transponder .....	89
Figure 5.3: The Acoustic Conversation as Observed by the TC4034 Hydrophone .....	90
FIGURES IN APPENDICES	
Figure A.1: Prototype Transponder (PCB Top Shown) .....	97
Figure A.2: Prototype Transponder (PCB Bottom Shown) .....	98
Figure A.3: Pressure Housing (Side View) .....	99
Figure A.4: Assembled Pressure Housing .....	99
Figure B.1: Piezoelectric Ceramic with Soldered Electrode .....	100
Figure B.2: Machined Brass Mount used to House the Transducer Assembly .....	100
Figure B.3: Punch Used to Cut 1/16" Corprene Sheet for the Transducer Assembly .....	101
Figure B.4: The Brass Mount and The Corprene Sections Surrounding the Ceramic .....	102
Figure B.5: Assembling the Transducer .....	102
Figure B.6: Assembled Transducer (Front View) .....	103
Figure B.7: Assembled Transducer (Back View) .....	103
Figure B.8: Transducer Assembly Mounted to Pressure-Housing Lid (Pre-Potting) .....	104

Figure B.9: Potted Transducer Assembly within Pressure-Housing Lid .....	105
Figure B.10: Side View of Pressure-Housing Lid .....	105
Figure C.1: Overhead View of the Calibration Setup at the Klein Test Tank .....	106
Figure C.2: Side View of Tank Test Setup used to collect Sampled Waveforms.....	107
Figure D.1: Circuit Topology of the Microcontroller .....	108
Figure E.1: Reference Designation of Discretes Placed on the Top of the PCB .....	109
Figure E.2: Reference Designation of Discretes Placed on the Bottom of the PCB.....	110
Figure E.3: Top Two Layers of the PCB Design.....	111
Figure E.4: Bottom Two Layers of the PCB Design .....	112
Figure E.5: Top of the Fabricated PCB, Screw holding the Transducer Assembly.....	113
Figure E.6: Bottom of the Fabricated PCB with Mounted Transducer Assembly.....	114

## ACRONYMS

ADC(12)	-----	Analog to Digital Converter (12-bit)
AGC	-----	Automatic-Gain Control
AGU	-----	American Geophysical Union
ALU	-----	Arithmetic Logic Unit
AM	-----	Active Mode
APS	-----	Acoustic Positioning System
AWG	-----	American Wire Gauge
BAT	-----	Battery
BJT	-----	Bipolar Junction Transistor
BL	-----	Burst Length
BPF	-----	Bandpass Filter
BW	-----	Bandwidth
CAD	-----	Computer Aided Design
CC/CE	-----	Common-Collector / Common-Emitter
CCIFG	-----	Capture/Compare IFG (for Timer A)
CPU	-----	Central Processing Unit
CW	-----	Continuous Wave
DAQ	-----	Data Acquisition
DC	-----	Direct Current
DCO	-----	Digitally Controlled Oscillator
DFT	-----	Discrete Fourier Transform
DMA	-----	Direct Memory Access (Controller)
DRVR	-----	Driver
DSP	-----	Digital Signal Processing
DST	-----	Data Storage Tag
DUT	-----	Device under Test
EN	-----	Enable
EQ	-----	Equivalent
ESR	-----	Equivalent Series Resistance
FET	-----	Field-Effect Transistor
FIR	-----	Finite Impulse Response (Filter)

FS----- Full-Scale  
 GBW ----- Gain-Bandwidth (Product)  
 GND----- Ground  
 HPF----- Highpass Filter  
 I/O ----- Input/Output  
 I/Q ----- In-phase and Quadrature (Samples)  
 IC ----- Integrated Circuit  
 IDE ----- Integrated Development Environment  
 IFG ----- Interrupt Flag  
 IN ----- Input  
 ISR----- Interrupt Service Routine  
 JTAG----- Joint Test Action Group (IEEE 1149.1)  
 LC ----- (Parallel or Series) Inductor and Capacitor  
 LDO ----- Low Drop Out (Voltage Regulator)  
 LIM----- Limiter  
 LNA ----- Low-Noise Amplifier  
 LOS----- Line-of-Sight  
 LPF ----- Lowpass Filter  
 LPMx----- MSP430 Low-Power Mode ( $x = 0 \rightarrow 4$ )  
 LRC ----- (Parallel or Series) Inductor, Resistor, and Capacitor  
 LSB----- Least Significant Bit  
 LSW ----- Least-Significant Word  
 LT----- Linear Technology  
 MCLK----- Master Clock  
 MCU ----- Microcontroller  
 MEM ----- Memory  
 MRA ----- Maximum Response Axis  
 MSB ----- Most-Significant Bit  
 MSP430----- TI Mixed-Signal Processor (MCU)  
 MSW ----- Most-Significant Word  
 MUX ----- Multiplexer  
 NB ----- Number of Bursts  
 NC ----- Non-Connect  
 N-MOSFET ----- N-Channel Metal Oxide Semiconductor FET



NOAA----- National Oceanic and Atmospheric Administration  
 NPN ----- Semiconductor Doping Scheme of BJT  
 NSF ----- National Science Foundation  
 OCVR----- Open-Circuit Voltage Response  
 OSC -----Oscillator  
 OUT ----- Output  
 PC-----Program Counter  
 PCB----- Printed Circuit Board  
 PNP----- Semiconductor Doping Scheme of BJT  
 PPS ----- Pings-Per-Second  
 PSD----- Power Spectral Density  
 PWM -----Pulse Width Modulation  
 PZT ----- Lead-Zirconate-Titanate  
 RAM -----Random-Access Memory  
 RC -----(Parallel or Series) Resistor and Capacitor  
 REF----- Reference  
 RMS ----- Root Mean Squared  
 RX ----- Receiver (or Receive Mode Operation)  
 S/H-----Sample and Hold (Operation)  
 SAR ----- Successive Approximation Register  
 SHI ----- S/H Input (to ADC12)  
 SL----- Source Level  
 SMCLK ----- Sub-Main Clock  
 SONAR -----Sound Navigation and Ranging  
 SPL ----- Sound Pressure Level  
 SR----- Status Register  
 SS -----Sub-Sampling (Frequency)  
 SYNC -----Synchronizing  
 T/R----- Transmit or Receive  
 TA ----- Turnaround (Time)  
 TA0/TA1 -----Timer A Output Channel 0/1  
 TACCR ----- Timer A Capture/Compare Register  
 TAIFG -----Timer A IFG  
 TAR ----- Timer A Register

TI ----- Texas Instruments  
TT----- Travel Time  
TVR ----- Transmit Voltage Response  
TX ----- Transmitter (or Transmit Mode Operation)  
USB ----- Universal Serial Bus  
USBL----- Ultra-Short Baseline  
XDCR----- Transducer  
XTAL ----- Crystal

## SYMBOLS

$A_v$	-----	Voltage Gain [V/V]
$b$	-----	(Number of) Bits
$B$	-----	Susceptance [S]
$BW$	-----	Bandwidth [Hz]
$C$	-----	Capacitance [F]
$c$	-----	Sound-Speed [m/s]
$D1 \rightarrow D5$	-----	Reference Designation of a Specific Diode
$dc$	-----	Duty Cycle [%]
$E$	-----	(Electrical) Energy [Wh]
$f$	-----	Frequency [Hz]
$F$	-----	Frequency of Specific Merit [Hz]
$G$	-----	Conductance [S]
$g_m$	-----	Transconductance [A/V]
$H$	-----	Transfer Function
$I$ (Figure 4.1 and Section 4.2.3)	-----	In-Phase Sample(s)
$I$	-----	(Electrical) Current of Specific Merit [A]
$i$	-----	Instantaneous (Electrical) Current [A]
$IR$	-----	Interrogation Rate [pps]
$k$ (Figure 4.8)	-----	Discrete Filter Tap Coefficient
$k$	-----	Discrete Frequency Indexing Variable
$L$	-----	Inductance [H]
$m$	-----	Discrete Time Indexing Variable
$n$	-----	Sample Number / Discrete Time Indexing Variable
$N$	-----	Integer Number
$N_0$	-----	(Acoustic) Noise Spectral Density [dB re $1 \mu\text{Pa}^2 / \text{Hz}$ ]
$NL$	-----	(Acoustic) Noise Level [dB re $1 \mu\text{Pa}$ ]
$OCVR$	-----	Open-Circuit Voltage Response [dB re $V_{RMS} / 1 \mu\text{Pa}$ ]
$P$	-----	(Electrical) Power of Specific Merit [W]
$P_{XX}$	-----	PSD via Periodogram [dB re $V_{RMS}^2 / \text{Hz}$ ]
$Q$ (in Figure 4.1 and Section 4.2.3)	-----	Quadrature Sample(s)

Q	-----	Quality Factor [Hz/Hz]
Q1 → Q7	-----	Reference Designation of a Specific Transistor
R	-----	Resistance [ $\Omega$ ]
r	-----	Slant Range [m]
R5/R12 (Chapter IV)	-----	MSP430 CPU Register 5/12
re	-----	Referenced to
SL	-----	Source Level [dB re 1 $\mu$ Pa at 1 m]
SNR	-----	Signal to Noise Ratio [dB]
SPL	-----	Sound Pressure Level [dB re 1 $\mu$ Pa]
t	-----	Instantaneous Time [s]
T	-----	Period of Time [s]
TL	-----	Transmission Loss [dB re 1m]
TVR	---	Transmit Voltage Response [dB re 1 $\mu$ Pa / $V_{RMS}$ at 1 m]
U1 → U4	-----	Reference Designation of a Specific IC
v	-----	Instantaneous Voltage [V]
V	-----	Voltage of Specific Merit [V]
$V_{CC}$	-----	Positive Supply Voltage [V]
X	-----	Reactance [ $\Omega$ ]
x	-----	Time Sampled Voltage Value
Y	-----	Admittance [S]
z	-----	Discrete Time-Delay
Z	-----	Impedance [ $\Omega$ ]
$\tau$	-----	Time Constant [s]
$\omega$	-----	Angular Frequency [rad/s]

## ABSTRACT

### A MICRO-TRANSPONDER FOR PRECISION TRACKING OF UNDERWATER TARGETS

By

Albert Whitaker Franzheim, III  
University of New Hampshire, May, 2010

A prototype micro-transponder has been designed and built to track, in real-time, the positions of objects or animals within the water column. Commercially available data storage tags, which help monitor the behavior of underwater animals, do not provide real-time interrogation and data dissemination capabilities in a form factor and acoustic frequency band acceptable for active tracking applications.

This prototype is 18.5 cm<sup>3</sup> and weighs 43.7 g in air. It operates at an acoustic frequency of 160 kHz and uses a mixed-signal topology with low-power components and a microcontroller, which allows for firmware updates and addition of external sensors. It is powered by a lithium battery that provides enough energy for an 8-day deployment at a 1-second interrogation interval. Tests carried out in a tank confirmed the functionality of the design with coded replies being transmitted at source levels of 167 dB re 1  $\mu$ Pa at 1 m.

# CHAPTER I

## INTRODUCTION

### **1.1 Problem Statement**

The motivation for this project began through a National Science Foundation (NSF) research proposal to study Weddell seals foraging in the Antarctic. Typically, research scientists use Data Storage Tags (DSTs) to collect positioning information of seals while they search for their prey. The DSTs are attached to the epidermis of a seal and logs their activity while underwater. Once the seal is re-captured, the DSTs are removed and their data are downloaded and post-processed. These data are then used to interpolate the track of the seal's dive (Davis et al., 2004). Since DST technology has been a tried and tested methodology for tracking this well-behaved species in a semi-controlled environment, part of the goal behind this NSF proposal was to develop and test new technology capable of (1) tracking seals in real-time and (2) recovering the data without physically retrieving the tag.

The DST methodology is preferred to that of traditional SONAR echolocation techniques because foraging seals often dive into large schools of fish hindering the measurement. Transmitting acoustic tags could potentially be used to ensonify the location of the foraging seals even in severe multi-path environments, thus allowing such measurements to be made (Davis, et al., 2003). Pingers are one type of acoustically transmitting tag and are widely used in fisheries research to track the location of (even small) fish. They are 16-100 mm in their longest dimension, robust, able to produce relatively high acoustic levels (136-160 dB re 1  $\mu$ Pa at 1 m), and are encoded with a device specific signature. Some pingers produce up to 25 pings-per-second for high-resolution tracking.

Acoustic signals propagate over long distances underwater ( $\gg 10$  m). They are

singularly used for underwater communication of mammals and SONAR systems. Because attenuation due to absorption is proportional to frequency squared and because the ambient noise level spectrum is lowest between 10-60 kHz, many SONAR systems are designed to operate within this band. If a transmitting tag were affixed to the body of a seal, its operation must be non-invasive to the natural activities of that animal. However, most transmitting tags operate in the auditory band of many Pinniped species (up to 65 kHz; Schusterman, 1981). Commercially available transponders have been designed for relocation and reconnaissance of expensive equipment in deep-water applications. Commercially available pingers, on the other hand, are widely used in fisheries research. They have also been designed for tracking certain species of fish. The inner ears of most fish do not enable them to hear above 1 kHz although some species of Clupeids “can detect ultrasonic frequencies up to 180 kHz” (University of Rhode Island, 2009). A few pingers have been built to operate at higher frequencies (e.g. 307 kHz for the Model 795 Acoustic Tags from HTI).

It is important to distinguish between the two types of acoustically transmitting tags: pingers and transponders. Pingers are the simplest form of transmitting tag. Their function is limited to transmitting an encoded message at a fixed rate for the duration of their battery life. Their performance is either optimized for extended life transmission or range-resolution transmission. Transponders only respond when an inquiring source requests a transmission. Transponders can therefore utilize their limited energy supply for power intensive acoustic transmissions only when a destination is assured of receiving their transmitted message. Conversely, a pinger’s battery power would be wasted if no one were receiving its transmitted message. Because the transponder is interrogated by an external source before it responds with encoded data, it can achieve both: good range-tracking (from being interrogated frequently) and extended life transmissions (provided that it is not continuously queried). Some transponder designs enable users to deploy a tag and collect its transmitted data at periodic intervals that are convenient for data logging.

Since a transponding tag is interrogated by another source, its design is inherently more (functionally) flexible. A transponding tag might be interrogated once a second for tracking a particular type of target. This same transponder might also be used to track a faster moving target with an interrogation rate of 25 times a second. The inquiring source, in this case, controls the data rate, as opposed to the fixed rate of a pinging tag. The transponder is a bi-directional communication device. This functionality adds complexity to both hardware and software designs. If used for target tracking, the transponding tag actually reduces the complexity of the Acoustic Positioning System (APS) used to measure its position.

APSs are used to identify the location of targets underwater. Targets may be stationary or moving within the volumetric space. APSs collect data from a target to determine its location. Depending upon the system, they do so either by triangulating the time-of-arrivals, actively beam-steering, or differentially measuring the phase on two or more receive transducers. A network of receive elements is used, in all cases, to determine the location of the underwater target.

Range measurements can be estimated via time differentials, therefore, the transponder's function lends itself to tracking a target's position from a single transceiving source. By contrast, an APS must use multiple receivers spaced appreciably apart and synchronized to a master clock to triangulate the position of a pinger. Such a system is harder to deploy, potentially more costly, susceptible to human error, and often not used in real-time compared with, for example, a single Ultra-Short Baseline (USBL) APS that can resolve a transponding target's position. Unfortunately, most commercially available transponders are not designed for tracking moving, small, and/or organic targets. Existing underwater acoustic transponders are too bulky and heavy for this application, and they operate at acoustic frequencies in the auditory band of seals. Furthermore, standard echo-sounding methods cannot distinguish a seal in the midst of a fish school or one located near the sea floor. Thus, DSTs continue to be used for observing the movements of seals.



Because current methods for uniquely identifying underwater targets did not provide interrogation and data dissemination capabilities in a form factor and frequency band acceptable for tracking seals, the goal of this thesis project was to design and build a transponding tag that would eventually enable research scientists to track Weddell seals (and other species) without the aid of a DST. The specifications for the design were established and listed as the following:

- The transponder shall operate within the 100-200 kHz frequency band.
- The transponder's acoustic level and efficiency shall be scaled to ensure communication with a SONAR system at a maximum range of 500 m.
- The transponder shall provide data transmission rates in excess of 1 ping per second (pps) to enable a range resolution no less than 4 m when tracking a seal moving at 4 m/s.
- The operation of the individual transponders shall be autonomous and, therefore, run off an internal battery which provides enough energy for their entire deployment duration (a minimum of 24-48 hours of continuous interrogations).
- The transponder's physical size and weight shall not exceed 500 cm<sup>3</sup> and 300 g in air.

Although the NSF proposal was not funded, a small grant from the NOAA's Alaska Fisheries Science Center – National Marine Mammal Laboratory made it possible to develop a prototype micro-transponder.

## **1.2 The Mixed Signal Approach**

A microcontroller-based implementation of an underwater transponder was chosen because it allows firmware to be updated. As better signal processing algorithms are developed and external sensors added to the design, the transponder can be re-programmed accordingly. To minimize the overall size of the device without constraining its functionality, the analog design was intentionally kept simple yet controllable by the microcontroller itself. Future improvements of the digital design could potentially allow telemetry data to be encoded in a reply without a

physical re-design of the analog hardware. Figure 1.1 shows the block diagram of the sub-systems that make up the micro-transponder and illustrates its mixed signal design.

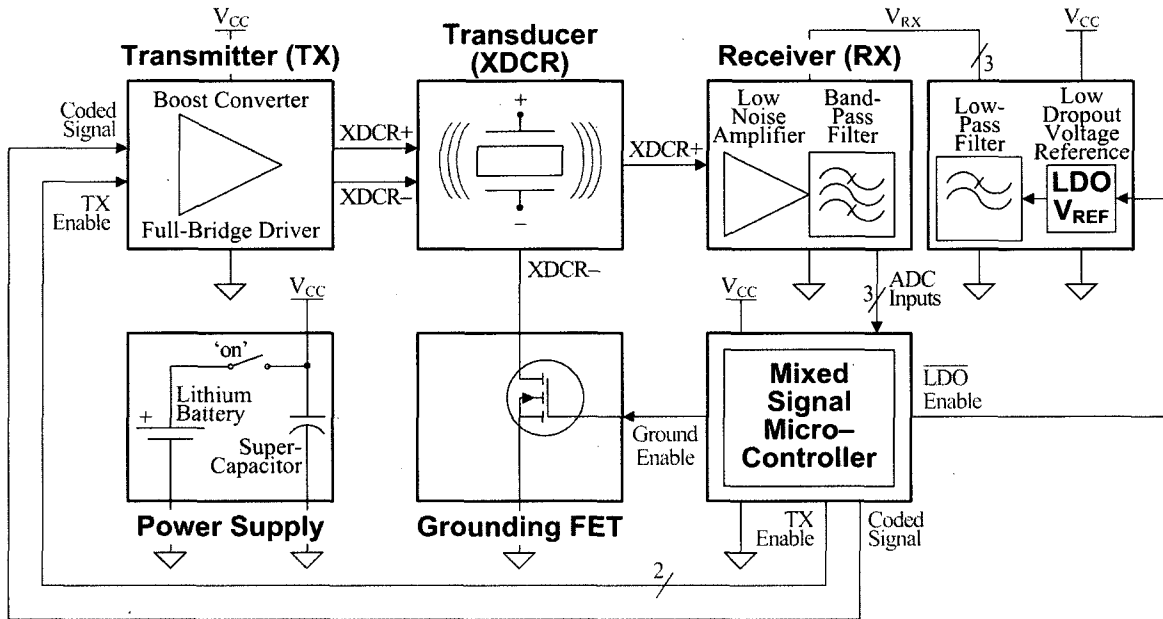


**Figure 1.1: System Level Block Diagram of the Micro-Transponder**

The sub-systems of the design are annotated in yellow and their interconnections displayed in red, black, green, and blue representing power, ground, digital (switching) signals, and analog signals; respectively.

The microcontroller (MCU) directs the functions of the analog sub-systems within this design<sup>1</sup>. When receiving, it grounds the negative terminal of the transducer and enables power to the single-ended analog receiver (RX). As acoustic waves interact with the micro-transponder, potential is generated across the leads of the transducer (XDCR). This, now, electrical signal is then amplified and filtered by the analog receiver whose output is fed into the Analog to Digital Converter (ADC) of the microcontroller. The MCU interprets the digital samples it collects and processes them in real-time. It does so through a process called quadrature down conversion. The MCU detects interrogation signals digitally by computing their complex magnitude and comparing it with a threshold value stored in memory. When the MCU determines that these detections correlate with an inquiry from an APS (or other source), it powers down the receive

<sup>1</sup> Except for the mechanical 'on' switch that controls the operation of the power supply.

circuitry, ‘cuts-off’ the channel of the Grounding FET, activates the boost converter and full-bridge driver, and generates a coded signal. This coded signal is amplified and differentially driven by the transmitter (TX) onto the two leads of the transducer. After the coded signal is transmitted, the MCU shuts down the transmitter, grounds the negative lead of the transducer, and enables power to the receiver. The process, repeats, until the internal battery is depleted and can no longer provide current to these sub-systems.

This document describes the details of this design, explains how it was implemented, examines the performance of the assembled prototype, and documents the results of initial tank tests. Because requirements were explicitly made with regard to the performance of the transponder, a careful analysis of the design and its constraints are examined within Chapter II. Specific details of the mixed signal design are examined within Chapters III and IV as related to the reception and transmission of signals in the water column. Chapter III describes the analog components of the design, including an analysis of the performance of the electronic circuitry. Chapter IV describes the digital design that was downloaded to the microcontroller and the signal processing methodology that was used to demodulate and detect received signals. Finally, the initial tank test results, which validate the functionality of the prototype, are shown in Chapter V. Additional suggestions on the future development of this technology and concluding remarks are made within the final chapter.

### **1.3 Summary of the Design**

The micro-transponder, designed and built for this project, is approximately the size of a matchbook (L: 50 mm × W: 37mm × H: 10mm) and weighs 43.7 g in air. It operates in the acoustic frequency band of 155-165 kHz, which is above the known hearing band of Weddell seals. A Printed Circuit Board (PCB) has been assembled with all of the circuitry for transponding. It includes a lithium battery that provides enough energy for a deployment duration of ~8.7 days, if continually interrogated once a second. The microcontroller

demodulates and detects received signals in real-time. It replies within 2.46 ms ( $\pm 0.04$  ms) upon receiving a 500  $\mu$ s, 160 kHz Continuous Wave (CW) interrogation burst. Its reply is encoded and transmitted into the water at a source level of 167 dB re 1  $\mu$ Pa at 1m.

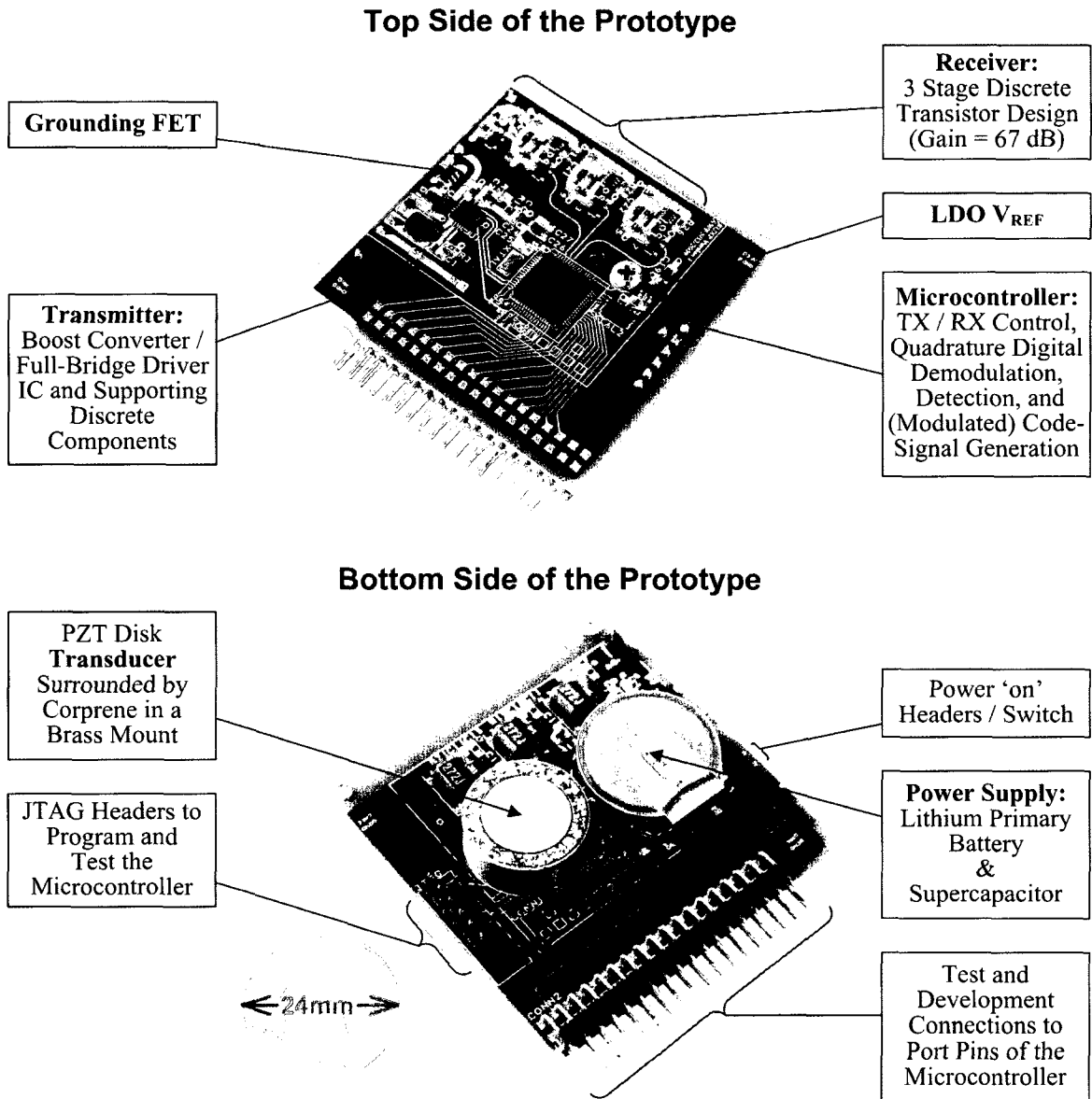


**Figure 1.2: Overview of the Prototype Micro-Transponder**

A photograph of the unpotted prototype shows the top and bottom of the PCB design and annotates relevant features of its design. A US Quarter is included for scale reference.

Figure 1.2 highlights the features of the current manifestation of the micro-transponder.

Its discrete parts were populated onto a four-layer PCB that was specifically designed and built

for this project. For prototype development and the testing, the transducer itself was potted in urethane and integrated into the lid of a pressure-housing. The prototype PCB was mounted to the inside of the same lid and when closed sat watertight inside the enclosure. Photographs of the prototype form of the micro-transponder, as tested within the tank, are shown in Appendix A. Throughout the body of this text it can be assumed that the micro-transponder in this physical form was used to collect the data that are displayed and discussed.

## CHAPTER II

### DESIGN AND CONSTRAINT ANALYSIS

#### **2.1 Utility of the Transponder**

A transponder is a communication device that automatically transmits an encoded message upon reception of a recognized interrogation signal. The most basic transponder will respond with a signal that is a simple permutation of the signal that was used to interrogate it. Such a device is often called a responder because it simply re-broadcasts signals at a predefined power level. Re-broadcasts are delayed by a known period of time because of latency with internal circuitry. When a common interrogation is used in a field of multiple transponders, the re-broadcast signal might be altered in frequency or encoded differently to tell an APS which device has replied. A “telemetry” transponder is interrogated in the same fashion as the responder, but it replies with a more sophisticated message that contains data gathered *in-situ*.

Transponders are used whenever querying devices want information to be broadcast into the communication channel. As illustrated by the canonical flow chart (Figure 2.1), a transponder is a device that “listens” or “waits” for signals of a predetermined signature before it replies. The micro-transponder prototype designed and built for this project is an update of the “Transponding Acoustic Fish Tag” described by Mitson (1971). The current design uses a microcontroller and modern low-power components to maximize utility. Detection of an interrogation signal is accomplished, in real-time, by an algorithm that is continuously executed until it determines that a ‘signal’ has been detected. The algorithm is then directed at controlling hardware and generates a coded signal for transmission. Once the reply is sent, the algorithm returns control to the analog receive portion of the hardware and starts “listening” for the next potential query.

When programmed to continuously detect signals in the water column, the micro-

transponder has two primary modes of operation: receive and transmit. Assuming that the transponder operates a vast majority of the time in receive mode, the analog receive circuitry and the digital detection processing should be optimized for power-demand in receive mode. Conversely, when the transducer transmits, output power must be sufficient to be received by an inquiring source over a maximum range. The transponder must switch between receive and transmit modes to minimize power-demand and maximize operating range. The average power-demand of the device will, therefore, be a function of the duty cycle with which the device transmits and receives.

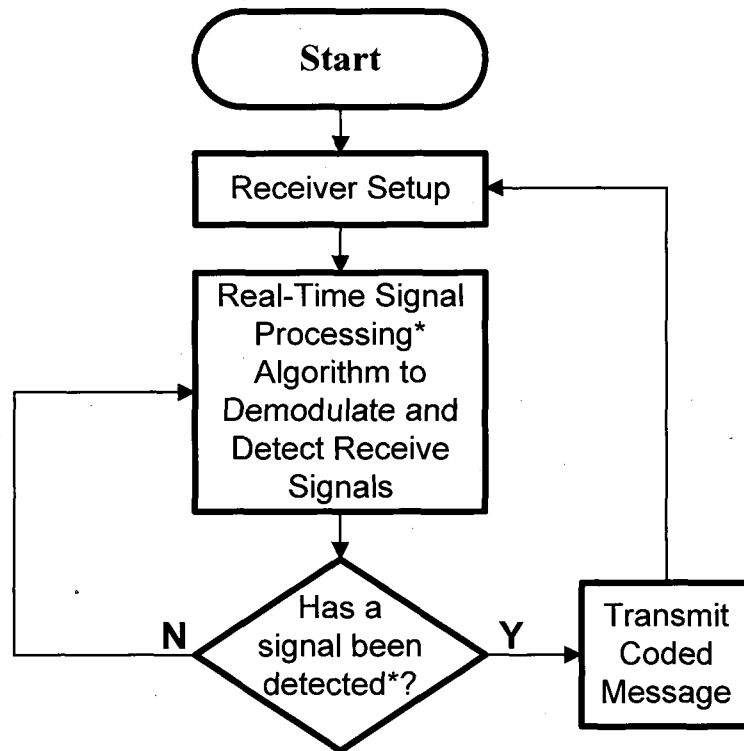


**Figure 2.1: Canonical Flow Chart of the Mixed-Signal Transponder**

\* denotes parts of this design that are implemented with real-time signal processing.

## **2.2 Design Constraints and the Performance Matrix**

The design of the micro-transponder is constrained by fundamental properties of sound propagation in water and the limitations of electro-acoustic technologies. For radiation of sound underwater, a transducer is typically operated about its mechanical resonance. The acoustic wavelength ( $\lambda$ ) produced by the transducer in water is equal to the ratio of Sound-Speed ( $c$ ) and the Frequency ( $F_0$ ) at which the transducer drives the medium. In general, the physical size of the transducer is proportional to the lengths of the acoustic waves with which it converts energy efficiently. The transducer's resonance frequency, bandwidth (BW), and power efficiency are all governed by the properties of the materials used in its construction. In these ways, limitations of transducer technology constrain the design of the micro-transponder.

Physical limitations of sound propagation in water further constrain the design. Geometrical spreading, attenuation, and ambient noise levels in water limit the maximum range of the underwater acoustic communication. In general, the maximum range of a SONAR system is based on (1) its ability to distinguish 'signal' from 'noise' when setting a detection threshold and for a given receiver bandwidth and (2) its source level, operating band, and directivity with respect to sound projection. Transponders automatically reply to an interrogation and do so within a known "turnaround time." Response time uncertainty is unavoidable because (1) these devices are band-limited, (2) the propagation medium fluctuates in time and space, (3) and the transponder's turnaround time is variable.

Deployment duration is a fundamental design constraint and a critical figure of merit for battery-operated devices. Deployment duration is proportional to the internal energy of the battery and inversely proportional to the average power-demand of the device. To maximize its life-span and reduce self-noise, the micro-transponder switches 'off' its transmitter when receiving<sup>2</sup>. If continually being interrogated, the average power-demand ( $P_{AV}$ ) is a function of the

---

<sup>2</sup> This assumes that more power is demanded when transmitting.



transponder's transmit duty cycle ( $dc_{TX}$ ). If  $P_{TX}$  is the power-demand within the period of its transmission ( $T_{TX}$ ) and  $P_{RX}$  is the power-demand within the period of its reception ( $T_{RX}$ ), the following equation can be used to calculate the average power-demand of the transponder:

$$P_{AV} = \left(\frac{T_{TX}}{T_{TX} + T_{RX}}\right)P_{TX} + \left(\frac{T_{RX}}{T_{TX} + T_{RX}}\right)P_{RX} = (dc_{TX})P_{TX} + (1 - dc_{TX})P_{RX}$$

The maximum deployment duration of the transponder is constrained by its power-demand when receiving ( $P_{RX}$ ). When replying to a large number of interrogations, the average power-demand increases and its life-span decreases.

The instantaneous current that a power supply can provide to the remainder of the circuit is also limited. Because batteries are current limited by their internal resistance, a supercapacitor will be used in this design to store energy and make it available to the circuit when transmitting. Once fully charged to the battery's voltage ( $V_{CC} = V_{BAT}$ ), the energy available for acoustic transmission is constrained by the capacitance ( $C$ ) of the supercapacitor and the maximum allowable voltage drop of the transmit circuitry ( $V_{drop}$ ). The maximum transmit time ( $T_{TX}^{max}$ ) is proportional to the energy stored in the capacitor and is inversely proportional to the power-demand of the transmit circuitry ( $P_{TX}$ ). Assuming that the supply voltage is allowed to drop by ~30%, the following equation is used to approximate the maximum transmit time of the micro-transponder:

$$T_{TX}^{max} = \frac{C(V_{drop})^2}{2 P_{TX}} = \frac{C(V_{CC} - V_{CC} / \sqrt{2})^2}{2 P_{TX}} = \frac{C(V_{CC})^2}{4 P_{TX}}$$

Likewise, the energy stored within this capacitor also constrains the maximum interrogation rate of the micro-transponder and is inversely proportional to its average power-demand at this rate. When this happens, the capacitor is unable to re-charge before the micro-transponder is interrogated again. Batteries and capacitors are technologically limited in their energy density and power delivery and thus further constrain the design in size, weight, and cost.

Figure 2.2 describes the interconnectedness of these constraints and illustrates the

quantitative and qualitative performance measures with which it is designed.

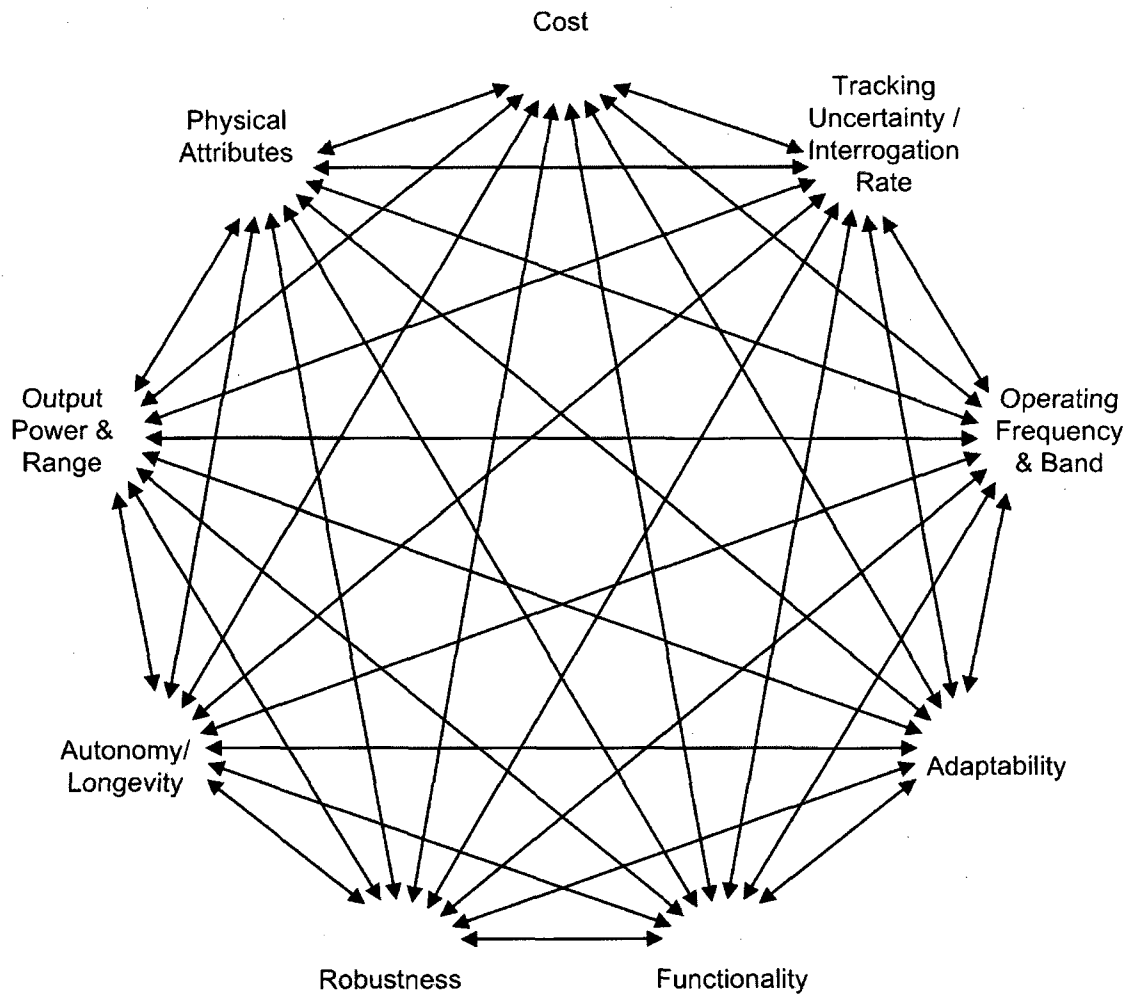


**Figure 2.2: Illustration of the Performance Matrix**

This figure illustrates the complex trade-offs of the design. The quantitative and qualitative performance measures of the design are annotated with blue and orange circles, respectively.

Because the interdependencies of design constraints were complex, the following approach was used in the construction of the micro-transponder to maximize its utility and meet the specifications listed in Section 1.1:

1. Pick a single piezoelectric ceramic based on the operating frequency and band of a commercially available APS with the caveat that is also above the auditory range of

Weddell seals.

2. Construct an acoustic power budget based on the bandwidth and electro-acoustic response of the transducer and determine the power requirements for its operation over a range of 500 m.
3. Design a circuit topology and pick modern and commercially available components (including a MCU) based on size, weight, and power-demand characteristics.
4. Construct an electrical power budget and choose a power-supply architecture based on the results of 2 and 3.
5. Lastly, design a multi-layer PCB. Have it fabricated and populate it with the discrete circuit elements of the design.

## **2.3 Initial Analysis**

### **2.3.1 Operating Frequency, Bandwidth, and Position Precision**

A piezoelectric ceramic transducer with material type and dimension that resonates at 160 kHz is chosen because it is desirable for the micro-transponder to be interrogated by a WASSP multibeam sonar system (<http://www.wassp.com>) and it is also above the underwater audiogram of Pinnipeds (Richardson, 1995). When monitoring the movements of the transponder with an APS, the following equation is used to relate the two-way slant-range uncertainty ( $\Delta r$ ) to the sound-speed ( $c = 1500$  m/s) of water and the turnaround uncertainty of the transponder ( $\Delta T_{TA}$ ):

$$\Delta r = \Delta T_{TA} \frac{c}{2}$$

Assuming it will have a turnaround time uncertainty of 0.2 ms, a transponder can precisely identify its position to within 0.15 m in water. For tracking targets traveling at 4 m/s, let us suppose that the WASSP will serve as an APS with an interrogation rate of 1 ping-per-second (pps) to accurately track this target to within 4 m of slant range. In this case, the jitter of the transponder's reply results in a positioning confidence of ~3.75% for targets moving at this speed.

Because this jitter is largely constrained by the bandwidth of the transponder's receiver, and since bandwidth is inversely proportional to the steady-state response time of the receiver ( $\tau = 1/BW$ ), this system will require at least 5 kHz bandwidth.

### **2.3.2 Interrogation Rate and Range Resolution**

At a maximum slant range ( $r^{\max}$ ) of 500 m, the interactions of an APS and a micro-transponder will have a two-way travel-time difference ( $\Delta T_{TT}$ ) that is a function of the range and the turnaround time of the transponder ( $T_{TA}$ ):

$$\Delta T_{TT} = \frac{2r^{\max}}{c} + T_{TA}$$

The maximum rate with which the APS can interrogate a transponder ( $IR^{\max}$ ) will additionally be limited by the duration of the information sent from ( $T_{\text{interrogation}}$ ) and received by ( $T_{\text{reply}}$ ) the APS:

$$IR^{\max} = \frac{1}{\Delta T + T_{\text{interrogation}} + T_{\text{reply}}}$$

In this way, interrogation rate (pps) is constrained by these quantities. Turnaround time is proportional to the duration of the interrogation and is also constrained by the transponder's receiver bandwidth as well as the circuitry used to detect, wake-up, and generate a reply. If it is assumed that an APS communicates with a transponder and both systems are band-limited to within 5 kHz, and data is encoded in lengths of 10 times their steady-state response time ( $10\tau \sim 2$  ms), and the transponder's turnaround time is 2 times the length of these pulses ( $\sim 4$  ms); the maximum interrogation rate for an APS communicating with a target at 500 m is calculated to be  $\sim 1.5$  pps. In order to track moving targets within the water column, the interrogation rate introduces uncertainty in the slant range precision of an APS. That is, when moving targets are moving at 4 m/s directly toward or away from the APS, the system will not be able to identify its

slant range to better than 4 m, if the interrogation rate is 1 pps.

Slant-range resolution is constrained by the bandwidth of the APS's receiver ( $\Delta r = c / (2 BW_{APS})$ ) and the uncertainty with which the transponder can identify the movements of objects or animals in the water. This uncertainty is calculated as the product of the target's speed and the jitter of the transponder's reply ( $\Delta T_{TA}$ ). Using the same assumptions previously made, this product is calculated as 0.8 mm, which is a fraction (0.02%) of the slant-range resolution of the APS. Therefore, the 'assumed' function of the transponder is acceptable for tracking targets moving at 4 m/s.

### **2.3.3 Acoustic Range and Power Budget**

Because a transponder communicates directly with an APS, the acoustic power budget must account for only one-way travel losses in the water column. A first-order analysis of the SONAR budget illustrates the range and power constraints of sound propagation in water. The following assumptions are made with regard to the analysis of the SONAR budget:

1. APS / Transponder acoustically communicate within the band of 155 – 165 kHz.
2. A worst case transmission loss of sound absorption ( $TL_A$ ) in seawater at 165 kHz is approximated by an attenuation coefficient  $\alpha = 60$  dB / km (Francois & Garrison, 1982).
3. The noise spectral density above 50 kHz increases by ~6 dB per octave and is approximated using the following equation:  $N_0 = -15 + 20 \log_{10}(F_0(kHz)) \approx 30$  dB.

Assuming white noise is within the receive band, noise level is approximated by:

$$NL = N_0 + 10 \log_{10}(BW(Hz)) \approx 70 \text{ dB for a 10 kHz bandwidth (Urlick, 1983).}$$

4. A Signal to Noise Ratio (SNR) of 13 dB is assumed to be required for signal detection by their receivers.
5. The geometric spherical spreading losses are range dependent and calculated as:

$$TL_S = 20 \log_{10}(r(m)).$$

6. A direct Line-of-Sight (LOS) Source Level (SL) acoustic budget is calculated by the following equation:  $SL = TL_A + TL_S + NL + SNR$ .

Figure 2.3 displays the acoustic power requirements of the system. This acoustic power budget shows that a source level of at least 167 dB re 1  $\mu$ Pa at 1 m is required to achieve reliable (+13 dB of SNR) communication at a range of 500 m.

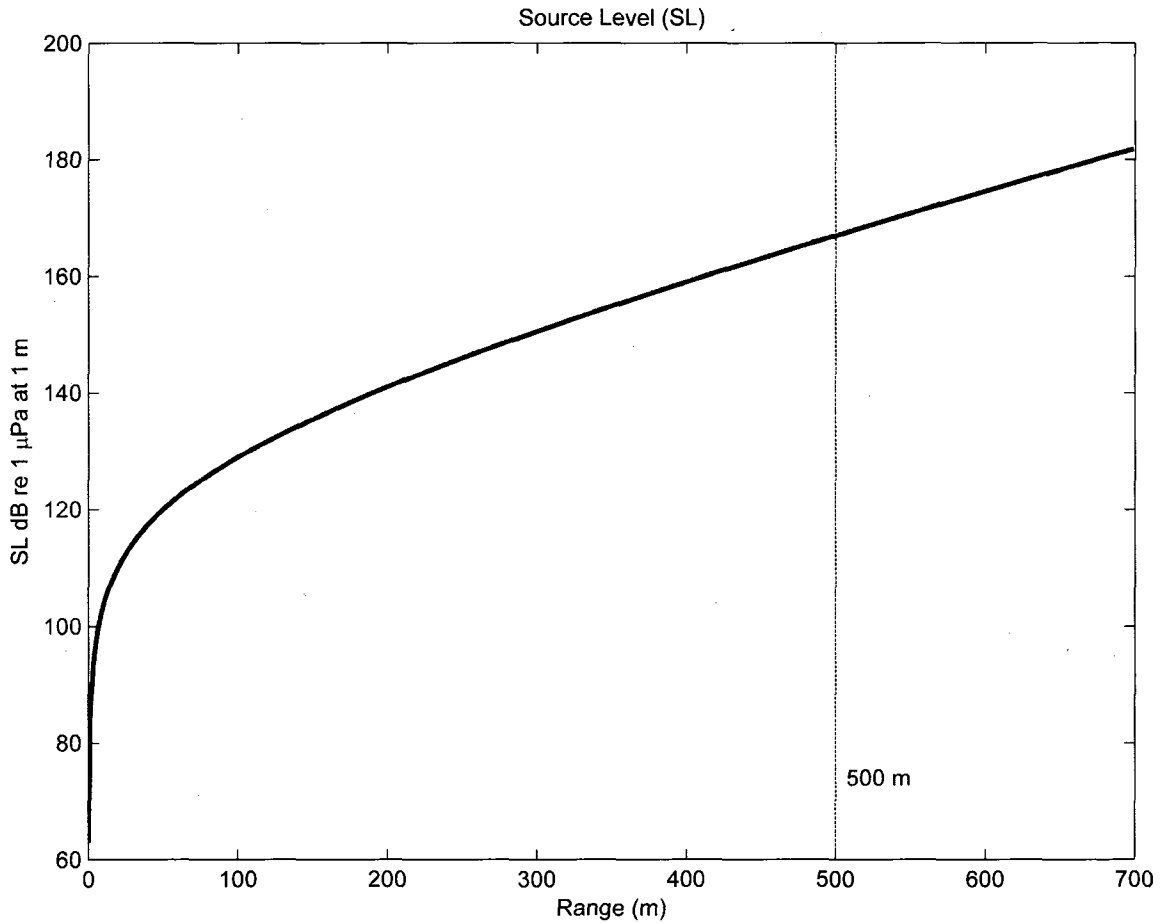


**Figure 2.3: System Requirements of Source Level vs. Slant Range**

The Source Level required to produce a SPL that is 13 dB above the ambient noise in water is shown.

## CHAPTER III

### ANALOG DESIGN – FRONT-END ELECTRONICS

#### **3.1 Overview of the Analog Design**

The ‘analog’ component of the micro-transponder can be characterized as the portion of the design that interacts with the physical environment and pertains to continuous-time varying signals such as pressure, electric current, and voltage. The analog front-end of the micro-transponder, as implemented within this design, performs the following functions:

1. Conversion of electrical energy into sound pressure and vice-versa.
2. Switching between the two modes of operation (RX and TX).
3. Conditioning receive signals for proper analog-to-digital conversion. Specifically, amplifying and bandpass filtering the incoming acoustic signals converted into a voltage by the reciprocal transducer.
4. Conditioning transmit signals generated by the MCU. Specifically, generating electrical signals to be converted into sound pressure by the reciprocal transducer.
5. Providing electrical energy (at appropriate voltage and power levels) for all on-board electronics.

Because the micro-transponder needs to respond to an interrogation within a few milliseconds at power levels that are appropriate for communication, switching from RX to TX is a critical component of the design, especially when maximizing the utility of the battery. To this end, the transient and steady-state performance of the analog front-end including an analysis of the power-demand of its sub-systems for active-on, stand-by, and/or quiescent operations, is presented in the following sections. The sub-systems of the design are described in detail within this chapter and are simply an extension of the information provided in and generalized by the system level block

diagram (Figure 1.1)

### **3.2 The Transducer**

A Lead-Zirconate-Titanate (PZT) piezoelectric ceramic is regularly used for the generation and reception of ultrasonic acoustic waves. PZTs of this type provide efficient, and reciprocal electro-mechanical properties that extend over large dynamic (power) ranges (greater than 150 dB re  $V_{\text{RMS}}^{\text{TX}}/V_{\text{RMS}}^{\text{RX}}$ ). “These materials, when mechanically stressed, will produce an electrical charge, and conversely, when an electrical field is applied, a mechanical strain will occur, changing the dimensional shape of the material” (Channel Industries). The PZT ceramic used in this project is a disk with diameter  $13.818 \text{ mm} \pm 0.08 \text{ mm}$  and thickness  $1.143 \text{ mm} \pm 0.05 \text{ mm}$ . It is polarized in its thickness dimension and manufactured with electrodes on both circular faces. When placed within a field of sinusoidally varying pressure waves, the physical stress caused by deflection of the disk’s face produces a congruent time varying electric potential across these electrodes. Similarly, a sinusoidally varying voltage applied across the same electrodes cause the disk’s faces to be displaced along the thickness axis. Because the crystalline structure of the ceramic is polarized in its thickness dimension, the axial movement of the disk is inversely coupled with the movement of its circular faces. For the micro-transponder application, the piezoelectric disks are excited in their radial mode at their resonant frequency of  $159.9 \text{ kHz} \pm 0.9 \text{ kHz}$ .

#### **3.2.1 Overview of the Assembly**

The utility of the transducer assembly is to provide a physical and electrical interface between the ceramic and the PCB. When receiving signals over long distances (500 m), the piezoelectric ceramic produces electrical signals as small as  $562 \text{ nV}_{\text{RMS}}$  (Section 3.2.3). Because these signals are to be detected by the receiver, any external noise must be reduced. To shield the



transducer from such noise, its assembly is designed to mimic a coaxial cable. In addition to the piezoelectric ceramic disk, the entire transducer assembly includes a brass mount, acoustic backing, electrical leads, and an acoustically transparent window (urethane potting provided by L-3 Klein Associates, Inc.). Figure 3.1 describes the physical orientation of these elements as implemented within the design (urethane potting excluded).

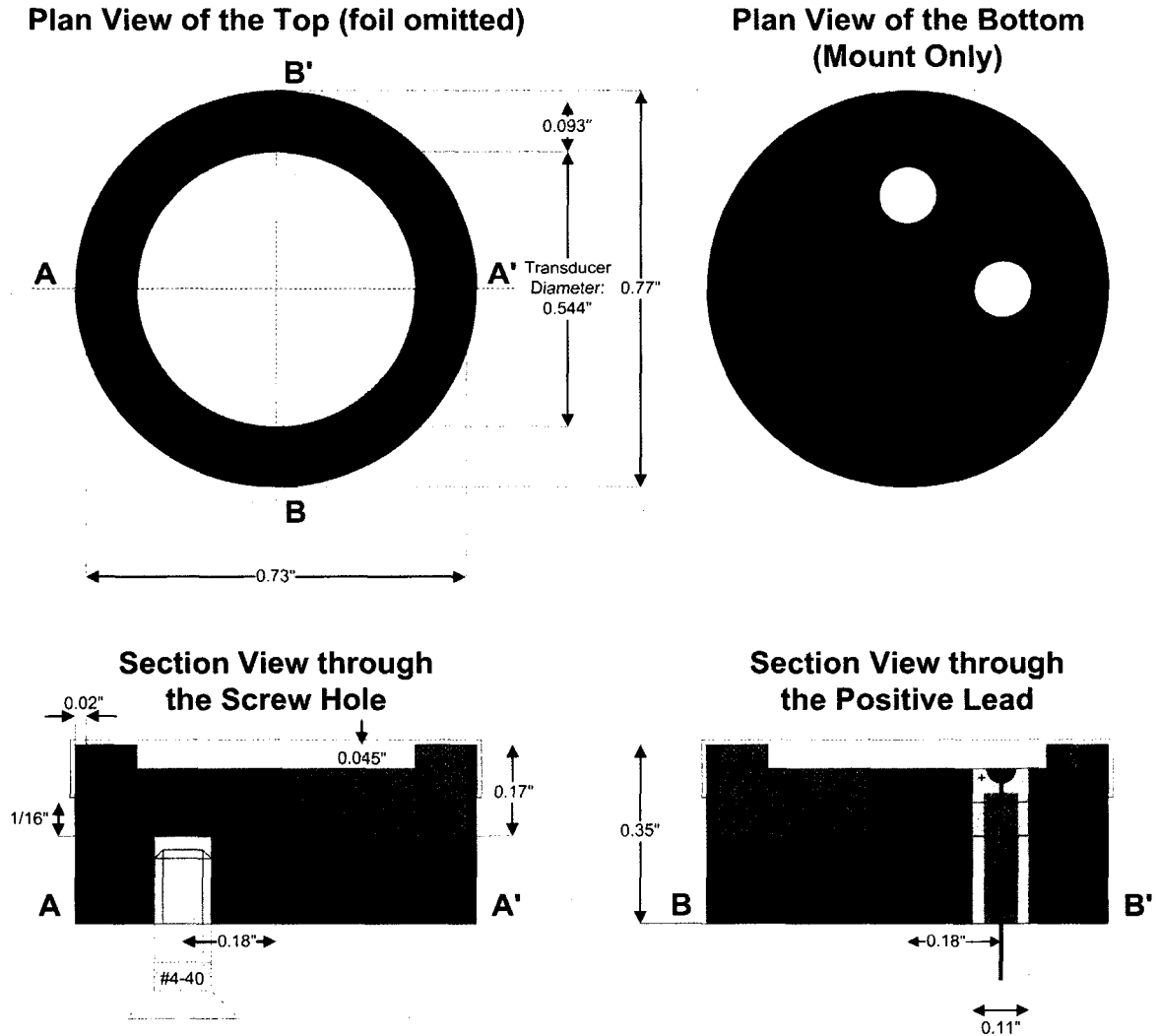


**Figure 3.1: Overview of the Transducer Assembly**

The transducer assembly is shown in plan and section views (sections annotated on the top left). The following colors are used to differentiate the different elements of this design: Red = Brass Housing, Green = Piezoelectric Ceramic Disk, Brown = Corprene, Yellow = Conductive Foil, and Blue = Insulation of the positive lead.

The utility of the brass mount is two-fold: Firstly, the brass mount physically houses the entire

transducer assembly and is attached to the backside of the PCB<sup>3</sup> with a #4-40 machine screw. Secondly, the brass mount provides electrical continuity between the outward facing electrode of the PZT disk and the negative transducer net-connection on the PCB, via a connector. A piece of copper foil (backed with highly conductive acrylic adhesive) electrically interfaces the mount with the outwardly facing electrode. The other electrode, oriented facing down into the assembly, is soldered (using SN-62 solder) to an insulated stranded 24 AWG lead. This lead extends downward through the assembly and is connected to the positive transducer net-connection on the PCB. Corprene surrounds the sides of the PZT disk and the downward facing electrode providing electrical insulation and a lossy pressure release on these faces.

To encapsulate the transducer, the entire assembly was potted within a vacuum and heat-cured within an oven at the L-3 Klein Associates facility in Salem, NH. The potting material, used in the construction of the prototype transducer, was a Navy-grade impedance-matched (density and sound-speed) urethane. This type of urethane provides an acoustic window for sound propagation and electrically insulates the entire design from (conductive) seawater. Additional details of the construction of the transducer assembly are shown in Appendix B.

### **3.2.2 Admittance / Impedance Characteristics**

The admittance ( $Y$ ) of a piezoelectric transducer fully describes its electrical characteristics. When integrated within a larger circuit topology, the transducer impedance ( $Z = 1/Y$ ) is critically important with respect to the sub-systems of the design. For resonant devices such as piezoelectric ceramics, admittance parameters are complex quantities represented by vectors in the complex plane. Figure 3.2(a) displays the vector results of these measurements<sup>4</sup> for both the potted and unpotted assemblies and (b) separates the components of admittance, conductance ( $G$ ), and susceptance ( $B$ ) for the unpotted case.

---

<sup>3</sup> Although the placement of the transducer assembly will ultimately end up on the PCB, the prototype transducer was potted within the PVC lid of a pressure housing (see Appendix B).

<sup>4</sup> These measurements were provided by Peter Runciman at L-3 Klein at the time of production.

(a)

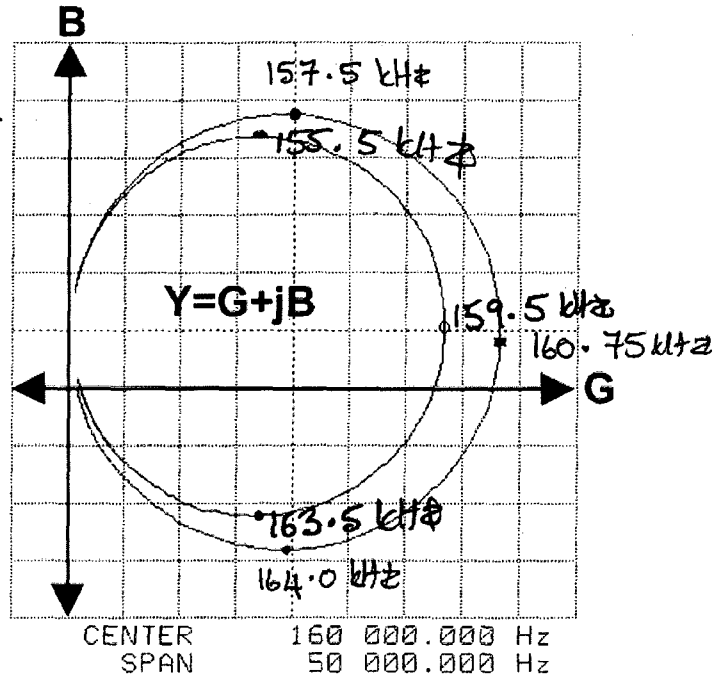
Transducer Legend:  
Black: Unpotted in Air  
Red: Potted in Water

<Horizontal>

A: G  
A MAX 9.000 mS  
A/DIV 1.000 mS

<Vertical>

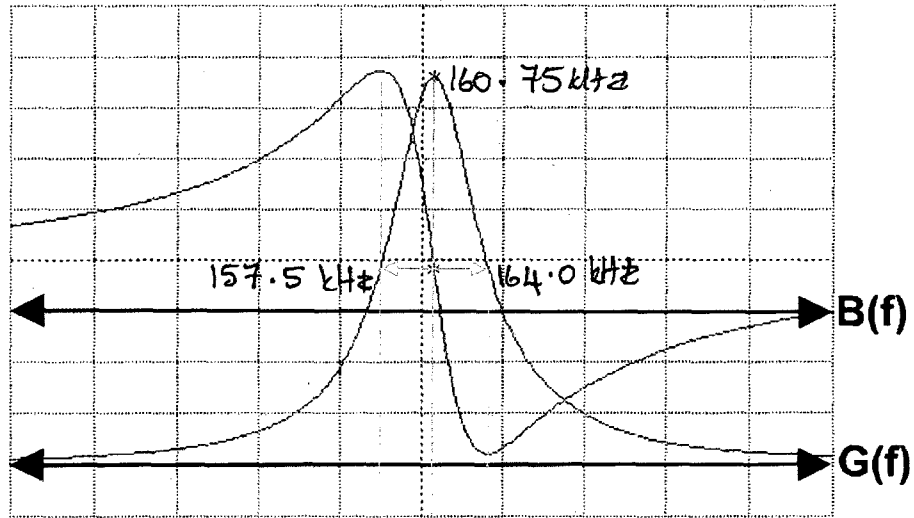
B: B  
B MAX 6.000 mS  
B/DIV 1.000 mS



SPAN=\_50000.000 HZ

(b)

A: G      B: B      \* MKR      160 750.000 Hz  
A MAX 9.000 mS      REAL      7.60492 mS  
B MAX 6.000 mS      IMAG      833.861 μS



A/DIV 1.000 mS      CENTER      160 000.000 Hz  
B/DIV 1.000 mS      SPAN      50 000.000 Hz  
SPAN=\_50000.000 HZ

**Figure 3.2: Vector Admittance Measurements of the Transducer**

(a) The vector admittance curves for the unpotted and potted transducers are shown and annotated by black and red, respectively. (b) Conductance and susceptance for the unpotted transducer are separated and plotted with respect to frequency. Admittance, conductance, and susceptance are expressed in units of mS for all plots.

Piezoelectric ceramics are often characterized in the admittance plane because their equivalent electromechanical properties can be simplified, about their resonance, to a series of complex motional parts in parallel with electrically ‘blocking’ parts (Wilson, 1988). From inspection, the motional resonance of the transducer is found at the point of maximum conductance ( $F_m = 159.5$  kHz for the potted transducer). The inverse of conductance at this frequency describes the electrically equivalent motional resistance ( $R_m = 148 \Omega$  for the potted transducer). This equivalent component describes the radiation of sound from the mechanical movement of the piezoelectric ceramic. The positive susceptive offset in the admittance plane describes the effects of the dielectric material within the PZT ceramic. The blocked electrical capacitance ( $C_0$ ) is calculated at the resonant frequency using the following equation:

$$C_0 = \frac{B(f = F_m)}{2\pi F_m} \sim 1 \text{ nF}$$

The frequency dependence of the piezoelectric transducer is electrically modeled as an inductor and capacitor in series with the motional (radiation) resistance. The motional inductance ( $L_m$ ) is a function of the transducer’s bandwidth, BW (Hz), and is calculated using the following equation:

$$L_m = \frac{R_m}{2\pi BW}$$

A transducer’s bandwidth is characterized as the half-power range of frequencies with which it most efficiently radiates sound. This bandwidth correlates with susceptance transitioning from a local maximum to a local minimum ( $\sim 8$  kHz for the potted transducer). The equivalent motional inductance of the potted transducer is calculated as  $\sim 2.94$  mH. The final component of the simplified model is the equivalent motional capacitance ( $C_m$ ). This capacitance is also a function of the motional resonance and is calculated for the potted transducer by the following equation:

$$C_m = \frac{1}{\omega_m^2 L_m} \sim 338 \text{ pF}$$

Because this motional capacitance is **not** ‘small’ compared to the blocked electrical capacitance,

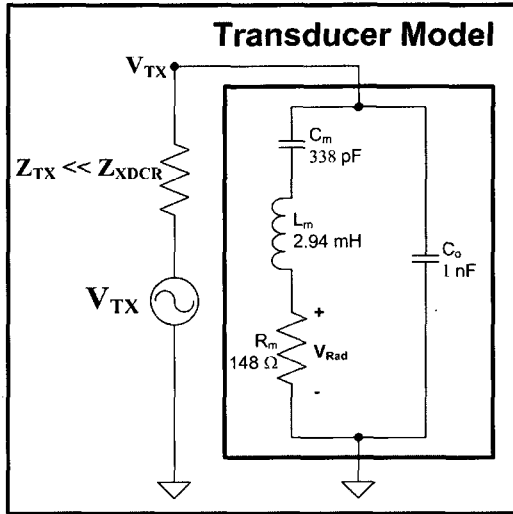
the effects of parallel (hydrophone) resonant frequency enhancement **cannot** be ignored. A frequency analysis of the equivalent piezoelectric transducer model illustrates this shift in resonant frequency when operating the device as a hydrophone. Figure 3.3 depicts the non-reciprocal frequency response of the transducer, but does so by using a lumped element model analysis that cannot be measured.

The lumped element model analysis compares the frequency response of the transducer for its two modes of operations: projection and reception. When operated as a projector, the transducer acts as an electrical load. The micro-transponder utilizes a switching amplifier to drive this load (Section 3.6). The full-bridge driver of this amplifier acts as a low impedance source and therefore the voltage drop across the Thevenin equivalent source impedance ( $Z_{TX}$ ) is negligible (Figure 3.3(a)). From inspection, the voltage delivered to the motional (radiation) resistance is shown to be independent of the blocked capacitance<sup>5</sup>. However, when the transducer is used as a hydrophone and fed into a high impedance load (Figure 3.3(b)), the effects of the blocked capacitance are observed. The magnitude of the frequency response is shifted from the motional resonance at 159.5 kHz to the so-called parallel “anti-resonance” at 184.6 kHz. This effect is shown in Figure 3.3(c). A common solution for cancelling this blocked capacitance is to ‘tune’ the circuit with an inductive element (Airmar, 2000). However, shunting the outputs of the full-bridge driver, in this case, has devastating effects. The inductive element acts as a DC short across the terminals of this device and conducts current from supply to ground through this (inductive) leg. The receiver, therefore, was designed with this enhancement problem in mind.

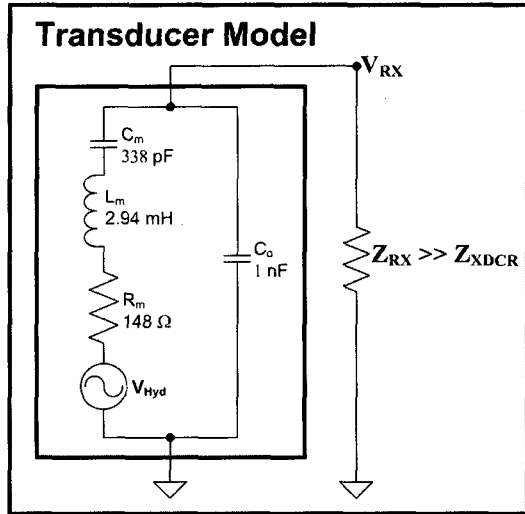
---

<sup>5</sup> But the power delivered to the load is dependent upon the input impedance of the transducer which is indeed a function of this blocked capacitance. The overall effect of this capacitance, about the resonance, is negligible because its reactive magnitude is ~6.7 times that of the radiation resistance.

(a) Projector Operation



(b) Hydrophone Operation



(c) Frequency Response of the Transducer Model (\* indicates normalization)

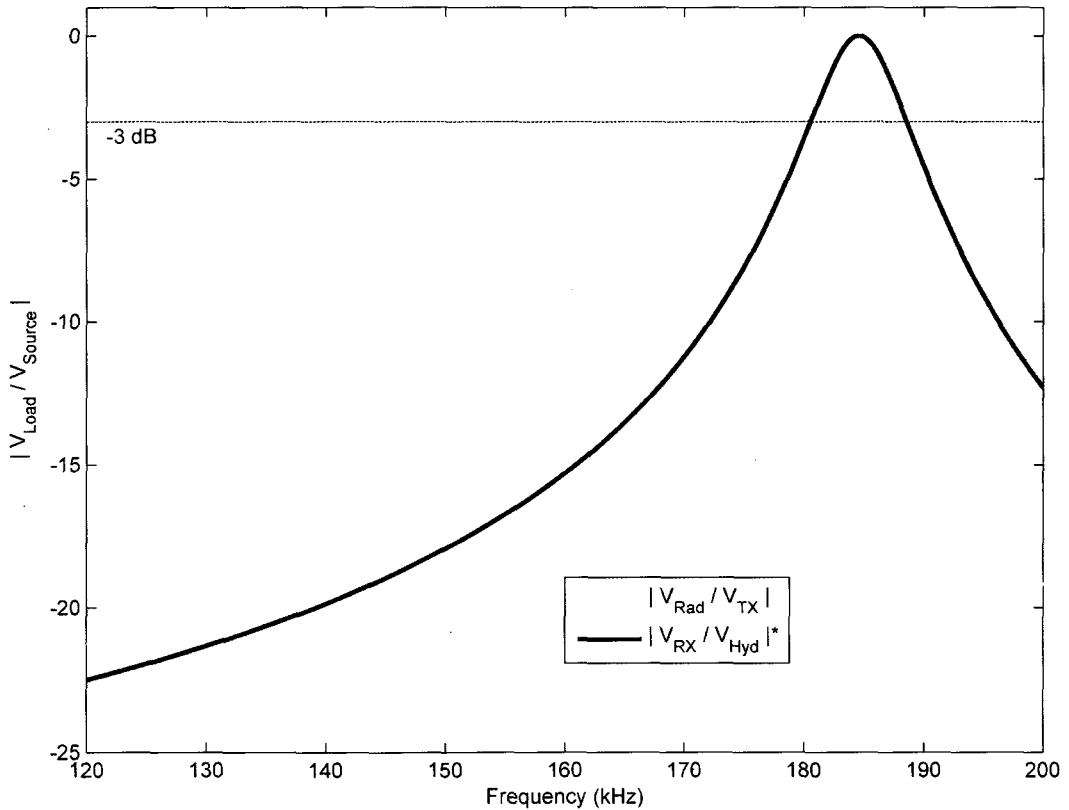


**Figure 3.3: Equivalent Circuit Model of the Transducer**

(a) When “projecting,” the transducer is driven by a low impedance switching amplifier and the equivalent circuit model of the transducer is analyzed as an electrical load. The green line in (c) displays the magnitude of the frequency response for this case. (b) When “listening,” the transducer’s signal is fed into a high impedance load and the equivalent circuit model of the transducer is analyzed as a source. The blue line in (c) displays the normalized magnitude of its frequency response for this case.

### **3.2.3 Electro-Acoustic Response**

The electro-acoustic response of an underwater transducer is defined as its ability to transform electric energy into acoustic energy and vice-versa. The ability to do so is a function of the transducer's material(s), the method with which it is mounted, and the interface(s) between it and the water. Although the electrical characteristics of the transducer are simplified by an equivalent lumped model, the electro-acoustic response is generally too complex to describe in closed form and therefore measurements are made. Tank tests within Klein's acoustic calibration facility measured the performance of the transducer in terms of both its electro-acoustic responses and its directivity (Section 3.2.4).

The Transmit Voltage Response (TVR) defines the amount of pressure (in  $\mu\text{Pa}$ ) that is produced by a transducer when applying a known sinusoidal voltage ( $V_{\text{RMS}}$ ). This response is measured using a calibrated reference hydrophone in a controlled test environment; namely, in water at a known distance on the Maximum Response Axis (MRA) of the transducer. Because the response of the reference hydrophone is known and because the test environment is well defined<sup>6</sup>, the magnitude of the signal applied to the test transducer is compared with the actual pressure it produces (referenced at 1 m from its face). A LabView program, developed by Barbara Kraft, controls Data Acquisition (DAQ) hardware that captures the signal(s) fed into the test transducer and compares them with the signal(s) received by the hydrophone. This program triggers a function generator that feeds a linear power amplifier and drives the test transducer with a known signal, whereby the signal is transduced into an acoustic pressure wave. The sound propagates through the water and is received by and transduced into a congruent time-varying voltage using a Reson 4038 hydrophone. The hydrophone's electrical signal is fed into a voltage pre-amplifier / bandpass filter and is captured using the same DAQ. Refer to Appendix Section C.1 for a detailed description of the calibration test setup used to measure the TVR. The

---

<sup>6</sup> Sound-Speed is measured; transmission losses are calculated from far-field approximations; and multipath is avoided by the signal processing of finite duration CW bursts in their steady-state.

LabView program processes the waveforms and calculates the TVR of the test transducer over the frequency band of 140 – 180 kHz in 500 Hz steps (Figure 3.4).

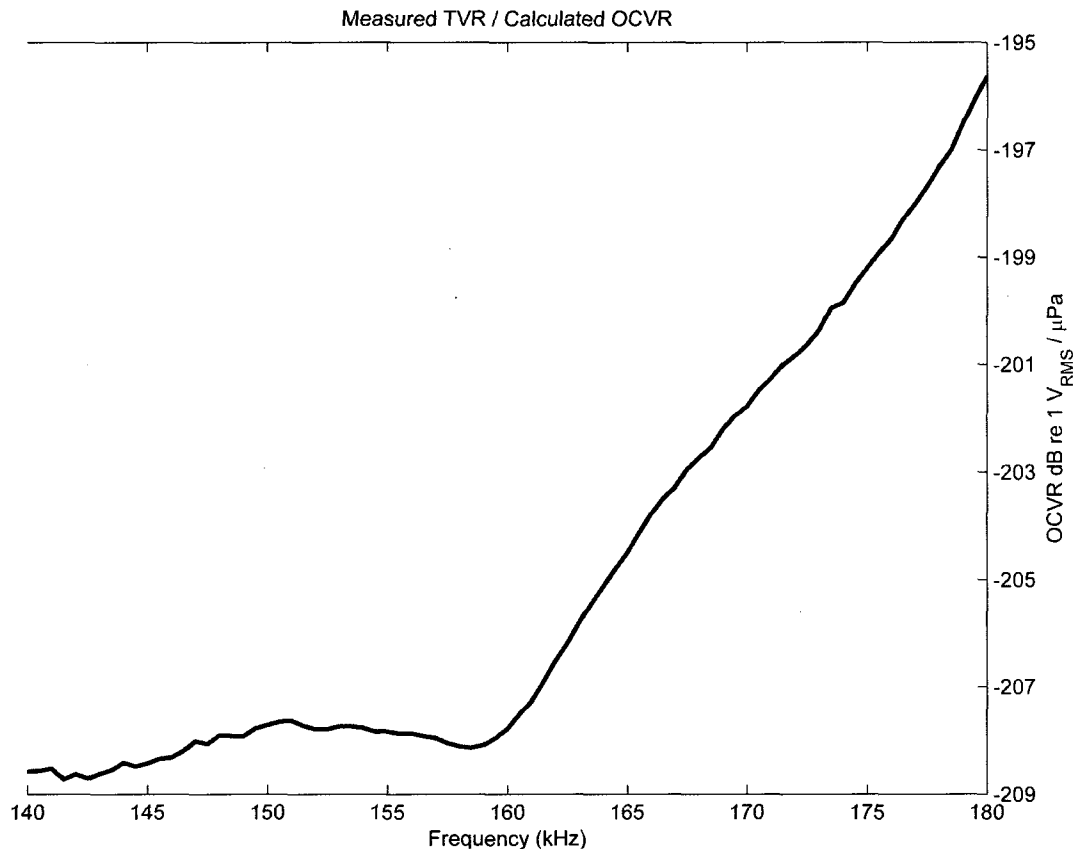


**Figure 3.4: Transmit and Receive Responses of the Transducer**

As calibrated within a test tank, the Transmit Voltage Response (TVR) is measured as a function of frequency and plotted in green. The Open-Circuit Voltage Response (OCVR) is plotted in blue and calculated based on the TVR and impedance measurements of the transducer.

The Open-Circuit Voltage Response (OCVR) is the amount of voltage ( $V_{RMS}$ ) that is produced by a transducer for a given incident pressure field. This acousto-electric response can be measured using a calibrated projector similar to the TVR method. Because the received voltages were very small ( $\sim 170 \mu V_{RMS}$ ) and the electrical noise that coupled onto the cable connecting the transducer to the top-side equipment was of similar magnitude, a reasonable assessment of the relative amplitudes of received signals could not be made. Hence, OCVR measurements were, instead, calculated using the following equation where  $f$  is the frequency in



Hz (de Moustier, 2005):

$$OCVR(f) = TVR(f) - 20\log_{10}(f) - 294 - 20\log_{10}(|Z(f)|)$$

Using the measurements of its TVR and Impedance ( $Z$ ), the OCVR is calculated for the test transducer.

The TVR and OCVR define the transmit and receive responses of the designed transducer, respectively. Since the TVR and the OCVR are defined at the leads of the transducer, the bandwidth and resonant frequency are a function of the equivalent series impedance as defined by the equivalent circuit model (Section 3.2.2). When driving its leads at a particular voltage and frequency, the amount of sound-power output by the transducer is a function of its TVR. The TVR has a maximum response of 146.8 dB re 1  $\mu\text{Pa} / V_{\text{RMS}}$  at 1 m at  $F_0 = 160$  kHz and has a -3 dB bandwidth of 11.1 kHz. To maximize the utility of the transducer when transmitting, the transducer will be used about its resonant frequency. Because it was determined that communication between the APS and the transmitter requires a Source Level (SL) of 167 dB re 1  $\mu\text{Pa}$  at 1 m at a range of 500 m (Section 2.3.3), the transducer should be driven at an average voltage of **10.2**  $V_{\text{RMS}}$  at  $F_0 = 160$  kHz. At this level, the amount of power that must be driven ( $P_d$ ) is a function of the transducer's impedance ( $Z(f)$ ):

$$P_d = \frac{(V_{\text{RMS}})^2}{|Z(f = 160 \text{ kHz})|} = \frac{(10.2)^2}{149 \Omega} = 0.70 \text{ W}$$

The transmit amplifier (section 3.6) must therefore deliver **~0.7 W** to the transducer at a frequency of 160 kHz with a RMS voltage of **~10.2 V**.

When operated as a hydrophone<sup>7</sup>, the amount of voltage produced by the transducer is a function of its OCVR. The OCVR is nominally **~ -208 dB** re 1  $V_{\text{RMS}} / \mu\text{Pa}$  from 140 kHz - 160 kHz and then it monotonically increases up to the parallel anti-resonance frequency. From our initial assumptions of Noise Level (NL) and SNR requirements at 500 m ranges, a Sound

---

<sup>7</sup> and fed into a high impedance load that is defined as  $Z_L \gg |Z_{\text{XDCR}}(f)|$

Pressure Level (SPL) of at least 83 dB re 1  $\mu$ Pa would be detectable by the system (Section 2.3.3). Incident sinusoidal pressure waves of this magnitude would therefore be converted to an average voltage of 562 nV<sub>RMS</sub> (or 1.59  $\mu$ V<sub>P-P</sub>) by the designed transducer. Assuming that signals are digitally detectable when their equivalent peak-to-peak voltages are 5 times that of the quantization level of a 12-bit ADC (Section 3.5.3) or 3.66 mV, a voltage pre-amplification gain of  $\sim$  67.25 dB is required by the analog receiver (Section 3.5.2).

### **3.2.4 Directivity**

The directivity of a transducer describes how the pressure field generated by the transducer varies about the non-radial spatial components of azimuth ( $\theta$ ) and elevation ( $\phi$ ). Likewise, the directivity describes how the acoustic sensitivity of the transducer is a function of spatial direction. The performance of the micro-transponder is further constrained<sup>8</sup> in range by the directivity of the transducer. As the transducer becomes more directional, the physical orientation of the transducer becomes more critical for APS / transponder communication and therefore limits its utility in some tracking applications. Beam pattern measurements analyze the transducer's performance as a function of space and are normalized by V<sub>RMS</sub> as measured at the MRA. Using the same signal processing and data acquisition methodology implemented in Section 3.2.3, the beam pattern of the test transducer was measured by comparing the relative amplitudes of pressure generated by the test transducer with the voltage applied across its leads at  $F_0 = 160$  kHz. A LabView program controls the rotation of the pole-mounted transducer to make far-field calibrated measurements of pressure about both axes in 2 degree steps. Because the forward projecting face of the transducer is symmetric, the beam pattern was assumed to be symmetric about the MRA in both  $\theta$  and  $\phi$ . Therefore, the beam pattern is simplified and only measured in one dimension by rotating the pole and comparing the calibrated receive response

---

<sup>8</sup> although the noise received by the transducer will be reduced

with measurements made along the MRA (refer to Figure C.1 for a description of the test setup used to measure the beam pattern). Figure 3.5 shows the result of the beam pattern measurements of the transducer.

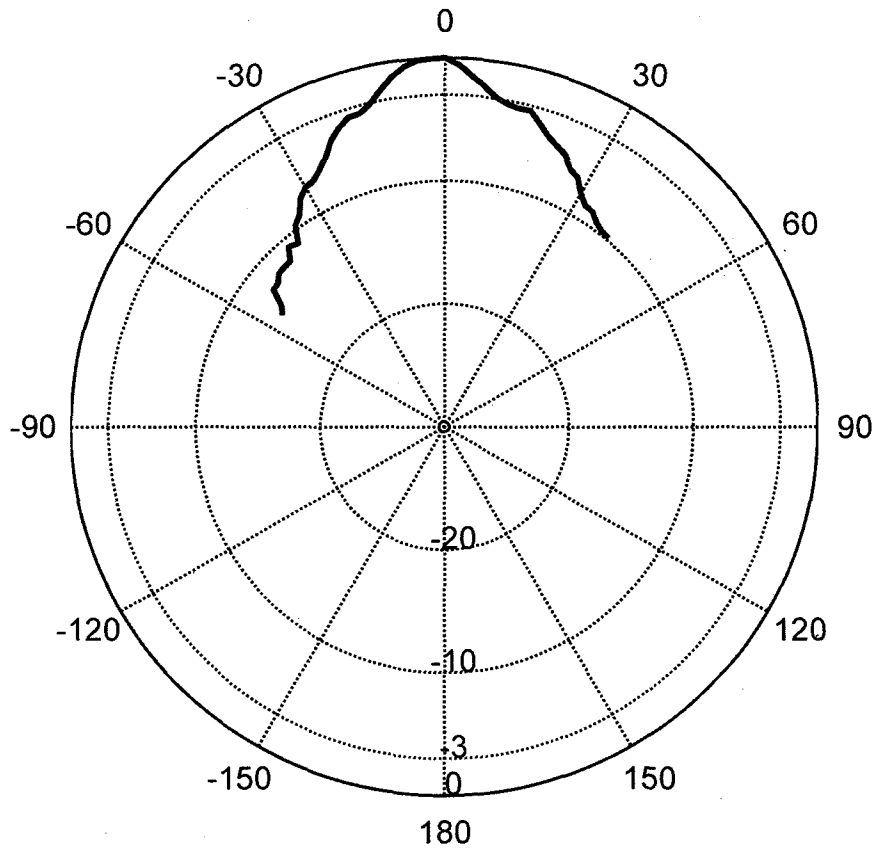


**Figure 3.5: Measured Beam Pattern of the Potted Transducer,  $F_0 = 160$  kHz**

This plot illustrates the directivity of the designed transducer. TVR measurements were made as a function of  $\theta$  and normalized to the MRA TVR.

The results show how the  $-3$  dB beamwidth is  $\sim 20$  degrees and the  $-10$  dB beamwidth is  $\sim 70$  degrees. The irregularities of the beam pattern suggest that either pressure was not uniformly distributed across the face of the transducer and/or destructive interference occurred. Pressure distribution was unknown because the ceramic disk was operated about its axial resonance and not its thickness resonance while destructive interference might have been caused by the brass mount holding the ceramic or the PVC surrounding the cavity in which the transducer assembly was potted within (Appendix B).

### **3.3 The Microcontroller**

A TI MSP430 mixed signal microcontroller uses an internal ADC to interface the analog received signals with digital circuitry (Section 3.5.3). This MCU executes an algorithm that digitally demodulates and detects these received signals, generates an encoded reply, and directs the transmit IC to drive this reply onto the transducer (description in Chapter IV). To minimize the power-demand when communicating with an APS over long ranges (up to 500 m), the micro-transponder switches between RX and TX operations under the direction of the MCU. The MCU appropriately controls which sub-systems are active and which sub-systems are inactive. Because the transmit amplifier uses a large amount of power when transmitting ( $\sim 1.2$  W vs. 6.2 mW in RX mode), its function is shut-down by the MCU when receiving. Likewise, the analog receiver can be shut down to demand no quiescent current. Although this functionality is not as critical to the present manifestation of the micro-transponder<sup>9</sup>, controlling the analog receiver will become important when extending the deployment duration of the transponder by implementing a polling routine that periodically turns off the analog receiver and puts the MCU to sleep. The MCU enables and disables the functions of the micro-transponder's sub-systems using the following digital / switching logic lines:

1. Ground Enable or  $GND_{EN}$ : Controls the negative lead of the transducer (Section 3.4).
2.  $LDO_{OFF}$  or Not  $LDO_{EN}$ : Controls power delivered to the analog receiver (Section 3.5.1).
3. Boost Enable or  $BOOST_{EN}$ : Controls the operation of the transmit amplifier's boost convert (Section 3.6).
4. Driver Enable or  $DRV_{R_{EN}}$ : Controls the output impedance ( $Z_{DRV_{R}}$ ) of the transmit amplifier's full-bridge drivers (Section 3.6).

These lines are shown by the circuit topology of the MCU (Figure D.1 of Appendix D) and mentioned throughout this chapter.

---

<sup>9</sup> Because the transmitter demands many orders of magnitude more power than the receiver, it can be argued that keeping the receiver turned on all the time is appropriate in this design.

### **3.4 Switching between RX and TX Modes and the Function of the Grounding FET**

Because the transducer is used differently when transmitting or receiving, the MCU controls the flow of current into and out of the negative lead of the transducer by opening and closing the channel of an N-MOSFET. The analog receiver utilizes a single-ended topology (Figure 3.9). When receiving, the negative lead of the transducer must be shunted to ground and the transmit IC's drivers disabled. The voltage produced by the piezoelectric ceramic is then able to flow from ground to the receive circuitry because its equivalent input impedance is lower than the disabled driver's equivalent impedance. When doing so, the MCU outputs  $V_{CC}$  onto the gate of the N-MOSFET and because its source is connected directly to ground and  $V_{GS} = V_{CC} = 3\text{ V}$ , the channel of the N-MOSFET is opened and signal flows from ground to the negative transducer lead.

Conversely when transmitting, signals are differentially driven by the switching amplifier and current flowing through the transducer is a function of the driver's operation (Figure 3.15). When doing so, the leads of the transducer must be controllable by this amplifier. When the boost voltage ( $V_{Boost}$ ) is driven onto the positive transducer lead, the analog front-end of the receiver is current and voltage limited by the combination of a series resistor ( $R_{LIM}$ ) and ground shunting back-to-back diodes. When driving this circuit into its non-linear operation, the analog front-end is isolated from the transmitter circuit because  $R_{LIM}$  is picked to be much larger than the impedance of the transducer. Therefore, current predominately flows into the transducer and not into the receiver when driving  $V_{Boost}$  onto the positive-transducer net-connection. To enable signal flow to be controlled by the differential amplifier, the MCU drives the gate of the N-MOSFET low and the channel connecting the drain to source is 'cut-off.' Figure 3.6 illustrates the utility of the N-MOSFET and simplifies the view of the sub-system functions of the micro-transponder's analog design.

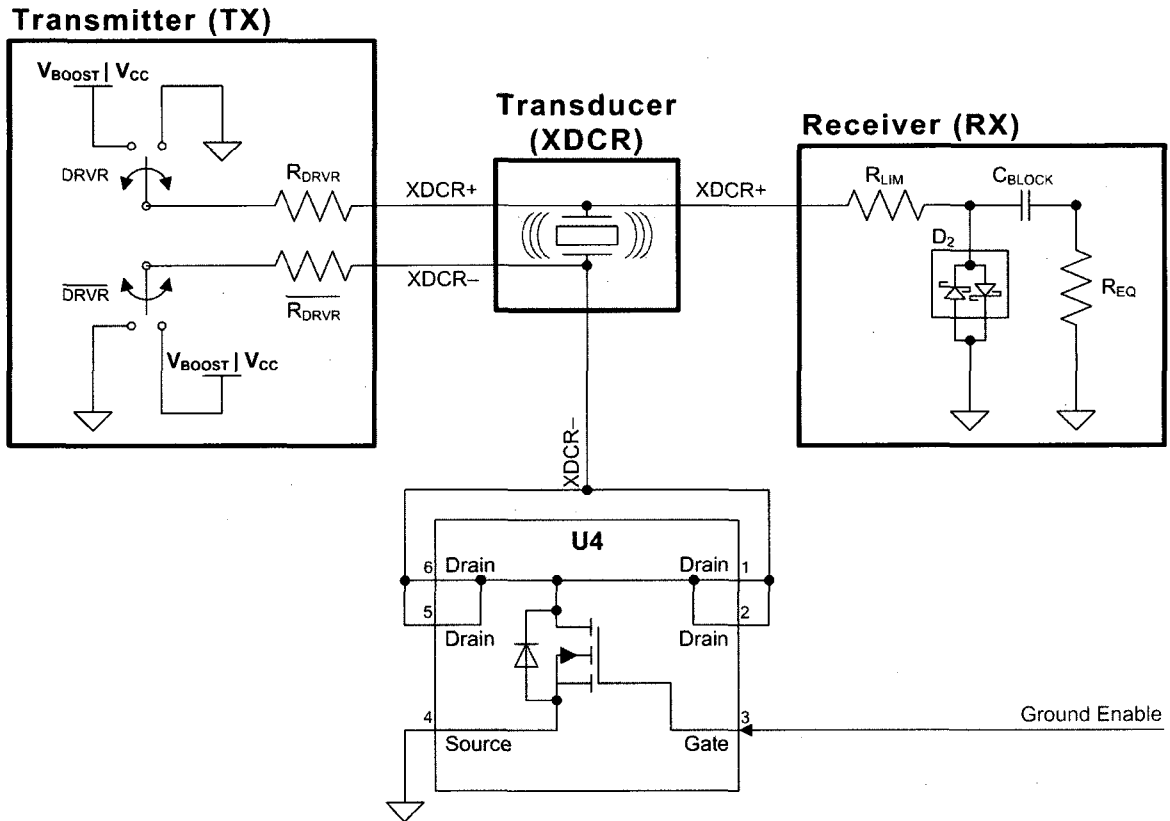


**Figure 3.6: Grounding FET Topology Implemented in the Design**

Circuit Topology of the N-MOSFET used to shunt the negative lead of the transducer when receiving. Its function is controlled by the MCU. The equivalent circuit models of the transmitter and receiver are shown and describe their relevant functions from the perspective of the transducer.

### 3.5 The Receiver

The basic function of the analog receiver is to amplify signals within the carrier band, filter those not in this band, and drive the ADC inputs of the MCU. Because of (1) the transducer's receive-sensitivity, (2) the limited dynamic range of the digital detector, and (3) the nominal amplitude of received signals communicated over the channel, voltages generated by the piezoelectric transducer should be amplified by 67 dB when interrogated by an APS at 500 m (Section 3.2.3). The carrier band is demodulated through a sub-sampling process called frequency translation (Section 4.2.2). Because the spectrum is intentionally aliased, signals are bandpass filtered before being digitally converted. This ensures that out-of-band signals are not 'folded' into the sub-sampled spectrum. The ADC interface itself is also fundamental to receiver

design. Because the response time of the ADC is a function of the circuit that drives it, the receiver is designed with a low impedance output buffer to reduce the conversion time required for accurate sampling (Section 3.5.3).

The design of the analog receiver is comprised of the following parts: voltage amplifiers, Bandpass Filters (BPF), and buffers. In addition to performing these functions, internal noise must be minimized so it too does not interfere with received-signal detection. The following sources of noise are identified within the design process:

1. Electrical, thermal, and shot noise from discrete circuit components within the signal path of the received signals.
2. Digital switching noise created by the MCU when converting analog signals into digital samples.
3. Oscillatory noise caused by the gain of the receiver and the coupling of signal, power, and ground traces on the PCB.

When implementing the design, these noise sources were reduced by physically separating the analog and digital traces on the PCB and minimizing the overall path length of the analog-receive circuit (Appendix E). Because the aim of the analog receiver was to amplify signals and an effort was made to reduce the noise in this signal path, the generic term “Low-Noise Amplifier (LNA)” will be used throughout the text to describe the analog receiver<sup>10</sup>.

### **3.5.1 Isolation of the Receiver’s Power Supply**

A Low-Dropout Voltage Reference (LDO  $V_{REF}$ ) is additionally implemented to isolate the power plane of the analog receiver and allow for the analog receiver to be shut down. The LDO  $V_{REF}$  IC is controlled by and interfaced with the MCU (using LDO<sub>OFF</sub>). When enabled, it provides a regulated voltage output of 2.8 V to the analog front-end of the receiver. This IC is placed on the topside of the PCB and it supplies power to the analog receiver (Figures 3.7 and 3.9

---

<sup>10</sup> although its noise figure was not measured

and Appendix Figures E.3 and E.4). Because the LNA applies gain to the received signal in three stages (Figure 3.9), the power provided to a section is further isolated and passively filtered by an ‘RC’ Lowpass Filter (LPF).

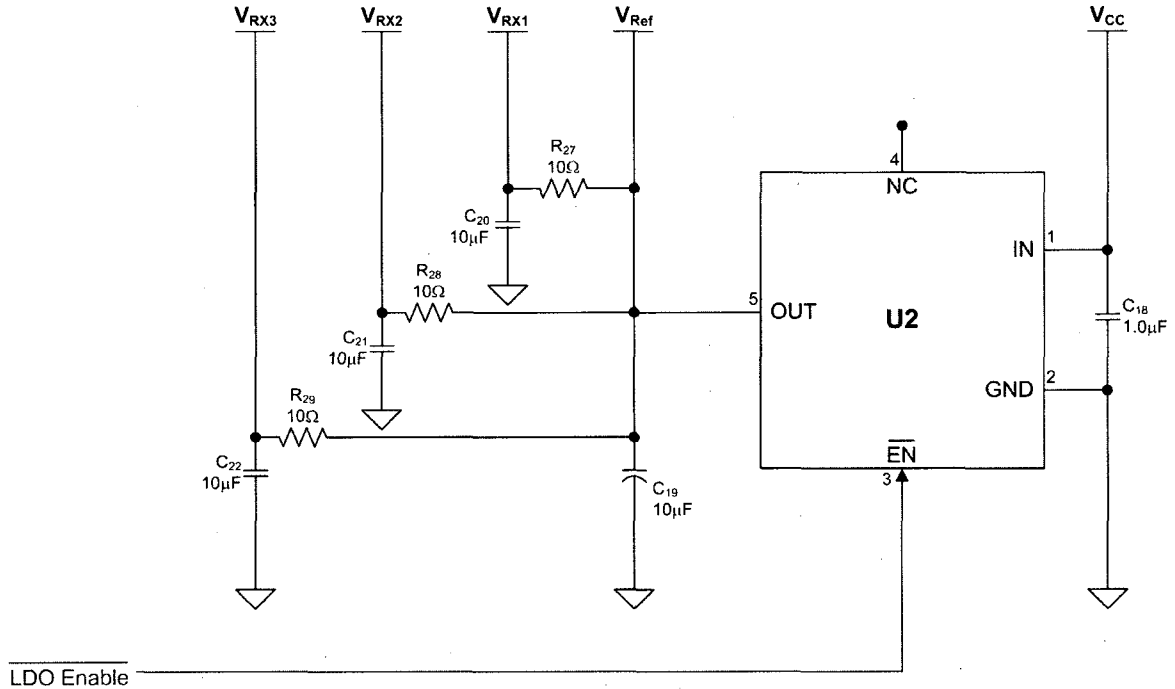


**Figure 3.7: Circuit Topology of the Receiver’s Isolated Power Supply**

When enabled by the microcontroller, a Low Drop-Out (LDO) Voltage Reference ( $V_{REF}$ ) IC provides regulated power to the three sections of the receiver. Additional lowpass filtering isolates the gain stage sections of this design.

Although the LDO  $V_{REF}$  does not introduce much noise to the receiver’s supply within the operating band of 155-165 kHz (less than -66 dB as inferred from the TI data sheet, SLVS210D, 2001), the output noise is further reduced by lowpass filters (LPF). The RC LPFs ( $R = 10 \Omega$ ,  $C = 10 \mu F$ ) are positioned physically close to the LNA section which they supply and provide ~40 dB of isolation about the receive-band (155-165 kHz):

$$|H(f)| = \left| \frac{V_{RX}}{V_{REF}} \right| = \frac{1}{\sqrt{1 + (2\pi f RC)^2}} \Rightarrow |H(f = 160 \text{ kHz})| = -40 \text{ dB}$$

These filters are designed with a time constant ( $\tau$ ) of 0.1 ms and a cutoff frequency of ~1.6 kHz.

Figure 3.8 shows the transient start-time of the LDO  $V_{REF}$  and the filtered supply lines that



provide power to the sections of the LNA.

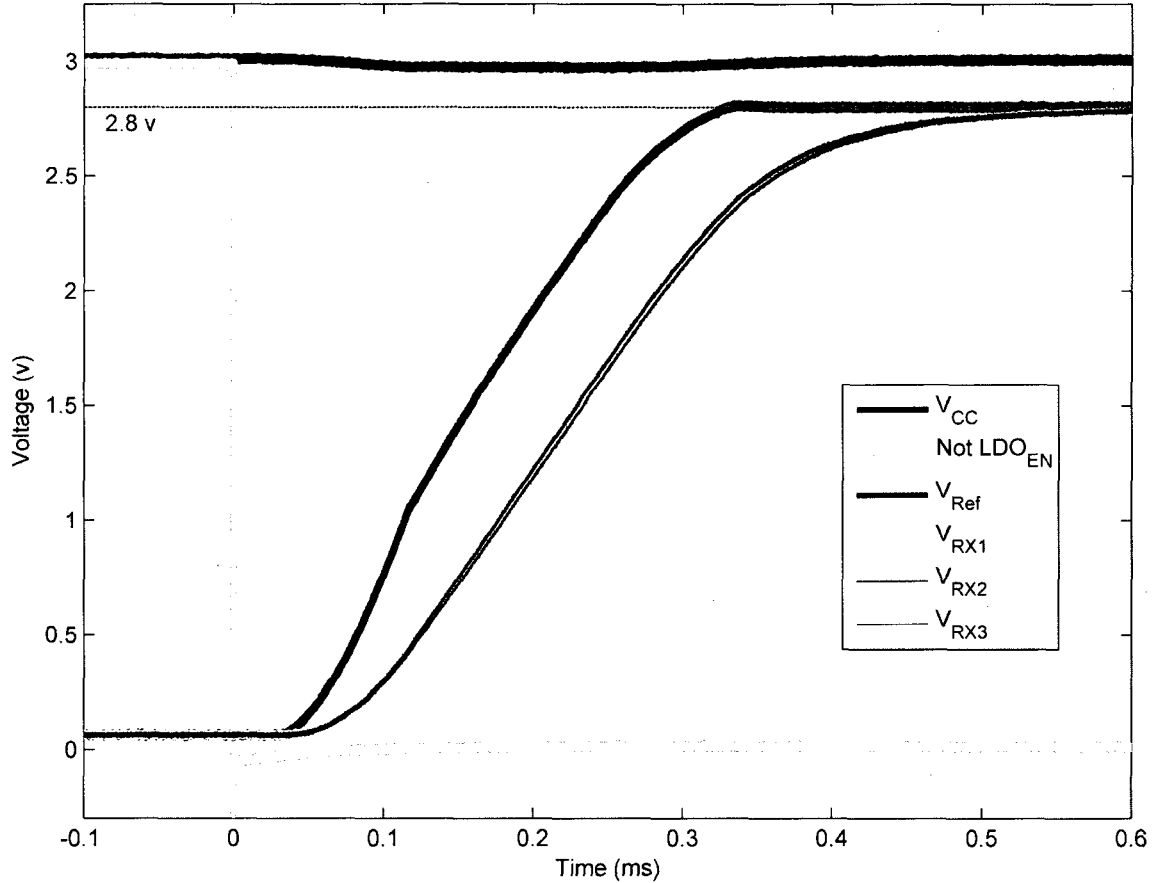


**Figure 3.8: Transient Operation of the LDO  $V_{REF}$**

The LDO  $V_{REF}$  is active-low enabled and produces a stable 2.8 V output within 0.33 ms of startup. Because RC lowpass filters are used to isolate the gain stages of the receiver, an additional delay of 0.27 ms is expected before their steady-state is reached.

The 2.8 V steady-state output from the LDO  $V_{REF}$  is realized after a startup delay of  $\sim 0.6$  ms.

The data sheet of the TI LDO  $V_{REF}$  IC states its quiescent current consumption for standby and operational modes: 1  $\mu\text{A}$  and 17  $\mu\text{A}$ , respectively (Texas Instruments, SLVS210D, 2001). It is therefore expected that the power-demand of this IC with  $V_{CC} = 3\text{V}$  will be 3  $\mu\text{W}$  when ‘off’ and 51  $\mu\text{W}$  when ‘on’ for receiving.

### **3.5.2 The Low-Noise Amplifier / Bandpass Filter**

The analog front-end of the receiver is designed and built using discrete circuit elements to achieve desired performance criteria (Sections 3.5) at acceptable current consumption levels. This design provides a voltage gain of 67.7 dB, filters signals within the 154 – 166 kHz band, and drives the ADC of the MCU at an output impedance of 240  $\Omega$ . When performing these functions, it demands 1.63 mW. The analog receiver utilizes a simple circuit topology consisting of Bipolar Junction Transistors (BJT) and passive ‘LRC’ tank filters. Because of their high transconductance, BJTs are implemented in a Common-Emitter/Common-Collector (CE/CC) cascade configuration to fully utilize the Gain Bandwidth Product (GBW) of the amplifier with little compromise<sup>11</sup> of current consumption (Sedra et. al., 1998). Figure 3.9 describes the circuit topology of the analog receiver and illustrates the functions of its discrete design.

The analog receiver is realized in three gain-stage sections. Each section provides voltage amplification ( $A_V$ ) and bandpass filtering. The first section provides the highest realizable gain<sup>12</sup> and it is the most frequency selective. The other two sections are less selective and use negative feedback to provide moderately less gain. When cascaded, the transfer functions ( $H(\omega)$ ) of the sections multiply accordingly. The measured frequency response of the micro-transponder’s analog receiver is shown in Figure 3.10 and the following table summarizes its performance:

**Table 3.1: Measured Performance Summary of the LNA / BPF Analog Receiver**

Because of ‘LC’ component variances, the center frequency varies from stage to stage. Cascading the non-symmetric frequency responses of these sections therefore affects the overall output gain, center frequency, and bandwidth as realized at  $RX_{OUT2}$  and  $RX_{OUT3}$ .

	<u><math> A_V (f = F_0) </math></u>	<u><math>F_0</math> (kHz)</u>	<u>BW (kHz)</u>
$RX_{OUT1}$	34.2 dB	161.5	15
$RX_{OUT2}$	51.7 dB	158.3	11.8
$RX_{OUT3}$	67.7 dB	162.5	12.2

<sup>11</sup> The amplifier’s performance is highly dependent upon the characteristics of the BJT in this configuration and variation in its performance will suffer as consequence.

<sup>12</sup> As limited by the bias-current, the Q of the inductor, and the loading of the input resistance to the next CC/CE cascade section.

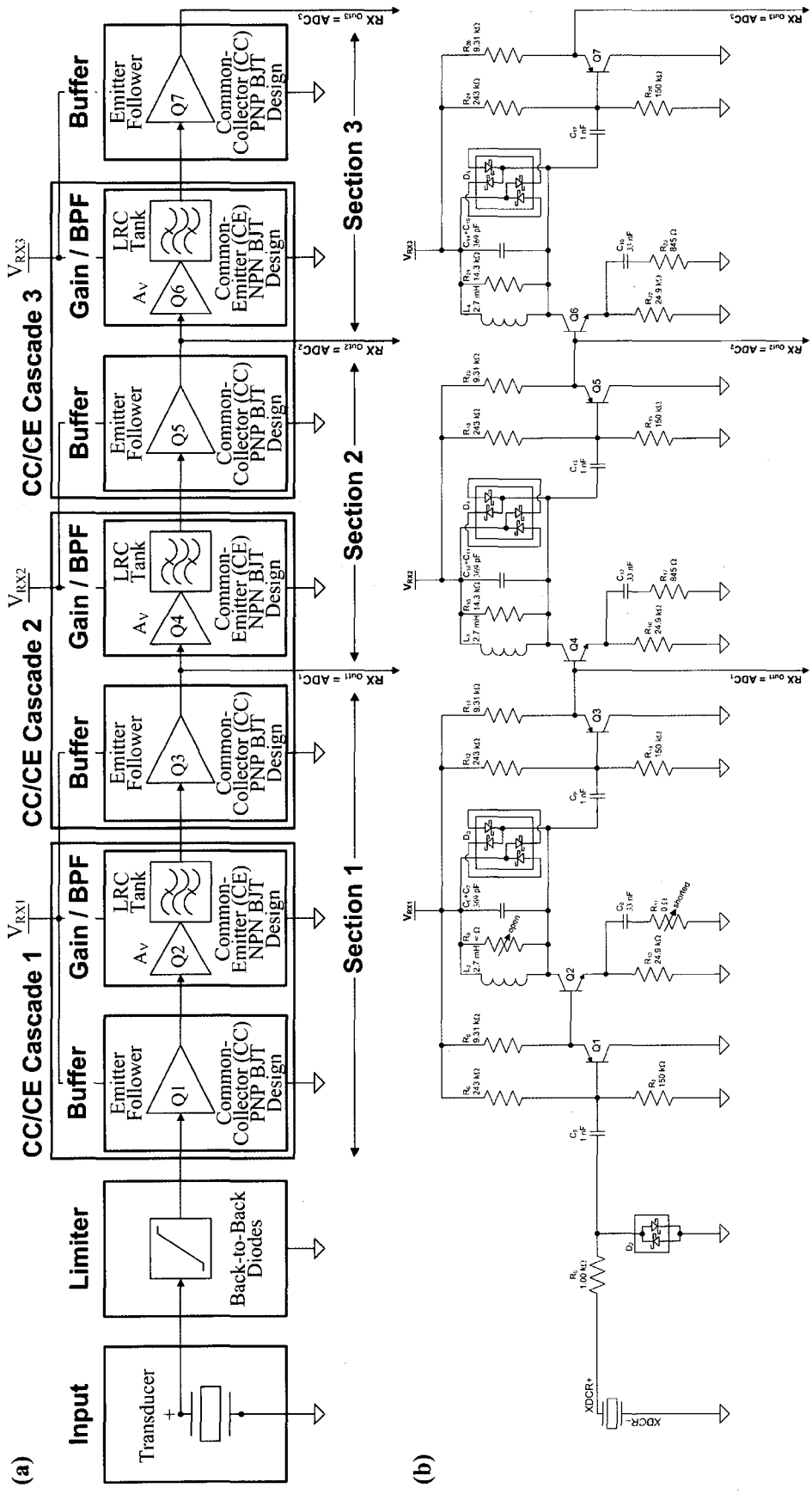


**Figure 3.9: Overview of the Analog Receiver Design**  
 The gain stages of the analog receiver are isolated by buffers which drive received signals into the ADC inputs of the MCU. The circuit topology of the discrete transistor design is shown (a) and its parts are reflected in the block diagram (b). This design is based on the CC/CE cascade configuration of two bipolar transistors: PNP and NPN, respectively.

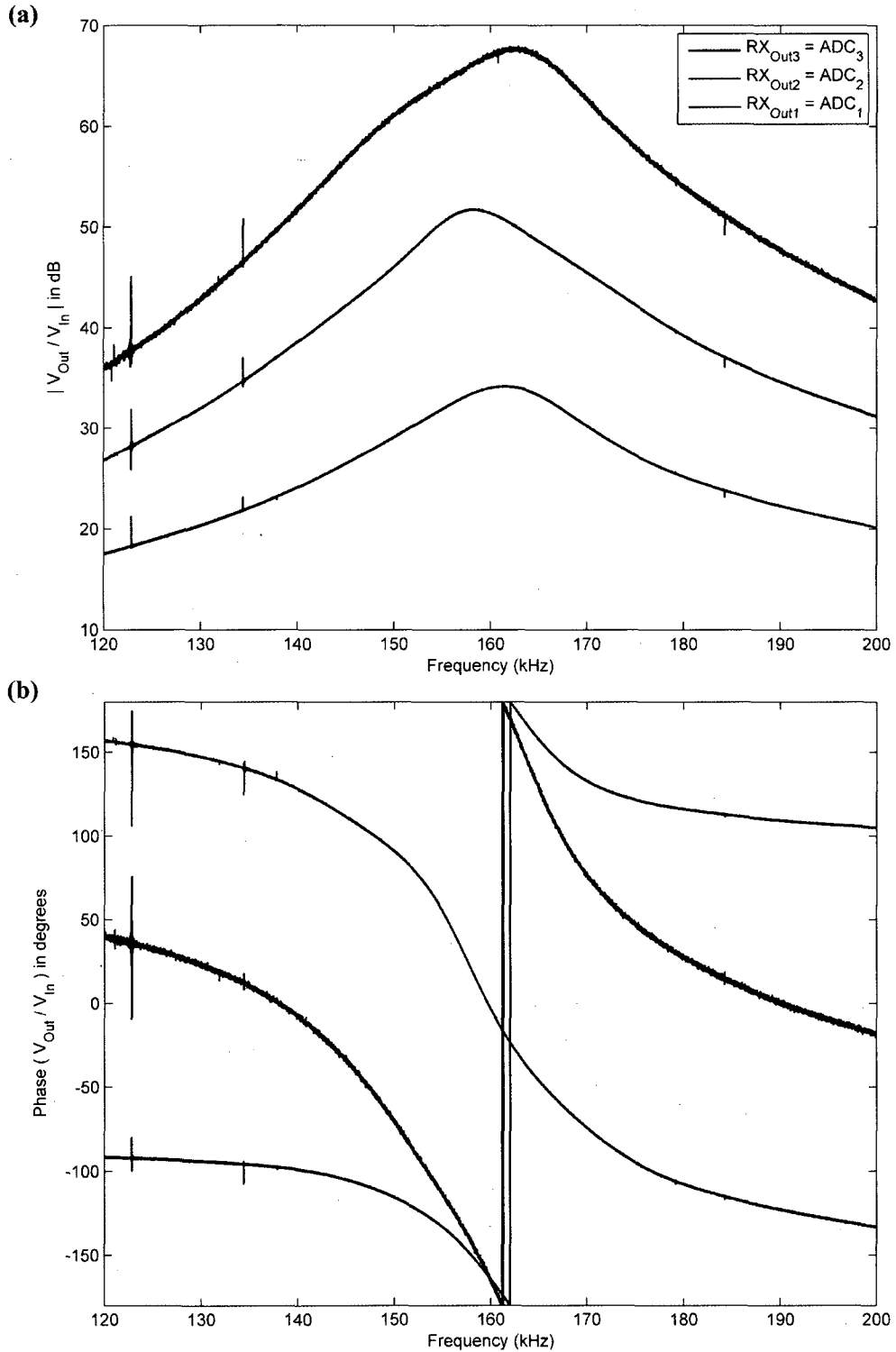


**Figure 3.10: Measured Frequency Response of the Receiver's Cascaded Sections**  
 As realized at the three outputs of the receiver's sections, the frequency response is plotted in magnitude and phase and shown in (a) and (b), respectively. Component variances affect the frequency response symmetry of cascaded sections. The transfer functions of sections 2 and 3 are therefore distorted.

The three gain stages of the LNA utilize NPN BJTs arranged in their CE configuration. When power is enabled, these transistors are biased and consume 49  $\mu\text{A}$  (at 2.8 V). Their outputs are clamped by a set of back-to-back Schottky diodes. Because each diode has a voltage drop of 0.3V and they are arranged as a series stack of 2 diodes in either direction, the output of these sections will be able to swing  $\pm 0.6$  V. The clamping of the analog signal allows for further assumptions of the number of bits needed to represent the digitized received signals for subsequent signal processing (Section 4.2.3). Components and DC biases are selected to ensure that the NPN BJTs operate in their active mode over the entirety of this 1.2 V limit. Three gain stage sections are implemented because, although one CC/CE section can achieve a voltage gain of 67 dB, either the bias-current ( $I_{\text{bias}}$ ) and/or the collector load ( $R_C$ ) would have had to be increased. To achieve the highest level of voltage gain ( $A_V^{\text{max}}$ ) in the tuned ‘LRC’ CE configuration while consuming the smallest bias-current, the negative feedback of the emitter resistance is “shorted” and the collector resistance is infinite “opened.” In this case, the voltage gain at resonance is limited by  $Q_L$  of the inductor and the maximum voltage gain is proportional to the bias-current ( $A_V^{\text{max}} \propto I_{\text{bias}}$ ) by the following equation, where  $g_m$  is the biased amplifier’s transconductance (Niknejad, 2008):

$$A_V^{\text{max}} \approx -g_m Q_L \omega_0 L$$

Compared to N identical cascaded sections in this configuration, bias-current additively increases while their effective gains increase geometrically:  $N I_{\text{bias}} \propto (A_V)^N$ . As a consequence, three gain-stage sections are utilized in the design to decrease bias-current consumption at the expense of more components (and more noise). As illustrated within Figure 3.10, the gain of the receiver increases according to which output tap is being sampled by the ADC. This provides a crude form<sup>13</sup> of discrete Automatic Gain Control (AGC). The last stage can be used for receiving weak signals and provides the most gain and is also the most frequency selective. Even though this

---

<sup>13</sup> Because the receiver’s bandwidth is also changed

form of AGC will not maintain a constant receive band, reducing the noise bandwidth for high gain is a sensible solution and a detection performance trade-off. Improvements of the dynamic performance of the micro-transponder might benefit from the ability to switch between the different ‘taps’ of the LNA / BPF, but this feature is not currently implemented within the design.

The CE gain stages are isolated from one another by buffers. Buffers constructed from PNP BJTs and arranged in their CC configuration drive the signal into the next gain stage section and, if enabled by the MCU, additionally drive the signal into the ADC<sup>14</sup>. They have an input resistance of 78 k $\Omega$  and are biased to consume 101  $\mu$ A (at 2.8 V). They can provide a  $\pm 1.2$  V signal-swing and have an output impedance of less than 240  $\Omega$ .

To understand the context of the LNA / BPF in the transponder design, the transducer’s receive-response can be included in the analysis by way of superposition. Figure 3.11 shows the measured transient response of the analog receiver with and without signal incident on the transducer and illustrates its functionality upon startup. The transistor’s bias points are overshoot on start-up and reach their steady-state value within  $\sim 0.7$  ms. The MCU takes this delay into account when it enables power to the receiver.

---

<sup>14</sup> With the exception of the first buffer, which provides high input impedance into the amplifier.

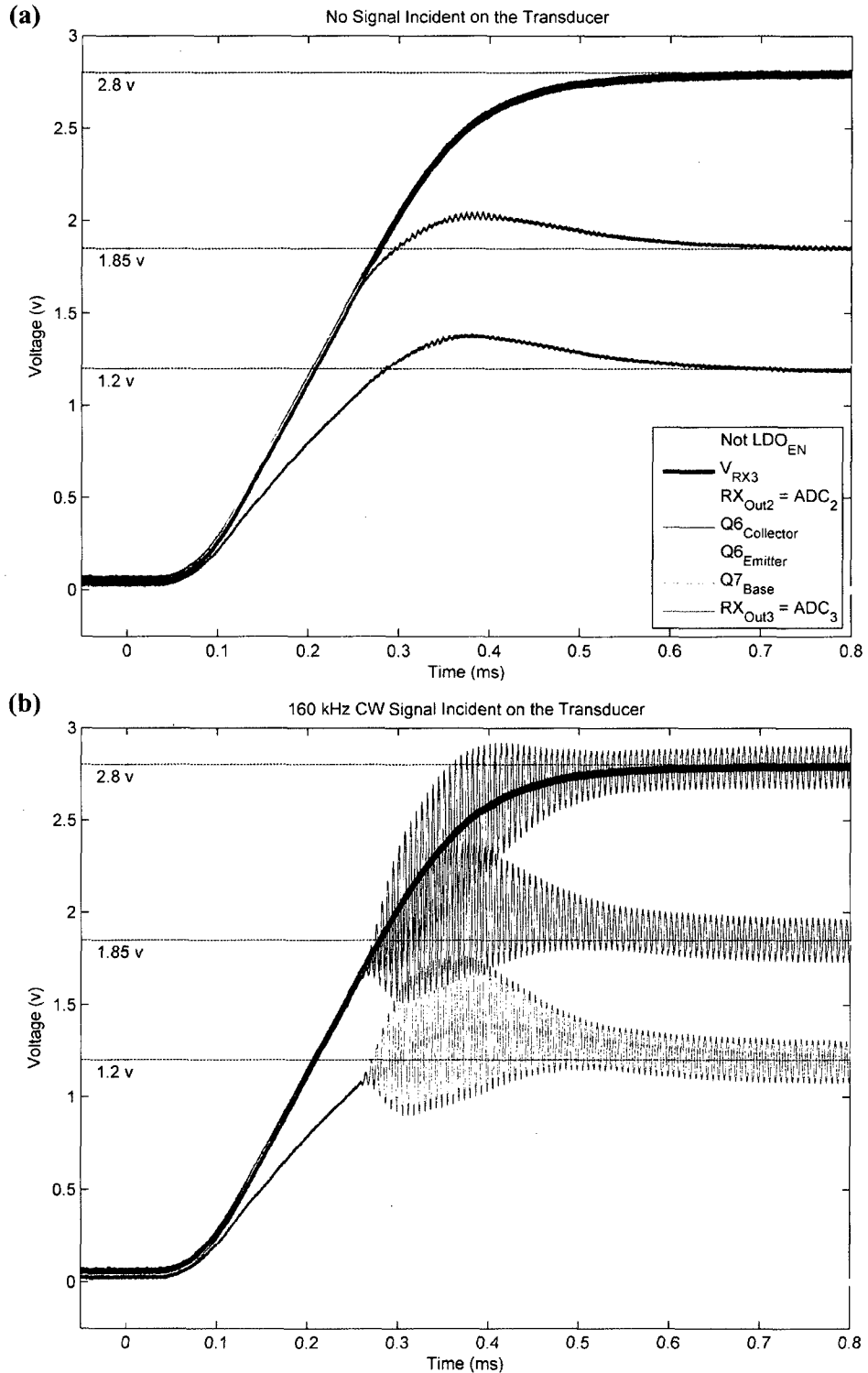


**Figure 3.11: Transient Response of the Final Analog LNA / BPF Section**  
 As measured by an oscilloscope, the response when no signal is incident on the transducer is described in (a) and illustrates the DC biases of the transistors used in this design. The response when a 160 kHz CW signal is incident on the transducer is described in (b) and illustrates the steady-state response time of this design.

### **3.5.3 Interfacing the Receiver with the ADC Input of the Microcontroller**

The 12-bit Analog to Digital Converter (ADC12) within the TI MSP430 MCU uses a switched capacitor architecture that performs successive-approximation based on the charge redistribution of an input source voltage ( $V_S$ ). The equivalent resistance of the MCU's internal Multiplexer (MUX) in series with the capacitance of the Successive Approximation Register (SAR) requires a period of time for charging ( $T_{Sample}$ ). The data sheet of the MSP430 lists the values for MUX-on resistance ( $R_{MUX}$ ) and SAR capacitance ( $C_{SAR}$ ) as 2 k $\Omega$  and 40 pF, respectively and explains that the voltage across this capacitance must be charged to "within  $\frac{1}{2}$  LSB of the source voltage  $V_S$  for an accurate 12-bit conversion" (Texas Instruments, SLAU144E, 2008). Because the source voltage sampled by the ADC is driven by the emitter-follower buffer of the LNA/BPF and they have an output resistance ( $R_{RX}^{OUT}$ ) of 240  $\Omega$ , the steady-state response time required by the SAR is mainly constrained by its internal MUX-on resistance. The following formula is given by the data sheet and is used to calculate the sample timing requirements for 12-bit accurate analog to digital conversions:

$$T_{sample} > (R_{RX}^{OUT} + R_{MUX}) \ln(2^{b+1}) C_{SAR} + 800 \text{ ns} \approx 1.6 \mu\text{s}$$

When quantizing analog signals, the resolution of a 12-bit ADC is a function of the full-scale voltage ( $V_{FS}$ ) range that it is converting. The ADC of the MCU is configured to reference its supply voltage ( $V_{CC}$ ) and Ground (GND) when converting analog signals. The resolution of the 12-bit ADC ( $\Delta V_{ADC}$ ) is calculated using the following formula:

$$\Delta V_{ADC} = \frac{V_{FS}}{2^b - 1} = \frac{V_{CC} - GND}{2^{12} - 1} = \frac{3}{4095} \approx 733 \mu\text{V}$$

Figure 3.12 shows the transient charge-time of the SAR and illustrates the impulsive effects of sampling the receive waveform with the MSP430's ADC12.



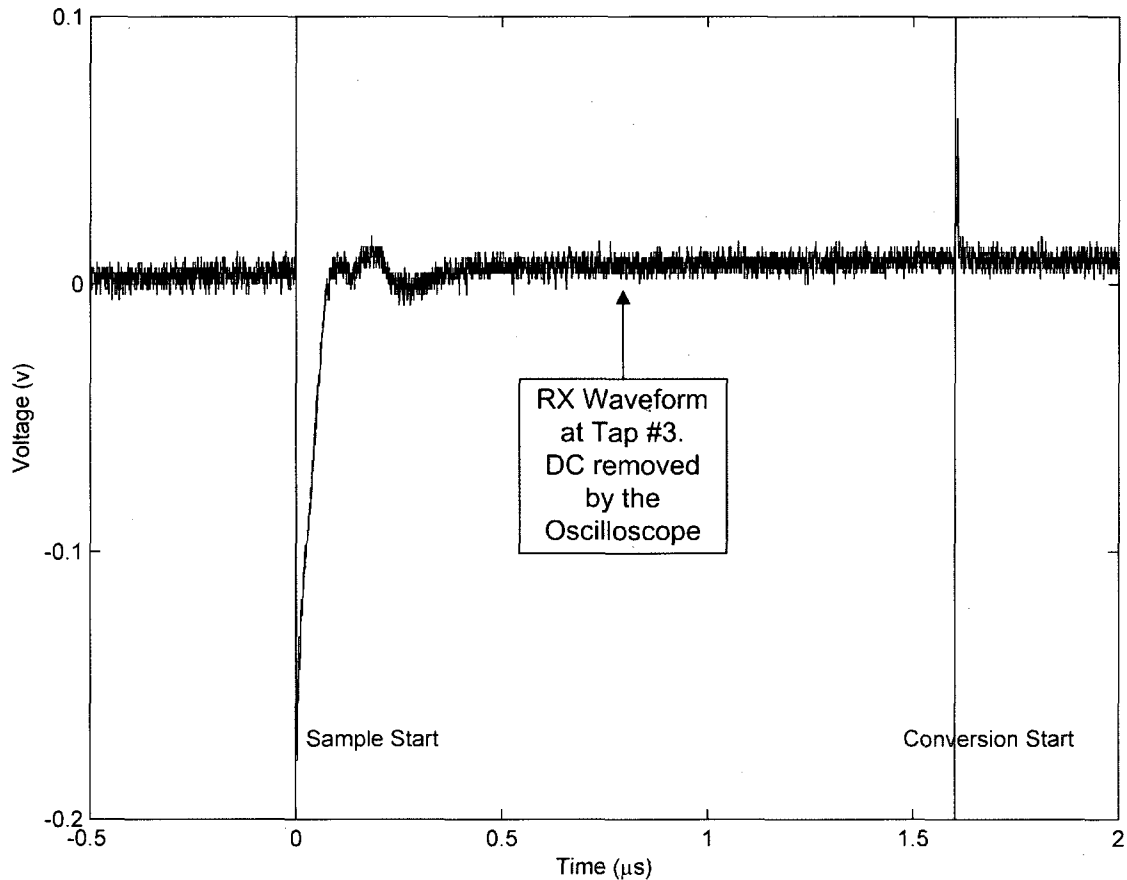


**Figure 3.12: Observed Effects of the SAR ADC Sampling the Received Waveform**

The effects of waveform sampling using the MSP430's ADC12 are shown. When sampling is initiated, the input of the SAR ADC is opened and its capacitor bank is charged. After 1.625  $\mu\text{s}$ , this bank of capacitors is charged to within 367  $\mu\text{V}$  of the received waveform's voltage value and conversion begins.

### **3.6 The Transmitter**

Non-linear switching amplifiers are easily controlled by, and integrated with, microcontrollers and allow for power efficient transmission of signals. A Linear Technology LT3572 is used because it integrates both the functions of voltage conversion and digital switching in a single IC. This IC can deliver up to 1.5 W at switching speeds acceptable for transmitting coded signals at 160 kHz and consumes a quiescent-current of 7.4  $\mu\text{A}$  when shut down (Linear Technology, LT0408, 2007). Figure 3.13 shows the circuit topology of the discrete components that support this IC and illustrates its context within the micro-transponder's design.

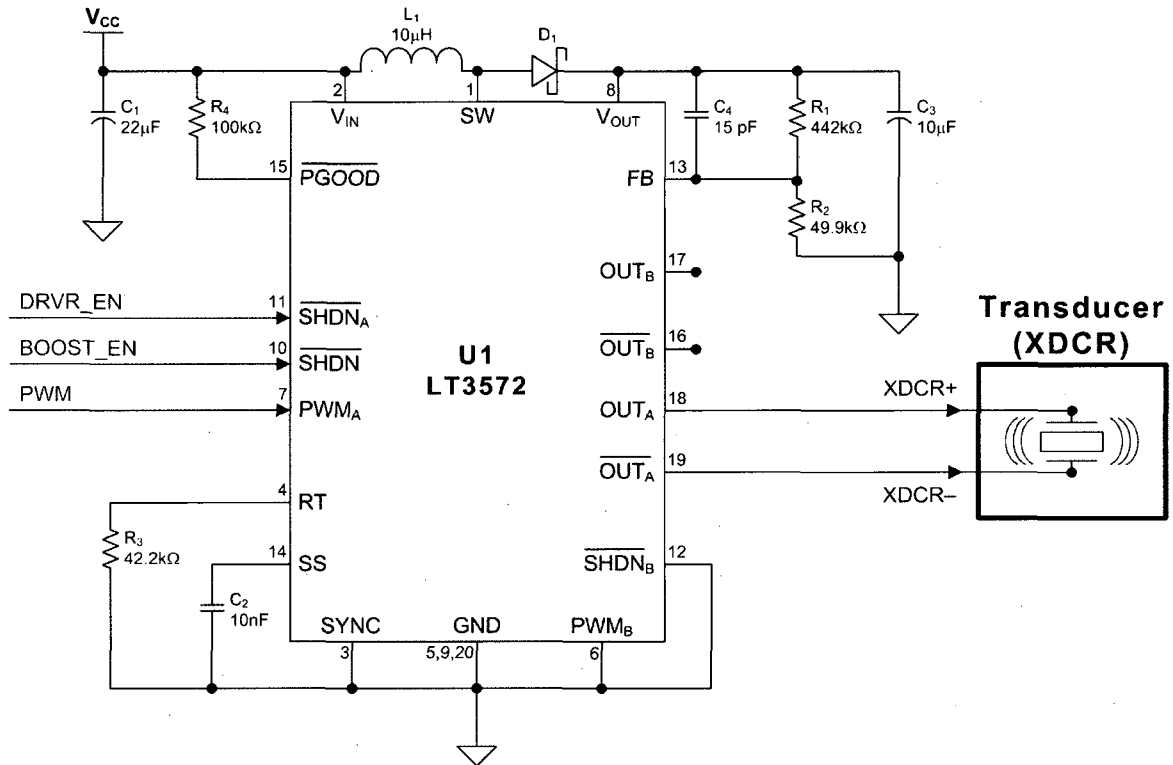


**Figure 3.13: Circuit Topology of the Transmit Amplifier**

The LT3572 IC is used for power-amplification of low-level digital-switching logic sent by the MCU. This IC contains both a boost converter and differential full-bridge switching amplifier for voltage conversion and signal driving, respectively. It produces a differential output onto the leads of the transducer that is a function of the coded signal generated by the MCU.

Once the MCU determines that it is being interrogated by an APS, it stops receiving, cuts off the channel of the N-MOSFET (Section 3.4), and enables the boost converter of the LT3572. “The soft-start feature [of the converter] limits the inrush current drawn from the supply upon start-up.” (Linear Technology, LT0408, 2007). The boost converter systematically steps-up the battery supply from 3 V to 12 V within 1.2 ms by way of its internal switching regulator (Figure 3.14). The PGOOD pin on the IC is toggled low when steady-state is reached. Afterward, the coded signal generated by the MCU can be differentially driven onto the leads of the transducer. The coded signal, generated by the digital logic of the MCU, is driven at the boost level onto the positive transducer lead. Similarly, this logic is inverted and driven at the boost level on the negative transducer lead. The operation of the Boost Converter and Full-Bridge Driver in relation

to the coded signal that is generated by the MCU is shown in Figures 3.14 and 3.15, respectively.

When driven by the LT3572 in this configuration, the direction of the transducer current is a function of the digital logic of the MCU's coded signal. The full-bridge drivers are internally controlled by the IC and at times not correlated with switching, the transducer's leads are oppositely driven with either the boost voltage or ground. In this differential arrangement, the peak-to-peak signal swing is twice the driven voltage. The full-bridge driver outputs a square wave onto the leads of the transducer, thus the average power delivered to the transducer is proportional to the squared peak voltage. Because the transducer is band-limited and exhibits a high Q, the fundamental frequency (160 kHz) will be predominantly transduced by the piezoelectric ceramic into a sinusoidal pressure field. The rms voltage ( $V_{RMS}$ ) delivered to the transducer is shown in Figure 3.15 and measured as 10.2 V. The power delivered ( $P_d$ ) to the transducer ( $Z_{XDRC}$ ) is calculated as  $P_d = V_{RMS}^2 / |Z_{XDRC}| \sim 0.7$  W. As consequence, the transducer generates the 167 dB re 1  $\mu$ Pa at 1 m of acoustic pressure needed for signal transmission (Section 3.2.3). When not loaded by the transducer, the IC's output nodes swing from ground to  $V_{Boost}$  (12 V). This suggests that, when the transducer is driven, power is lost by the internal resistance of the IC's output stage. When the transducer is driven with  $V_{RMS} = 10.2$  V, the efficiency ( $\eta$ ) of the full-bridge driver is calculated as  $\eta = 10.2 / 12 = 85\%$ .

When transmitting a coded reply onto the leads of the transducer, the average power-demand of the aggregate functions of the LT3572 is calculated as  $\sim 1220$  mW. The following analysis estimates the average power-demand of this IC. When driving the transducer with the boost voltage, the power-demand of the full-bridge driver is calculated as  $P_{DRVR} = (V_{RMS} V_{Boost}) / |Z_{XDRC}| \sim 827$  mW. The power-demand of the boost converter can be simplified by estimating the switching losses within the 10  $\mu$ H inductor. The switching regulator of the boost converter is configured to operate at 800 kHz. When regulating, the switch node is toggled between the boost voltage ( $V_{Boost}$ ) and ground (SW node in Figure 3.13). The SW node is controlled by the IC.

When idle, the SW pin sits at the supply voltage ( $V_{CC} = 3 \text{ V}$ ) and no current runs through the inductor. When transmitting, this node is empirically shown to have a 23% 12 V duty cycle and a 77% GND duty cycle. Because a  $10 \mu\text{H}$  inductor sits between the supply and this SW node, the average voltage dropped across this inductor is estimated by its duty cycle to be 4.38 V. At a switching frequency of 800 kHz, the magnitude of average current that runs through the  $10 \mu\text{H}$  inductor is calculated as  $\sim 87.6 \text{ mA}$ . The average power-demand of the boost converter's switching regulator is therefore estimated as 384 mW. Quiescent current also runs through the external resistors R1 and R2 (used to program the output boost voltage) and the other functions associated with the LT3572. This current consumption is found by inspection of its data sheet. These functions add another  $\sim 10.6 \text{ mW}$  to the aggregate power-demand of the IC when transmitting.

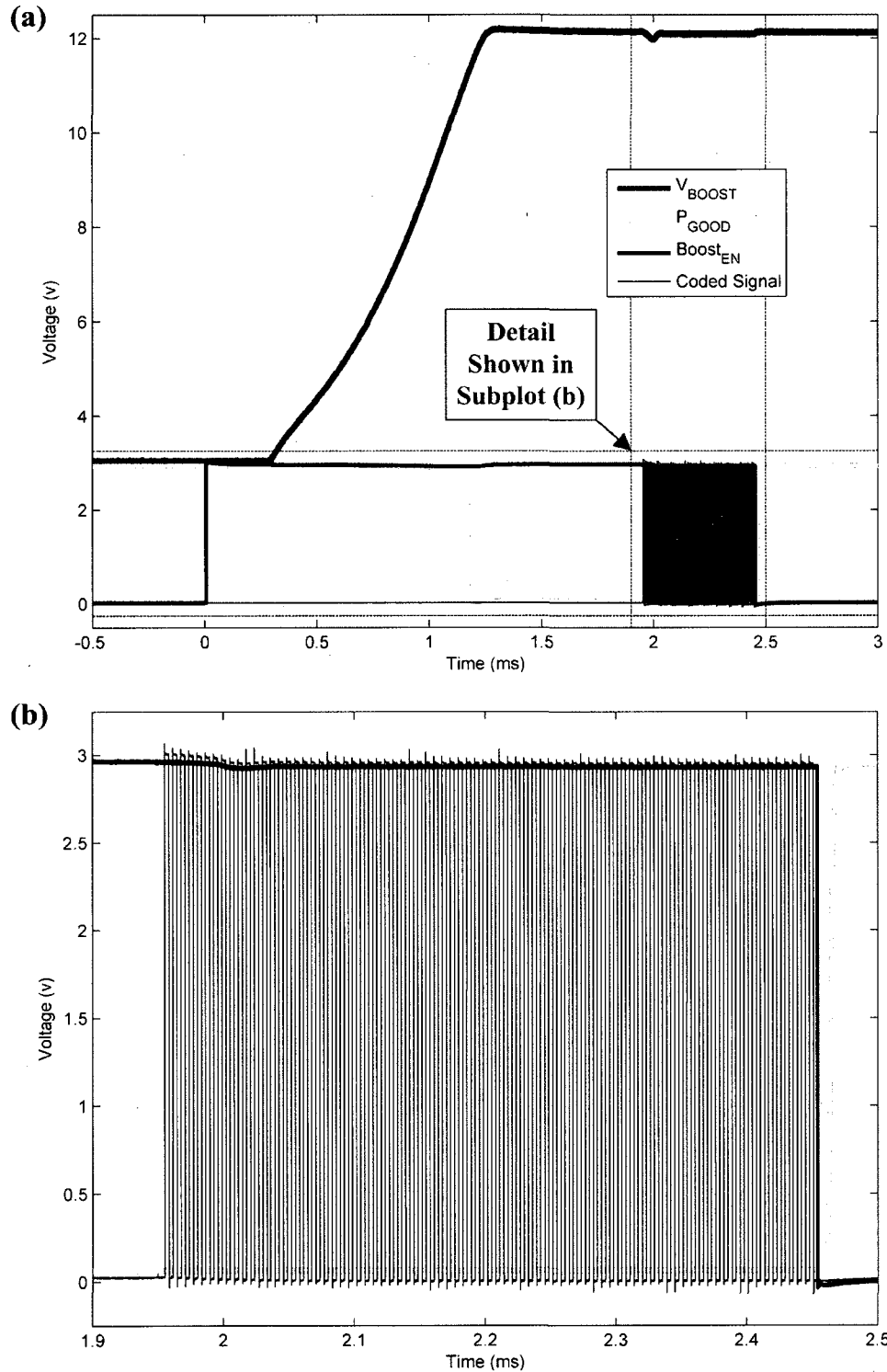


**Figure 3.14: Operation of the Boost Converter when Transmitting a Coded Signal**

The function of the IC's boost converter is shown. (a) The boost converter, enabled by the MCU, increases the supply voltage from 3 V to 12 V within 1.2 ms. The IC drives its PGOOD pin low when steady-state is reached. Afterward, the coded signal generated by the MCU (b) can be driven.

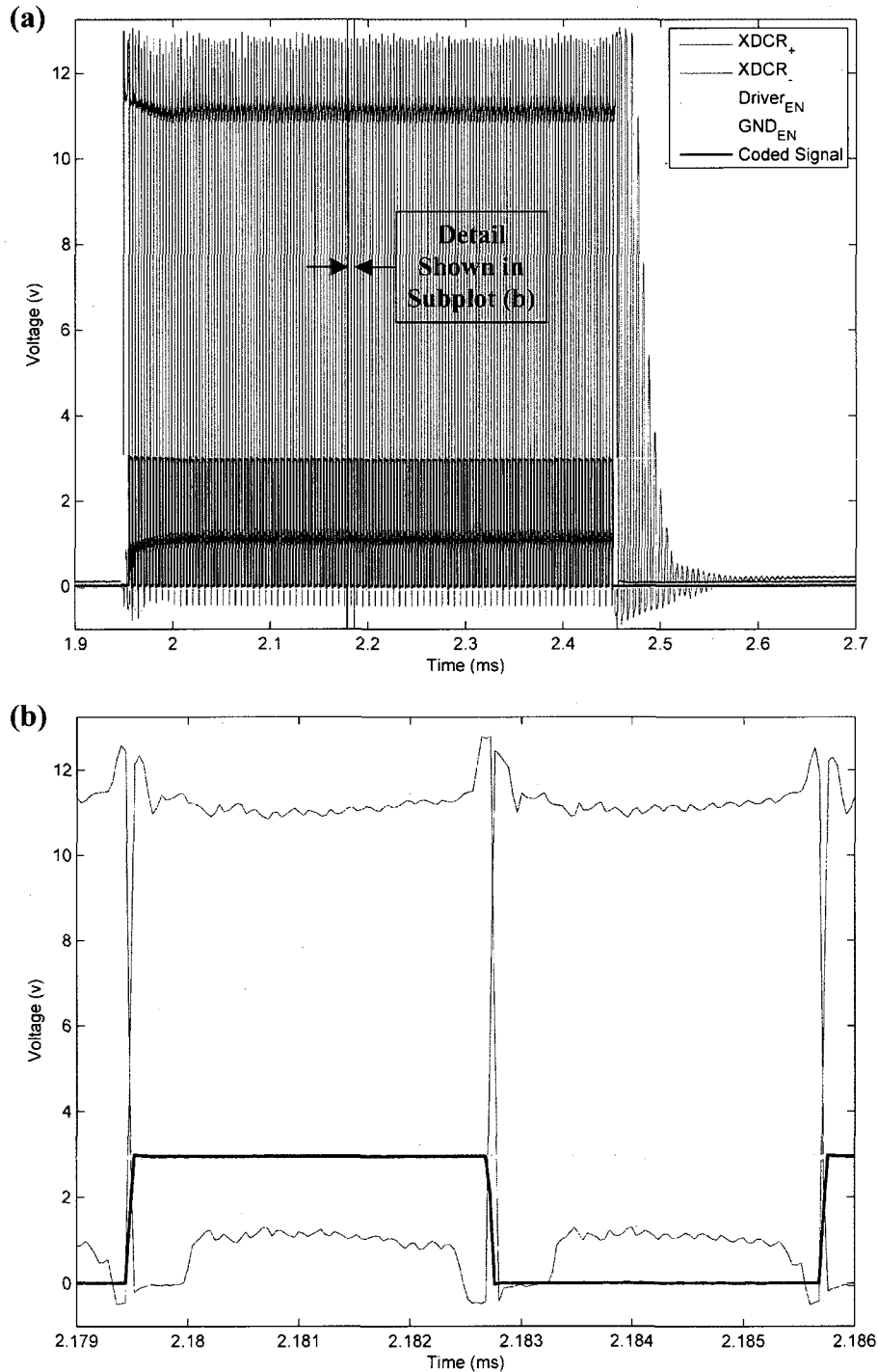


**Figure 3.15: Operation of the Full-Bridge Driver when Transmitting a Coded Signal**  
 The function of the IC's full-bridge switching amplifier is shown. This amplifier, when enabled by the MCU, drives the transducer differentially. The coded signal, generated by the MCU, is output at the boost level on the positive transducer lead. Similarly, the coded signal is inverted and output at the boost level on the negative transducer lead. When driven the transducer's loading effects are observed. As a result the average voltage delivered across the transducer is reduced from 12 V<sub>RMS</sub> to 10.2 V<sub>RMS</sub>.

### **3.7 The Battery Supply**

A 3 V Panasonic CR2354 (height = 5.4 mm, diameter = 23 mm, weight = 5.9 g) lithium primary watch battery is used to supply 560 mAh of electrical energy to the micro-transponder. “The high energy density of the lithium batteries and their high voltage of 3 V make them ideally suited for use in all kinds of products where the trend is to achieve increasing miniaturization. A single lithium battery can replace two, three or more conventional batteries” (Panasonic, 2000). The energy density of the CR2354 is calculated to be 750 kWh/m<sup>3</sup>. Although lithium primary batteries have a good energy density, they are limited in the amount of power they can provide at any given time (low power density). Capacitors, on the other hand, have much greater power densities.

Because pulsed-current demands cause the battery voltage to drop when transmitting, a 75 mF supercapacitor is added to the circuit topology of the power supply to provide enough energy for an acoustic transmission. The supercapacitor acts as a reservoir for the power delivered to the rest of the circuit, especially when pulsed transmissions drain ~400 mA from the power supply. Figure 3.16 displays the circuit topology of the micro-transponder’s power supply. The battery is modeled as an ideal voltage source in series with an internal resistance. Although it is explained in the Lithium Battery Handbook that the internal resistance will increase as the [battery] reaches the end of its lifespan, the CR2354’s internal resistance is unknown and not specified in its data sheet.

Resistors are recommended by the manufacturer to evenly balance the two cells within the supercapacitor ( $R_{31}$  and  $R_{32}$  in Figure 3.16). The manufacturer recommends that these resistors be chosen such that their leakage current is ten times that of the supercapacitor itself (~1  $\mu$ A) and therefore they were picked to be 150 k $\Omega$  each. Since the Equivalent Series Resistance (ESR) of the supercapacitor ( $R_{CAP} = 150$  m $\Omega$ ) is much smaller than the balancing resistors, essentially all of the current will be drawn into the capacitor from the battery, upon startup.

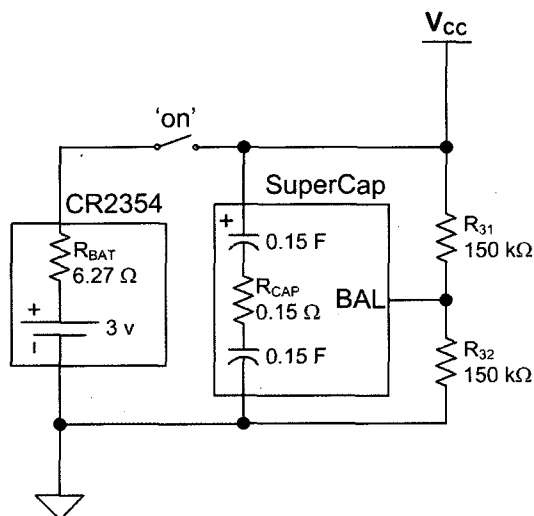


**Figure 3.16: Power Supply Topology**

The power supply of the micro-transponder is comprised of a single Lithium battery (CR2354) connected directly to a 75 mF supercapacitor. Balance resistors,  $R_{31}$  and  $R_{32}$ , are used to regulate the voltage drop across the two cells within the supercapacitor.

When the two headers connecting the battery to the (initially uncharged) supercapacitor are electrically shorted, the current drawn into the capacitor will be a function of the battery voltage ( $V_{BAT} = 3\text{ V}$ ) and the ESR of the battery and the capacitor ( $R_{BAT}$  and  $R_{CAP}$ , respectively). This maximum current draw ( $I^{max}$ ) is calculated from the following equation:

$$I^{max} = V_{BAT} / (R_{BAT} + R_{CAP})$$

Since the lithium battery will not be able to supply this current at the rated voltage, the battery voltage will drop. As more current flows into the capacitor, the difference between the ideal steady-state battery voltage and the instantaneous supply voltage will decrease exponentially. The supercapacitor will, eventually, charge up to the steady-state battery voltage. The RC time constant is empirically found by measuring the charging time associated with connecting the battery directly to an initially “empty” supercapacitor:  $\tau = C (R_{BAT} + R_{CAP})$ .  $\tau$  is measured in Figure 3.17 as 450 ms. From the rated ESR of the supercapacitor and the measurements of the charge-time constant, the internal resistance of the battery is calculated as 6.27  $\Omega$ . The maximum instantaneous current drawn from the battery into the supercapacitor is therefore calculated as 467



mA.

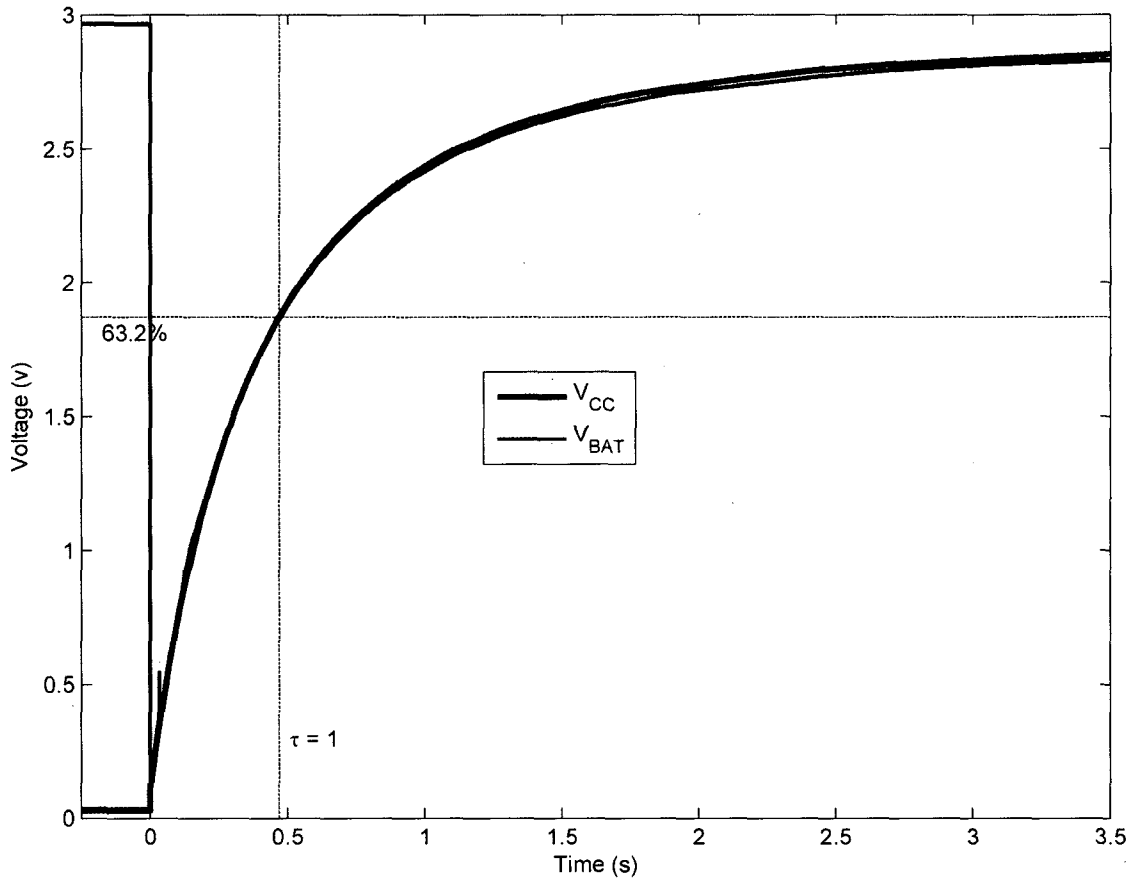


**Figure 3.17: Power Supply Transient Response on Startup**

The battery and capacitor voltages are shown in red and blue, respectively. A 450 ms charging time is observed when the battery is shorted across the leads of an initially uncharged supercapacitor.

The amount of energy supplied by the supercapacitor to the transmit circuitry is proportional to the size of the supercapacitor. Likewise, the length of time that this capacitor can sustain an acoustic transmission is inversely proportional to the transmit power-demand (calculated as  $P_{TX} \sim 1.2$  W in Section 3.6). The voltage across the leads of the supercapacitor will initially drop from the instantaneous current-demand (calculated as  $I_0 = P_{TX} / V_{CC} \sim 400$  mA). This initial voltage drop,  $V_0$ , is calculated as the product of instantaneous current-demand and the ESR of the supercapacitor ( $V_0 = I_0 R_{CAP} = 60$  mV). The supercapacitor's voltage will continue to drop as a function of the power-demand from the micro-transponder's transmit circuitry. Because

the LT3572 specifies a minimum operating voltage of 2.5 V and because energy stored in a capacitor is proportional the square of its voltage drop ( $\Delta V$ ), the supercapacitor constrains the duration ( $T_{TX}$ ) of the signal transmissions by the following equation:

$$T_{TX} \leq \frac{C (\Delta V)^2}{2 P_{TX}} = \frac{C (V_{BAT} - V_0 - V_{LT3572\_min})^2}{2 P_{TX}} \approx 6 \text{ ms}$$

Therefore, the micro-transponder can not sustain coded signal transmissions in excess of 6 ms.

### **3.8 The Printed Circuit Board**

The micro-transponder's PCB was designed using PCB Artist, a CAD design tool from Advanced Circuits. "The PCB board layout and component placement" of switching regulators requires "careful attention" (Linear Technology, LT0408, 2007). A PCB meeting the specifications of the LT3572 demo-board (LT 1197A), was laid-out for the circuits illustrated throughout the text. The PCB is comprised four layers. The middle two layers are the ground and power planes, respectively and the top and bottom layers are etched to include the signal traces of the design. Appendix E illustrates the details of this design.

## CHAPTER IV

### DIGITAL DESIGN – EMBEDDED FIRMWARE

#### **4.1 Overview of the Digital Design and Signal Processing Methodology**

Interrupt-based code flow is integral to the low-power performance of the microcontroller. This technique uses interrupts, generated by peripheral modules within the MCU (or input signals present on port pins), to alert the CPU of an event. An Interrupt Flag (IFG), if activated, will be addressed by the CPU upon the next available clock cycle. Interrupt Service Routines (ISRs) within the MSP430 are code-based directives that change the course of CPU instructions and automatically clear the acknowledged IFG upon completion of the routine. The ISR for a particular IFG may be used to change variables, store results, toggle pins, or any other action available within the instruction set. An important feature of the MSP430 is that an ISR can change the CPU mode of operation after its execution is complete by modifying the status register (SR) which was pushed onto the stack before it began; that is, keep the CPU awake (and active) or put the CPU into one of its five Low-Power Modes (LMP0→LMP4). The TI MSP430 Application Report on Software Coding Techniques (Quiring, 2006) recommends a “code architecture [that] is interrupt driven, because doing so provides the most opportunities to power down the device. The device sleeps until an interrupt is received, thereby maximizing power efficiency.”

An analysis of the current consumed by the MSP430 in its various operating modes reaffirms the previous statement. The following table highlights the current consumption of the MCU for the two modes implemented in this digital design: Active Mode (AM) operation and LPM0 operation. The difference between these two modes is that the CPU clock is enabled in AM (via MCLK) and instructions are being fetched and executed. The Sub-Main Clock

(SMCLK) remains active in both modes and, therefore, allows for precise (high-frequency) timing of hardware peripherals whether the CPU is ‘on’ or ‘off.’ Current consumption at Digitally Controlled Oscillator (DCO) frequencies of 8 and 12 MHz are particularly important because the designed transponder uses the DCO to source MCLK and SMCLK at these frequencies for receive and transmit timing, respectively. Even though the data sheet for the MSP430 (Texas Instruments, SLAS547B, 2008) did not explicitly list the current consumption of this device in LPM0 at 8 and 12 MHz, the current consumption was inferred based on a linear fit of the data that was available (an approximation made because  $I_{AM}$  is shown to be linear over this region).

**Table 4.1: Current Consumption of the MCU at Applicable Clock Frequencies**

The power-demand of the MSP430 is a function of the clock frequency, its mode of operation, and the supply voltage ( $V_{CC}$ ). The data highlighted in ‘red’ is the inferred current consumption of the MCU in LPM0 at 8 and 12 MHz.

Mode of Operation	DCO Frequency	Current Consumption	
		Typical	Max
AM	8 MHz	3 mA	-
AM	12 MHz	4.25 mA	-
LPM0	1 MHz	75 $\mu$ A	90 $\mu$ A
LPM0	100 kHz	36 $\mu$ A	46 $\mu$ A
LPM0	8 MHz	378.3 $\mu$ A	432.2 $\mu$ A
LPM0	12 MHz	510.5 $\mu$ A	627.8 $\mu$ A

From this data it is apparent that a worst case current savings of 85.6% will be achieved when putting the device into its LPM0 state.

In order to service an IFG from a device residing in a low-power mode, the Master Clock (MCLK) needs to be re-established before the CPU can acknowledge the interrupt. Therefore, while power is saved by putting the device to sleep, time is lost while the MCU restarts the CPU (wake-up latency).

[Fortunately,] The design of the MSP430 was driven by the need to provide full real-time capability while still exhibiting extremely low power consumption. Average power consumption is reduced to the minimum by running the CPU and certain other functions of the MSP430 only when it is necessary...power is conserved by keeping only selected low-power peripheral functions active. But to have a true real-time capability, the device must be able to shift from a low-power mode with the CPU off to a fully active mode

with the CPU and all other device functions operating nominally in a very short time...Only two additional MCLK cycles ( $2 \mu\text{s}$  at  $F_C = 1 \text{ MHz}$ ) are necessary to get the device from LMP3 to the first instruction of the interrupt handler (Bierl, 2000).

Since the DCO is still active in LPM0 and sourcing SMCLK (as opposed to the cited LPM3 case), it is assumed that the wake-up latency would be at worst one clock cycle ( $125 \text{ ns}$  at  $F_{\text{DCO}} = 8 \text{ MHz}$ ). The MCU is then able to service the IFG of the peripheral/source that triggered it. In addition to the wake-up latency needed to re-establish the CPU, a minimum of 11 MCLK cycles are required to acknowledge the IFG within an ISR and return control to the main program (“wake-up and service latency”). With the current consumption and “wake-up service latency” trade-off established as such, an interrupt based code architecture that follows TI’s Software Coding Techniques is implemented in the embedded firmware design of the micro-transponder.

The microcontroller has a variety of dedicated on-board hardware that can perform specific and often repetitive tasks (called peripherals). The understanding of two such peripherals is critical in describing the digital design of the transponder: the general purpose timer (Timer A) and the 12-bit Analog-to-Digital Converter (ADC12). Timer A is used for precise timing of operations within the design. Specifically, when receiving, Timer A is used to control the sampling frequency ( $F_s$ ). The sampling signal generated by Timer A triggers the Sample and Hold (S/H) operation of the Successive Approximation Register (SAR) of the ADC12. The ADC12 digitizes the received waveform and automatically stores the 12-bit result in memory via a Direct Memory-Access (DMA) Controller which requires no CPU intervention. When transmitting, Timer A is configured to generate a 50% duty cycle Pulse Width Modulated (PWM) signal at a prescribed Carrier Frequency ( $F_C$ ). The transmit signal generated by Timer A is output on the prescribed port pin of the MSP430 and finally amplified by the LT3572 IC. To configure a peripheral within the MSP430, a value is written to a dedicated memory location (called a peripheral register or a special function register).

The overall code architecture of the micro-transponder can be summarized by three distinct features: configuring peripherals, promptly servicing interrupts, and executing code that

is based on these ISR events. The flow chart of the overall embedded digital design is shown in the Figure 4.1. The overall digital design is simply an extension of the canonical function of the transponder (Figure 2.1) and uses the features of the MCU for accurate and efficient demodulation and detection of signals, thereby conserving power whenever possible.

As highlighted by the code flow in Figure 4.1, the micro-transponder demodulates and detects signals in real-time until it determines that the prescribed interrogation signal has been received. The algorithm then shuts down the receiver, turns on the transmitter, and transmits a coded message. After each transmission, the MCU shuts down the CPU and waits for 32 ms, thereby, “blinking” the receiver from reverberation. That is, the micro-transponder waits for the transients from reflections of its transmitted signal to attenuate to an acceptable level before receiving again. From empirical data collected within an acoustic test tank, 32 ms was determined to be enough time for TX reverb to die off. Currently, no signal processing equalization is implemented within the design and, therefore, “blinking” is used. Real-time signal processing is shown within the receiver’s digital design. The critical path for this design is highlighted in red. All operations within this path need to be completed before another four samples are collected, or else, signal processing of sequential sample sets will not be possible. Subsequent sections of this chapter will detail the specific signal processing techniques used to demodulate and detect receive signals within the water column.

This code was designed, downloaded, and tested using IAR’s Embedded Workbench Integrated Development Environment (IDE). The routines developed in “C” and Assembly language are compiled and linked into a single executable-machine-code using this software. The code is then downloaded to the “target” device (the MSP430 IC soldered directly to the PCB) using the MSP-FET430UIF USB Interface Module. This hardware connects the USB port of a computer with the JTAG connections on the designed PCB. The Flash Emulation-Tool then downloads the machine code to the target and controls its execution for testing and debugging purposes.

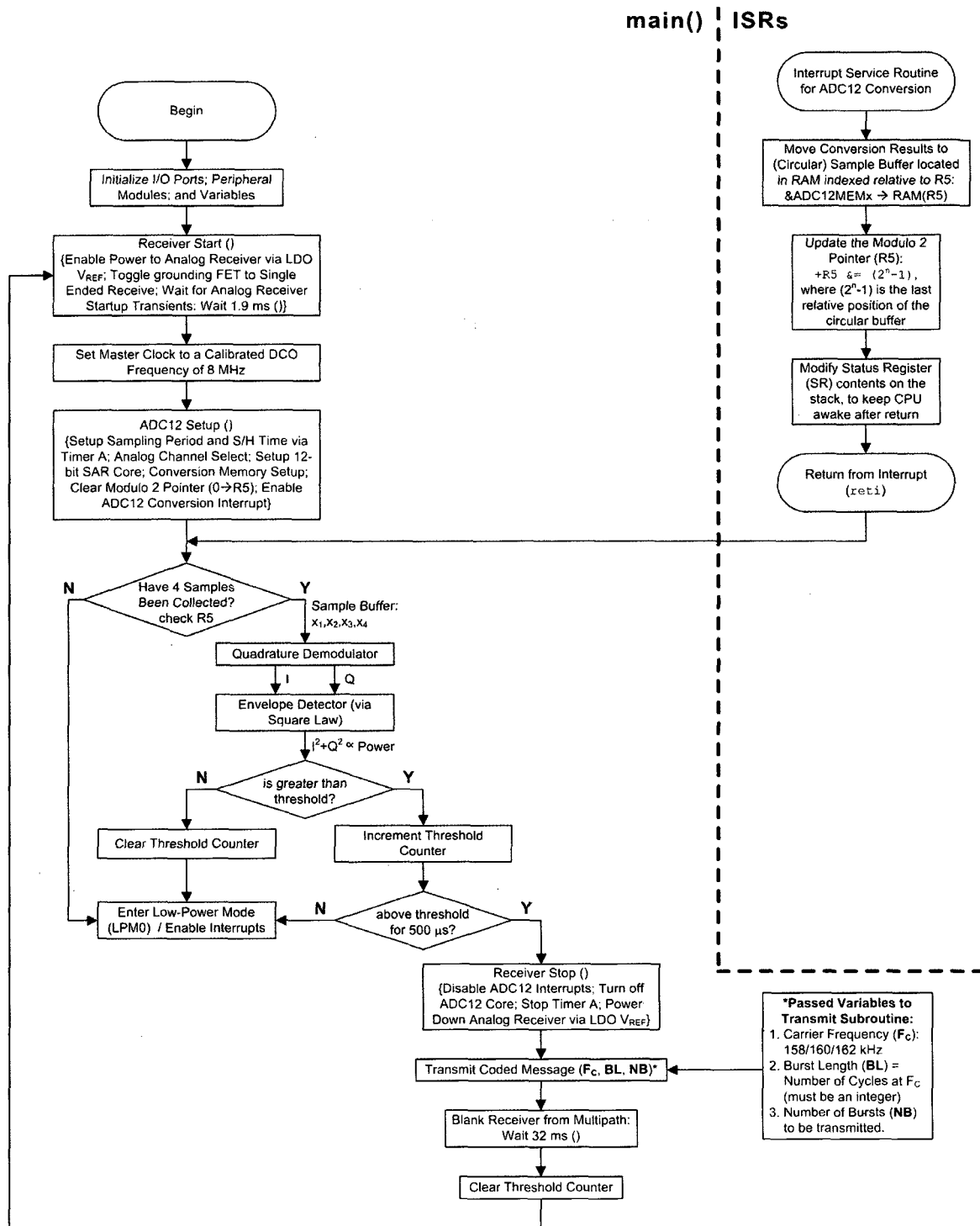


**Figure 4.1: Flow Chart of the Micro-Transponder's Digital (Embedded) Design**

The digital receive algorithm is highlighted in grey. The critical path for digital demodulation and detection is highlighted in red. For real-time signal processing, this path must be completed before 4 new samples are collected. After a received signal has been detected, the transponder transmits its coded message and waits for reverberation to pass before it starts its receive-routine again.

## **4.2 Receiver Digital Design**

The receiver's digital design is highlighted in Figure 4.1. The receiver's routine begins by controlling the analog sub-systems. Port pins of the MSP430 enable power to the analog receiver and toggle the Grounding FET to "single-ended" mode (Sections 3.5.1 and 3.4, respectively). The CPU is then stalled for 1.9 ms to account for the startup transients of the analog receiver (Figure 3.11). The DCO is then set to 8 MHz and configured to source MCLK and SMCLK to the CPU and peripheral modules, respectively. The execution of instructions and timing of most peripheral operations for the receiver is henceforth made with respect to this DCO frequency. The ADC12 is configured to sample analog signals at one of the three RX 'taps' at a sampling rate controlled by Timer A. The modulo-2 pointer (R5) is initialized and sampling begins. Analog signals are sampled and converted to a digitized equivalent. These results are stored in a circular sample buffer that sits within Random Access Memory (RAM). The MCU executes an algorithm that processes sequential sample sets in an infinite loop until the envelope of a sample set is greater than a preset threshold for a prescribed period of time (500  $\mu$ s). When the algorithm determines that a 'signal' is received, it disables the ADC12 and Timer A peripherals and powers down the analog receiver.

### **4.2.1 Using the MSP430 to Generate Precise Timing of Samples**

Timer A is used in conjunction with the microcontroller's ADC12 for accurate sampling of an analog receive channel. The switched capacitor architecture of the SAR-ADC requires a period of time for charging. This is called the sample mode. It was previously shown that the equivalent analog input of the SAR requires  $\sim 1.625 \mu$ s for 12-bit sampling accuracy (Section 3.5.3). When Timer A is used to trigger the SAR core of the ADC in "extended" sample mode, a digital high activates the sampling of an analog signal. The rising edge signals the start of sampling while the falling edge stops it. Figure 4.2 shows how Timer A is configured and



controls the sample mode of the ADC12.

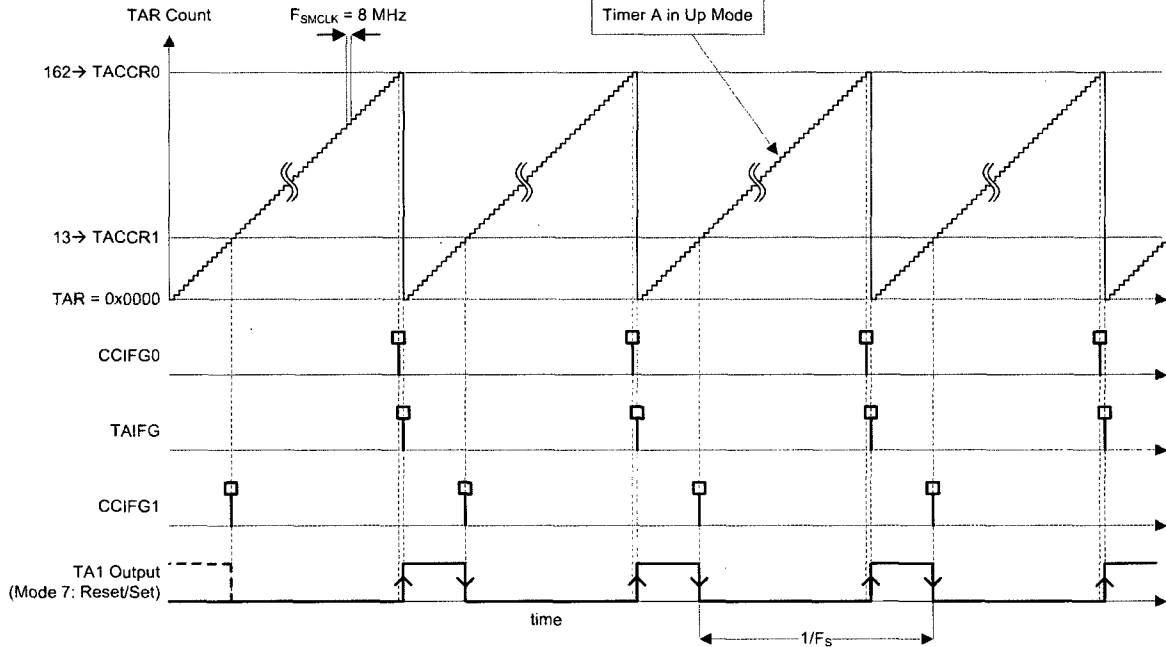


**Figure 4.2: Configuration of Timer A to Trigger the Sampling of the SAR ADC**

The output of Timer A controls the sampling frequency and the sample time of the SAR ADC. Because MCLK is set to 8 MHz and because Timer A is configured with an ‘on’ duty cycle of 8%, the sampling frequency and sample time are set to 49.08 kHz and 1.625  $\mu\text{s}$ , respectively.

Timer A is configured to count up to the value stored in the first capture/compare register (TACCR0). Since the count starts at zero, the total time between samples is one clock cycle greater than the integer stored in TACCR0. As configured, the DCO sources the timer at 8 MHz and with TACCR0 ultimately set to 162, the sampling frequency is 49.08 kHz. Although subsequent IFGs for the timer’s channels are disabled, it is useful to observe their events. The duty cycle of the timer’s output can be controlled for channels other than zero, thus channel one is used. The value stored in TACCR1 controls the IFG for channel 1 (CCIFG1). For Timer A operating in mode seven, the output of channel 1 (TA1) is reset upon CCIFG1 and set upon the timer count returning to zero (a TAIFG event). With TACCR1 set to 13, the TA1 output (sample mode) will be set high (activated) for 1.625  $\mu\text{s}$ . In this way, TACCR1 controls the period of time for sample mode operation of the SAR-ADC.

When the sample mode is complete (at the falling edge of TA1), the voltage value at that instant is held (hold mode) and the digital conversion begins. In the following, this is referred to as the redistribution mode. The data sheet for the device assures us that the operation of the 12-bit SAR-ADC will be monotonic without any missing codes and specifies its linear performance up to a maximum clock frequency of 6.3 MHz. An internal clock oscillator within the ADC12 typically runs at a clock rate of 5 MHz and therefore is used for converting the result. At this frequency, twelve clock cycles are required to convert the sampled voltage to a 12-bit value through redistribution. The DMA controller then uses another clock cycle to store the result to memory. Once stored, the conversion flag, corresponding to that memory location, is set. Figure 4.3 depicts the order of operations for the configured ADC12, beginning with the start of sampling and ending with the start of the ISR that acknowledges that the conversion result has been stored to memory.

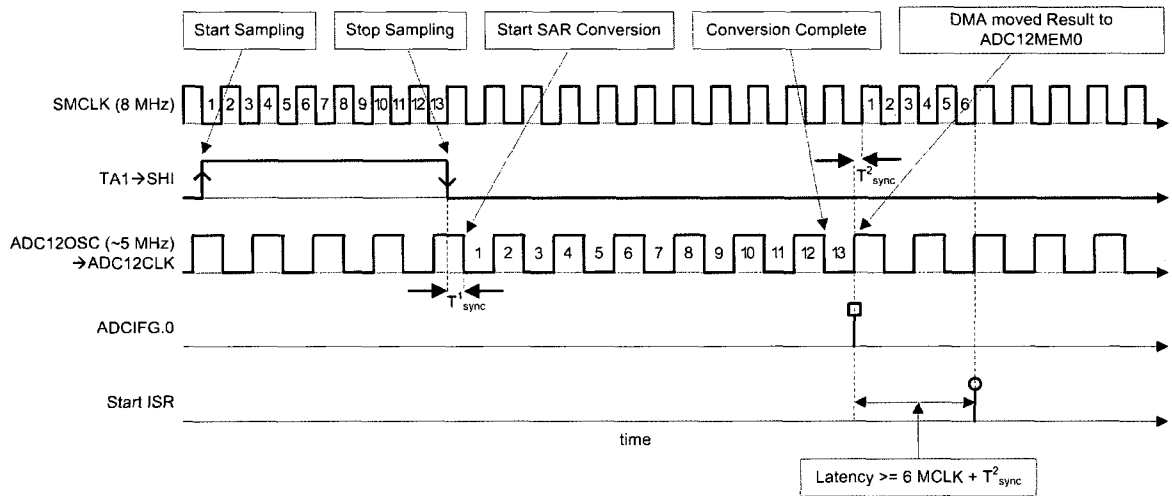


**Figure 4.3: Sample Timing including Conversion and Latency Constraints**

The operation of the SAR ADC is shown. The analog voltage value is captured on the falling edge of TA1 and converted into a 12-bit digital equivalent after 12 ADC clock cycles. Afterward, the digital value is saved in memory and triggers the ADC12 ISR event.

The SAR-ADC redistributes the sampled voltage value to a bank of binary weighted capacitors on the edge of each ADC12 clock cycle. Thus, the sampled voltage is briefly held (hold mode) until the first redistribution event occurs. This period synchronizes the ADC12 clock with the

sampling event and is referred as  $t_{\text{sync}}$  in the literature ( $T_{\text{sync}}^1$  in Figure 4.3). Using the internal ADC12 oscillator as its clock source,  $T_{\text{sync}}^1$  will be, at most, one ADC12 clock cycle or  $\sim 200$  ns. Once the sampled voltage value is redistributed over all SAR capacitors and the binary result is stored to one of the 16 predefined memory locations (ADC12MEM0 in this case), the IFG is set and upon the next CPU clock cycle and the interrupt is addressed. The time between an ADC12IFG event and the next CPU clock cycle is shown as  $T_{\text{sync}}^2$  in Figure 4.3. Because the DCO sources both the SMCLK and the MCLK of the CPU,  $T_{\text{sync}}^2$  is implied in Figure 4.3 and will be, at most, one DCO clock cycle or 125 ns. If the CPU were powered down in LMP0 prior to the ADC12IFG.x event, a sequence of CPU operations lasting 6 clock cycles is necessary before the start of the ISR. If the CPU is not powered down prior to the ADC12IFG.x event, the instruction currently being executed by the CPU must first be completed before the 6-cycle sequence can push the ISR address into the Program Counter (PC) and thus beginning the start of the ISR. The ISR latency is therefore calculated to be between 750 ns (LMP0 case) and 1.5  $\mu$ s (for at worst a 6-cycle instruction) with an unknown synchronous event ( $T_{\text{sync}}^2$ ) that might cause an additional 125 ns of latency. The entire conversion latency of the ADC12 is therefore calculated to be between 3.35  $\mu$ s and 4.1  $\mu$ s, with unknown synchronizing events that may cause an additional 325 ns of latency. Here, the latency is the time differential between capturing an analog sample and the start of code that acknowledges its digital equivalence. Even though the conversion latency of the ADC12 is variable, Timer A insures that the time between samples is not.

#### **4.2.2 Bandpass Sub-Sampling Scheme for Frequency Translation**

A frequency of 49.08 kHz is ultimately used for sampling received waveforms within the 155-165 kHz band. The next two sections describe how and why these sub-sampled signals are translated. To analyze the spectrum of received signals within their carrier band, a controlled

experiment was carried out in a test tank. The transponder was pointed at the surface and operated as an echo-sounder by transmitting continuous wave (CW) bursts toward the surface and recording their reflections from the air/water interface. For this experiment, the ADC12 is configured to digitize signals at a rate of 413.8 kHz and, rather than saving the digitized samples internally, the ADC12 ISR is configured to output the 12-bit conversion onto unused I/O port pins of the MCU. From Least-Significant Bit (LSB) to Most-Significant Bit (MSB), the conversion result is immediately fed in parallel<sup>15</sup> out of the MCU (one pin per bit). The binary data is then transferred to an Intronix LogicPort logic analyzer through a multi-stranded shielded cable. PCB headers connect the port pins of the MCU to the cable (Figure 1.2 and Figure D.1). The logic analyzer is then used to capture and save 2,048 conversion results when triggered. Refer to Appendix Figure C.2 for a detailed description of this test setup. One such time-sampled received signal collected within the acoustic test tank is shown in Figure 4.4.

A digitized received signal is captured by the logic analyzer when setting the trigger level to an appropriate level. The received signal has a DC offset of over 0.6 V (normalized by the full-scale voltage). The ‘signal’ part of the data is characterized by a single amplitude CW burst whose rise and fall times are shaped by both the transmitting source that created it and the analog receiver that conditioned it. Because a self-reciprocity calibration setup was used to collect this data, these sources are one in the same. The transfer functions of both the analog transmitter and the analog receiver are, therefore, captured within this data (assuming the surface is a perfect reflector).

The DC offset is a by-product of the single-ended design of both the MCU’s ADC and the analog receiver. The SAR-ADC is configured such that full-scale and “zero” conversion results are referenced to supply voltage ( $V_{CC} = V_{BAT}$ ) and ground, respectively. Therefore, all sinusoidal signals digitized and measured by the MCU require an analog DC offset. To this end,

---

<sup>15</sup> Actually, two ports are needed to output the entire 12-bit result since only 8 pins were available per port. The asynchronous switching of the result, therefore, required an additional ‘data valid’ pin to signify that the parallel binary data displays the entire conversion result.

the buffered outputs of the analog receiver are directly coupled to the inputs of the MCU's ADC and provide the offset. Once converted to a digital equivalent, these signals will have a sample bias. The sample bias will be variable because the full-scale voltage ( $V_{FS}$ ) of the SAR-ADC is referenced to  $V_{BAT}$ , which drifts over the lifespan of the device. The green and blue ordinates in Figure 4.4 represent the analog and digital equivalence of this data, respectively. Since the conversion results are referenced to  $V_{CC}$  and since the battery voltage, again, varies between 2.8 and 3.0 V, the analog axis is normalized by  $V_{FS}$ .

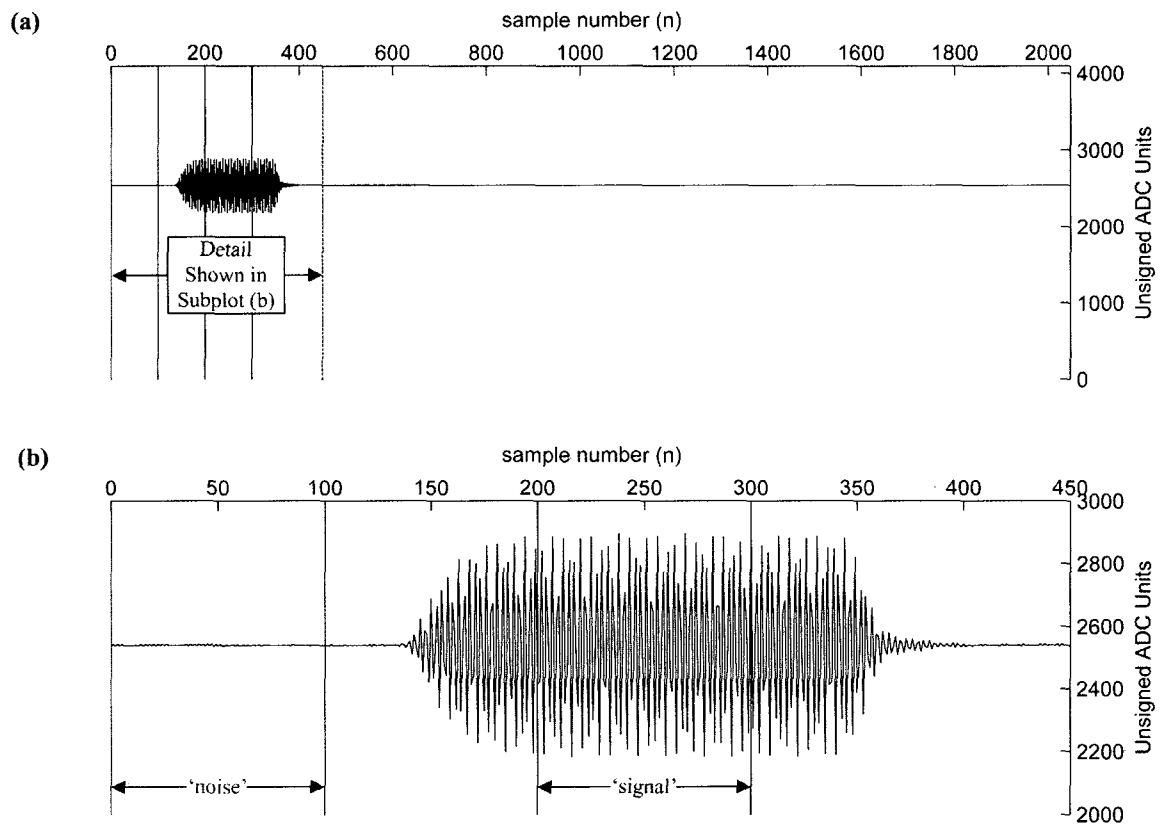


**Figure 4.4: Received Signal Collected within the Test Tank, Sampled at 413.8 kHz**  
 (a) shows the entire record while the (b) zooms in on the 'noise' and 'signal' sections as indicated by the red and black lines, respectively.

The pre-trigger buffer of the logic analyzer allows for the entire 500  $\mu$ s CW burst to be collected including its initial rise time. At a sampling rate of 413.8 kHz, approximately 207 of the 2,048 samples (or 10.1%) will constitute received 'signal' while the other 1,841 samples (or

89.9%) will be either ambient ‘noise’ or reverberation (from a previous transmission reflected within the test tank). Subsequent frequency analysis of received signals is described by the regions depicted in Figure 4.4: (1) The entire record of 2,048 samples is shown in blue (2), the ‘noise’ section is described by the selection of the record within the two red lines (i.e. the first 101 samples), lastly (3), the ‘signal’ section is described by the selection of the record within the two black lines (i.e. samples 200 through 300). To allow reverberation to die-off, ‘noise’ analysis was conducted on samples just prior to the direct-path CW ‘signal’ reception.

The frequency content of these data sets is analyzed in terms of their discrete Power Spectral Densities (PSDs). The periodogram ( $P_{XX}$ ) is used to calculate the non-parametric PSD estimate for a particular data set. The  $P_{XX}$  at a discrete frequency bin (denoted by the indexing variable, ‘k’) is calculated for a discrete-time data set,  $x(n)$ , as:

$$P_{XX}(k) = \frac{|DFT(x(n))|^2}{N^2 \Delta f} = \frac{|DFT(x(n))|^2}{N F_s} \Leftarrow DFT(x(n)) = X(k) = \sum_{n=0}^{N-1} x(n) e^{(-j2\pi k \cdot n/N)}$$

There are N-summed coefficients in the Discrete Fourier Transform (DFT) and therefore the magnitude squared spectrum is normalized by  $N^2$ .  $P_{XX}$  is calculated by dividing the normalized magnitude spectrum by the frequency resolution or bin width ( $\Delta f$ ) of that respective data set (where  $\Delta f = F_s/N$ ).  $P_{XX}$  (for all k values) is thusly calculated for the ‘entire’ data set of 2,048 samples. Likewise, the selected ‘signal’ portion of the data set is analyzed, albeit with less spectral resolution. Bartlett averaging of numerous periodograms is used to reduce the variance of the PSD estimate over the ‘noise’ portion of the data set. In this way, 35 independent subsets of the ‘noise’ were analyzed. All Bartlett ‘noise’ segments are taken from the first 101 samples captured by the sample buffer before a received CW burst is collected. The 35 Bartlett ‘noise’ segments are collected from 35 consecutive (hence independent) pings. The Bartlett periodogram ( $P_{XX}^B(k)$ ) is calculated as:

$$P_{XX}^B(k) = \frac{1}{35} \sum_{i=1}^{35} P_{XX}^{(i)}(k) , \text{ where } P_{XX}^{(i)}(k) \text{ is the periodogram of the } i^{\text{th}} \text{ noise segment.}$$

By analyzing the Bartlett PSD estimate of actual received ‘noise’ when sampling at 413.8 kHz, the spectral noise floor of the receiver is calculated up to and including the carrier band in which signals are communicated within the water column. When comparing the in-band ‘noise’ to the ‘signal’ only spectrum, the signal to noise ratio (SNR) at the output of the receiver is analyzed. Because the spectral resolution of these two PSD analyses is  $\sim 4$  kHz, an analysis of the entire record will give more detail ( $\Delta f \sim 200$  Hz) of the pulse shaping effects of the micro-transponder’s front-end. Figure 4.5 compares the single-sided PSD of these three analyses after the large sample bias is removed in each case. Note that a rectangular window was used (and should be assumed) when looking at the spectral content of this data.

The frequency response of the entire record illustrates the received signal’s spectrum. As expected this spectrum lies within the carrier band and its shape displays  $\sin(x)/x$  (or  $\text{sinc}(x)$ ) characteristics of its dual (Fourier transform of the time gated CW ‘burst’). With a PSD frequency resolution of  $\sim 200$  Hz and a signal period ( $T$ ) being a fraction of the entire record (500  $\mu\text{s}$ ), even the side lobes of the  $\text{sinc}(x)$  function were discretely visualized with nulls corresponding to 2 kHz spacing ( $1/T$ ). The magnitude of these lobes drops off more rapidly than the ideal case because of the band-limiting nature of the transponder’s analog front-end (exhibited as the rise and fall time of its dual). The lobes appear within the spectrum until the ‘noise’ floor is reached, at which point the PSD analysis exhibits large variance ( $\sim 20$  dB). These out-of-band signals are subject to noise, as expected.

To analyze the “type” of noise to which the receiver is sensitive, the Bartlett PSD estimate is used (single-sided result shown in red in Figure 4.5). Quantization noise from the ADC ultimately limits any digital receiver. If it is assumed that the quantization noise is evenly distributed over all discrete frequency bins, the PSD level can be shown to be independent of the number of bins and solely dependent upon conversion rate and the number of digitized bits. If ‘b’

represents the number of converted bits and the RMS quantization level is normalized by the Full-Scale Voltage ( $V_{FS}$ ), the  $P_{XX}$  for a discrete frequency bin is calculated as:

$$P_{XX}(k) = \frac{\left(\frac{0.707}{2^b}\right)^2}{N \Delta f} = \frac{\left(\frac{0.707}{2^b}\right)^2}{F_S} \Rightarrow P_{XX}^{dB}(k) = 10 \log_{10} \left( \frac{1}{2 F_S (2^{2b})} \right)$$

For a 12-bit ADC sampling rate of 413.8 kHz, the single-sided quantization noise PSD is roughly  $-128 \text{ dB re } (1 V_{RMS}/V_{FS})^2 / \text{Hz}$ . Therefore, the behavior of the Bartlett PSD from DC to  $\sim 140 \text{ kHz}$  is characterized by quantization noise effects of the 12-bit ADC.

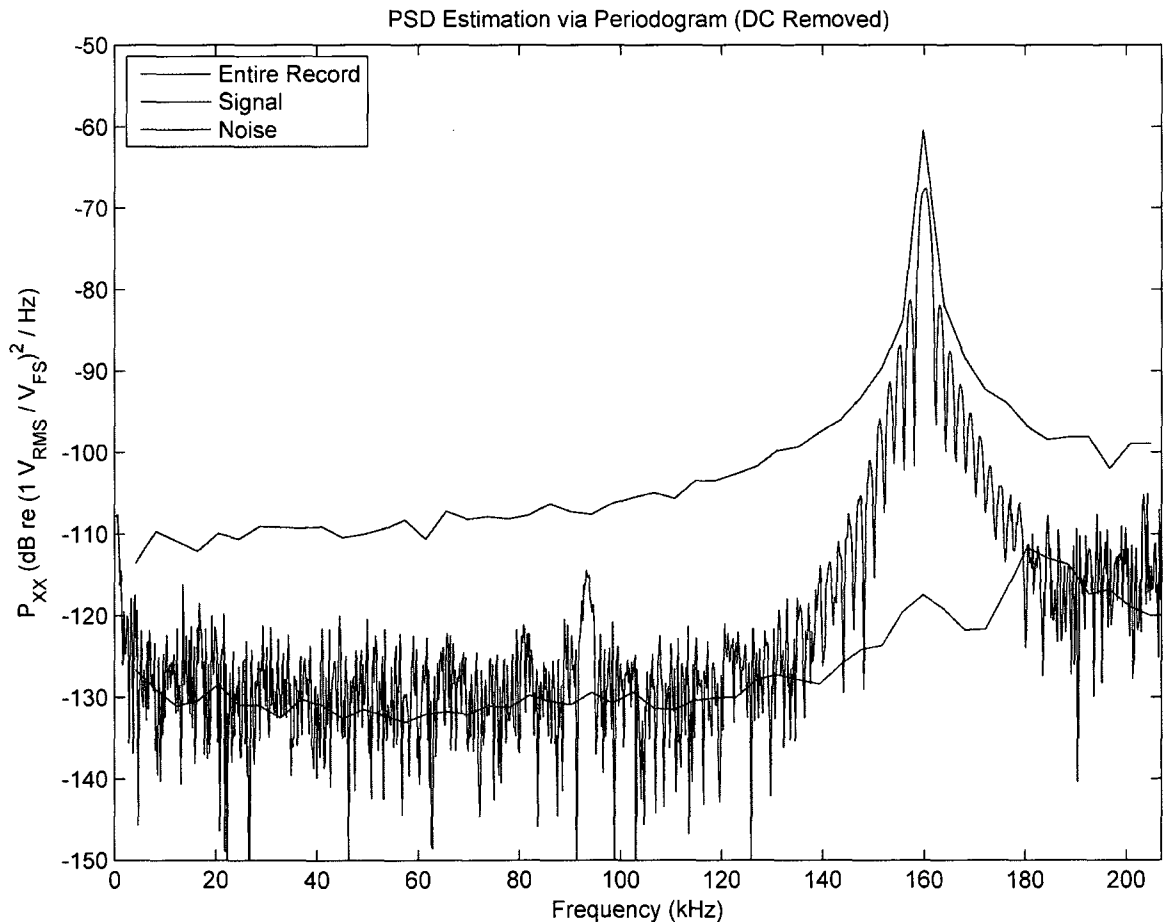


**Figure 4.5: Frequency Response of Received Signal(s), Sampled at  $F_S = 413.8 \text{ kHz}$**

The PSD analysis of the 'Entire Sample Record' is compared with the 'signal' and 'noise' portions. Noise is analyzed through Bartlett Spectral Estimation methods on 35 independent sample records.

As shown in Figure 4.5, the 'noise' analysis deviates from this quantization level in two



locations: within the carrier band (150-170 kHz) and over the piezoelectric transducer's source-mode self-resonance band (180-190 kHz). Detection of 'signal' within these regions is then limited by some factor other than the quantization effects of the ADC. Further analysis suggests that this in-band noise is elevated by reverberation within the tank and not by ambient acoustic sources or the electronic noise within the signal path.

The PSD of the 'signal' portion of the data set is calculated using the periodogram; it is displayed in black in Figure 4.5. Even though this data is visualized through straight line interpolation, it is important to note the discrete nature of these results. The ideal spectrum of a 244  $\mu$ s segment of a 160 kHz sinusoid (equivalent to 101 samples at 413.8 kHz) is a sinc(x) function centered at 160 kHz with nulls that correspond to  $\sim 4$  kHz spacing. But since the carrier frequency is not an integer number of  $\Delta f$  frequency bins, the discrete spectrum does not sample the nulls, resulting in spectral leakage. Despite the greater bin width, the PSD of the isolated 'signal' portion is nominally greater than that of the PSD of the entire record. With all things being constant the PSD value of the bin corresponding to 160 kHz should be  $\sim 13$  dB greater for the entire record because the periodogram was divided by smaller bin widths (202 Hz vs. 4 kHz in the isolated case). But the average power of the two time-sampled data sets is not the same. Because 'signal' is present for only a tenth of the time, the average power of the 'entire' record is reduced. Therefore, the PSD estimate of the entire record is reduced by  $\sim 20$  dB within the carrier band, thus explaining the 7 dB offset at the 160 kHz bin.

Although these received signals were converted and collected at a rate of 413.8 kHz, this (high) sampling rate is shown to be impractical for the design of the transponder's digital receiver. Processing of digital samples in real-time requires all CPU operation to be carried out before a new sample (or set of samples) is collected. In other words, the digital receiver must determine the significance and come to a decision based on the sample (or sample set) just collected before any new data can be processed, or else signal processing in real-time is not

possible. At a sampling rate of 413.8 kHz and MCLK set to 12 MHz, 29 CPU clock cycles are available for processing data before another sample result is converted (less than 20 with MCLK set to 8 MHz). As previously stated, a minimum of 6 clock cycles are required to acknowledge that a sample was just converted. Simply reading the value of the converted sample takes another 3 - 6 clock cycles. The remaining balance of CPU clock cycles could not, therefore, warrant Digital Signal Processing (DSP) at this rate. In fact, the ISR code that is used to output the converted sample onto the parallel port pins of the MCU (at this rate) barely met the real-time requirements. This illustrates the fundamental problem with sampling the carrier band at a rate that is twice its highest frequency component (referred to as ‘traditional lowpass Nyquist sampling’ in Lyons’ text on Digital Signal Processing). Namely, sampling at this rate requires a faster ADC clock, demands more power when processing due to the required increase in CPU clock, and is unnecessary for narrow-band bandpass signals. Because information is transmitted and received within a narrow band and the traditional Nyquist rate preserves all lowpass spectral content up to and including this band, most of the spectrum is not used. Sampling at this rate is redundant. Heterodyning (or mixing) may be implemented to greatly reduce the sampling rate. This technique is described in the literature as “bandpass sampling” (Lyons, 2004).

Bandpass sampling intentionally aliases the analog spectrum and shifts its content to a lower frequency. Upon digitization, the analog spectrum is replicated at integer multiples of the sampling rate. By sampling at a sub-Nyquist rate, spectral images of the analog band are shifted to a lower band. Thus, heterodyning is achieved. Lyons (2004, Ch. 2) describes this method in detail. The following equation gives the sampling frequency necessary to translate the carrier band ( $F_0$ ) by a sub-sampling frequency ( $F_{SS}$ ) and center the band at one-fourth of this sub-sampled rate ( $F_{SS}/4$ ).

$$F_{SS} = \frac{4 F_0}{N}$$

With an ‘N’ value of 13, a sub-sampling frequency of 49.23 kHz will ideally translate 160 kHz

down to  $\sim 12.3$  kHz. However, a sampling rate of 49.08 kHz could be synthesized by Timer A, configured with SMCLK at 8 MHz, and therefore is used. By sub-sampling at this frequency, 163 CPU clock cycles occur between successive samples (MCLK also set to 8 MHz). This provides more time (more clock cycles) for signal processing of these converted samples. Similar to the test setup used to collect received signals sampled at 413.8 kHz, sub-sampled data was acquired in the test tank by aiming the transducer at the surface, transmitting a 160 kHz CW burst (500  $\mu$ s long), and receiving its reflected signal. Timer A was configured to trigger the sample mode of the SAR-ADC at the sub-sampled rate shown in Figure 4.2. One such time-sampled received signal collected at this lower rate is shown in Figure 4.6.

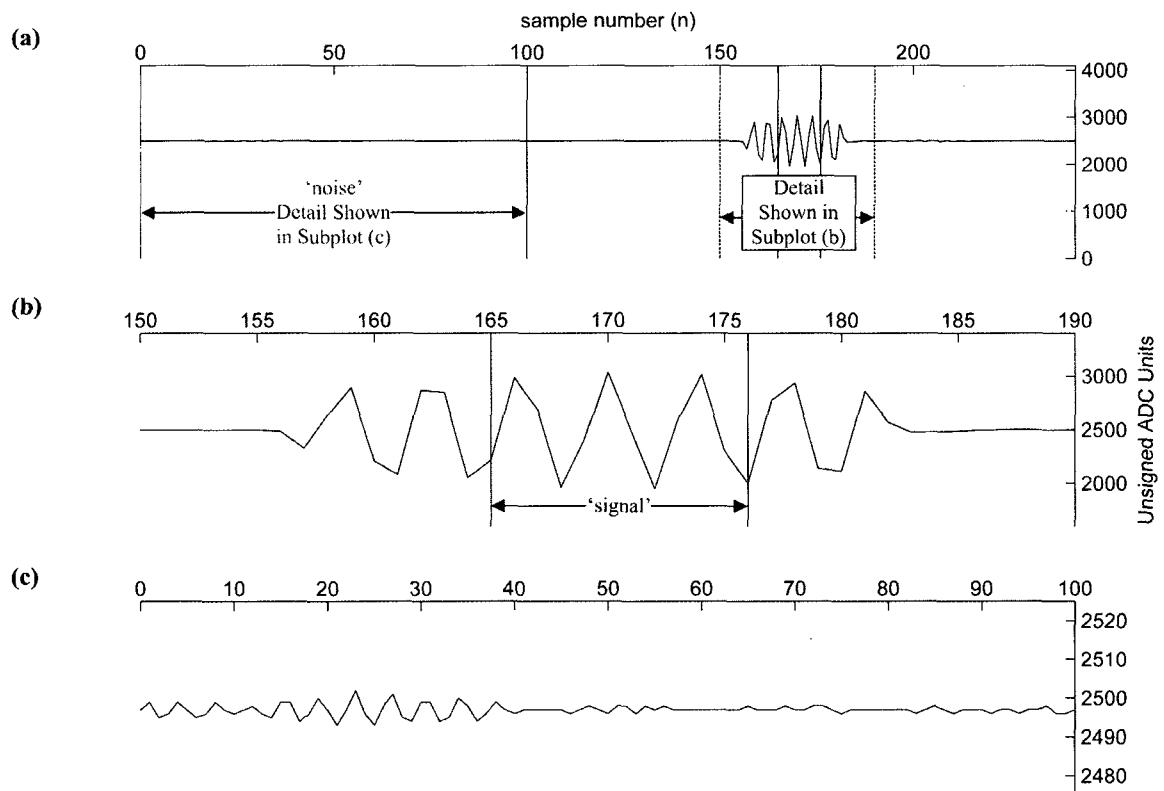


**Figure 4.6: Received Signal Collected within the Test Tank, Sampled at 49.08 kHz**  
 (a) displays of the entire 243 sample record. The 'signal' and 'noise' sections are annotated as the data between the black and red lines, respectively. The details of these sections are shown in (b) and (c), respectively. Some remnant of the pulse (from a previous ping) is seen between 0.2 and 0.8 ms in (c).

Being sub-sampled, the 160 kHz CW burst is now represented with about one tenth of the original number of samples. With the pre-trigger buffer set to capture the same number of samples before a ‘trigger’ event, more time elapses before a CW burst. The burst or ‘signal’ is now captured within the data set at around 3.25 ms. Spectral analysis is performed on the following sections of this record: (1) the entire record of 243 samples, (2) 12 ‘signal’ samples of the CW burst, and (3) the first 101 ‘noise’ samples. The latter two are annotated, as such, and enlarged within (b) and (c) of Figure 4.6. The discrete periodogram algorithm is again used to estimate the PSD of received signals, while the Bartlett spectral averaging method is used to estimate the PSD of the ‘noise.’ Bartlett averaging is performed on 14 independent sample sets collected by the pre-trigger buffer of the logic analyzer. These sets were collected prior to the CW burst. The sample bias is again removed prior to all PSD calculations and is therefore not included in the following single-sided spectral plots.

The discrete spectrum of the received signal displays the sinc(x) characteristics of the carrier band and, as expected, is translated to  $\sim 12.76$  kHz<sup>16</sup>. This is explicitly shown by the PSD analysis of the ‘entire’ record while implied by PSD analysis of the ‘signal’ only record. Again, their relative spectral peaks differ by  $\sim 7$  dB because of differences in their frequency resolution (bin width) and average power. By sub-sampling, information preserved within the carrier band (150-170 kHz) is translated down and centered within the discrete spectrum and bounded by the sub-sampled folding frequency ( $F_{SS}/2$ ). It is important to note that further translation to baseband could not be directly achieved because a large unstable bias is present in these digitized samples. It is therefore necessary to remove the sample bias before further translating the spectrum to baseband.

---

<sup>16</sup> Due to the non-ideal synthesis of the sub-sampling frequency, the 160 kHz carrier differs by +500 Hz from  $F_S/4$ .

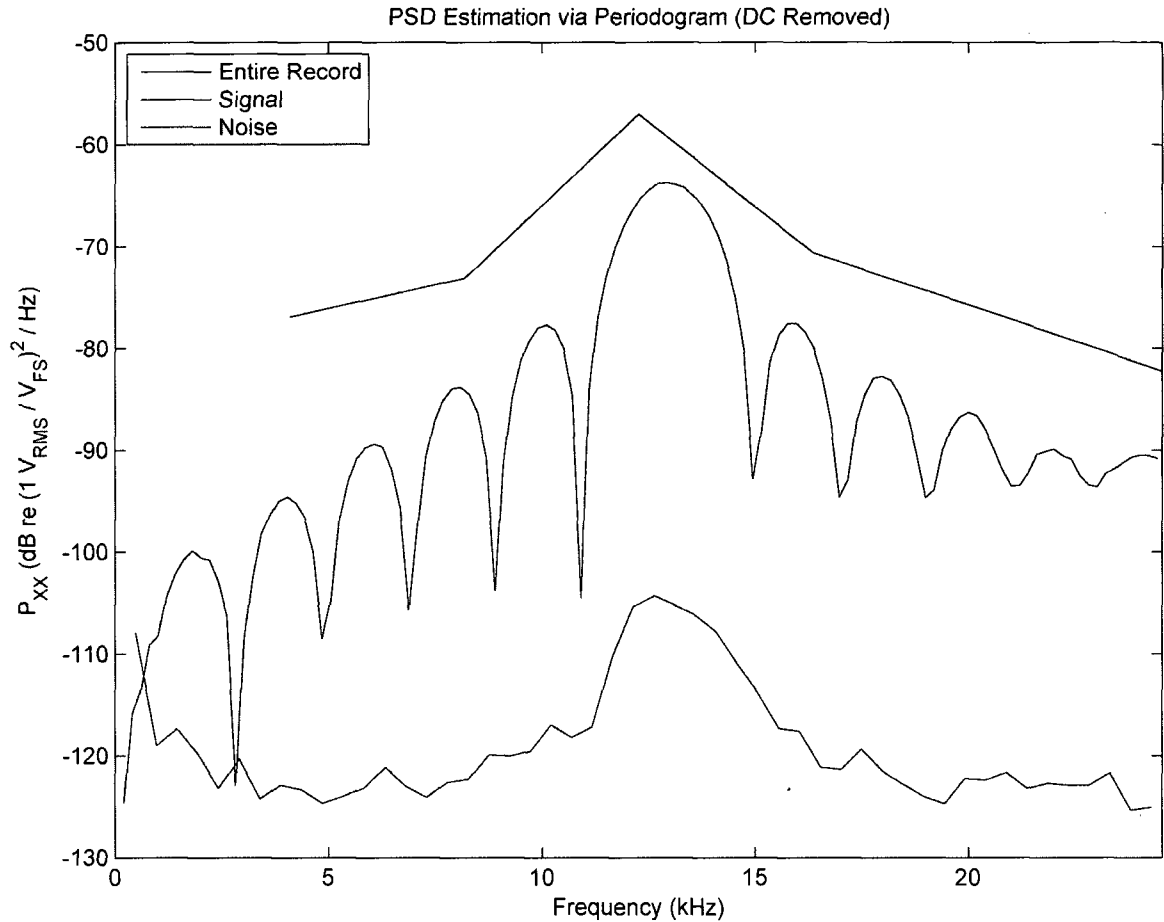


**Figure 4.7: Frequency Response of Received Signal(s), Sampled at  $F_{SS} = 49.08$  kHz**  
 The PSD analysis of the ‘Entire Sample Record’ is compared with the ‘signal’ and ‘noise’ portions. Noise is analyzed through Bartlett Spectral Estimation methods on 35 independent sample records. Around 12 kHz, the noise spectrum shows evidence of the signal remnant seen in Figure 4.6 (c).

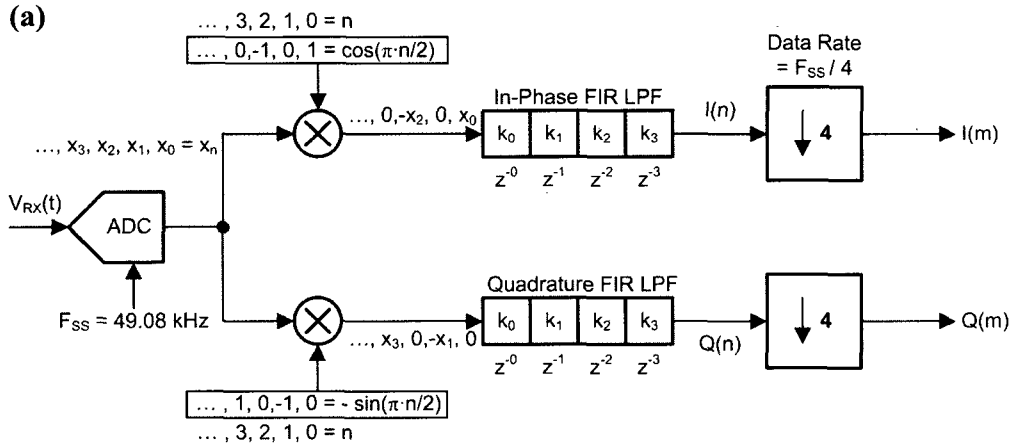
The Bartlett PSD estimate of the ‘noise’ suggests that reverberation might have shaped the noise floor within the carrier band when repetitively transmitting and receiving at a one second rate. Again, the quantization noise of the ADC12 is analyzed by evenly distributing its normalized average (RMS) power level over the entire discrete spectrum, the single-sided analysis of which is calculated to be around  $-119$  dB re  $(1V_{RMS}/V_{FS})^2/Hz$  at the sub-sampled rate. The Bartlett PSD estimate of the ‘noise’ differs from this spectral level around the  $F_{SS}/4$  band. Within this band, the shape of the Bartlett ‘noise’ estimate mimics the main lobe of the ‘signal’ spectrum. This suggests that ‘signal’ might have entered the ‘noise’ calculation. Further

correlation of these sections in time confirms this statement. By inspection of the Bartlett ‘noise’ segment in Figure 4.6 (c) from sample number 12 through 38, ‘signal’ similar to the isolated CW Burst in Figure 4.6 (b) is observed within this data set (albeit attenuated by a factor of 100). This illustrates that collecting ‘noise’ in the midst of repetitive transmissions does not allow for the absolute minimum ‘spectral’ floor to be analyzed. It does, however, illustrate the problem with detection. Because the receiver is extremely sensitive, when transmitting at a regular rate the spectral ‘noise’ floor is elevated by reverberation within the acoustic environment. The threshold of the detector must therefore be increased when transmitting at a regular rate within a reverberant environment.

### **4.2.3 Real-Time Demodulation and Detection of Sampled Signals**

The digital receiver’s real-time signal processing is decision-directed and aimed at determining if a set of samples is representative of ‘signal’ or ‘noise.’ A quadrature digital demodulator is implemented, in real-time, for complex down conversion of received signals and is configured to remove sample bias within its processing. In-Phase (I) and Quadrature (Q) components of the signal are extracted by the demodulator and are further down converted to baseband through down-sampling. The quadrature parts (I/Q) are then combined for magnitude detection of a ‘signal.’ A sub-sampling rate greater than four times the analog receiver’s bandwidth is required for this type of demodulation. Furthermore, a sub-sampling rate that translates the carrier band to  $F_{SS}/4$  is “attractive because it greatly simplifies” the demodulator’s design (Lyons, 2004).  $F_{SS} \sim 49$  kHz to ensure that these two criteria are met (Section 4.2.2).

Figure 4.8 illustrates the block diagram of the quadrature digital demodulator implemented in the embedded design. By down-sampling the collected samples at the onset of signal processing, the amount of CPU clock cycles available for real-time processing was increased by the down-sampling factor. Figure 4.8 shows how the implemented design (c) is equivalent to Lyons’ text book design (a).



(b)

FIR Input Samples

Quadrature				In-Phase				n	m
$z^0$	$z^{-1}$	$z^{-2}$	$z^{-3}$	$z^0$	$z^{-1}$	$z^{-2}$	$z^{-3}$		
$x_3$	0	$-x_1$	0	0	$-x_2$	0	$x_0$	3	0
0	$x_3$	0	$-x_1$	$x_4$	0	$-x_2$	0	4	
$-x_5$	0	$x_3$	0	0	$x_4$	0	$-x_2$	5	
0	$-x_5$	0	$x_3$	$-x_6$	0	$x_4$	0	6	
$x_7$	0	$-x_5$	0	0	$-x_6$	0	$x_4$	7	1
$\vdots$	$\vdots$	$\vdots$	$\vdots$	$\vdots$	$\vdots$	$\vdots$	$\vdots$	$\vdots$	$\vdots$

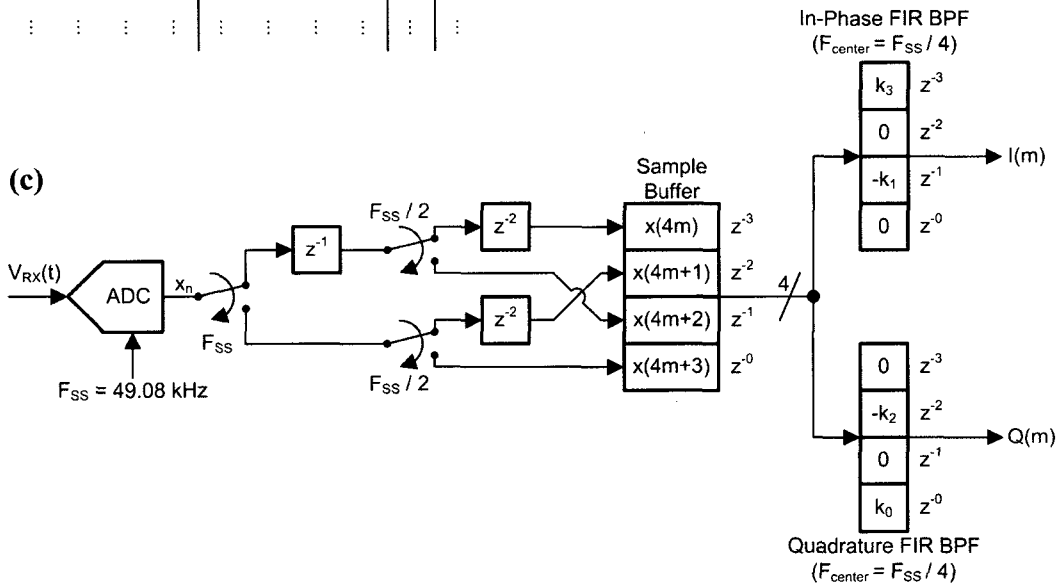


**Figure 4.8: Block Diagram of the Quadrature Digital Demodulator**

Lyon's I/Q demodulator is shown in (a). The samples input into its I/Q FIR LPF sections are shown in (b) and compared with the I/Q demodulator implemented in the microtransponder's digital receiver (c). This design moves the down conversion to the front of the demodulation scheme and implements I/Q FIR BPF through parallel processing. Notice that both (a) and (c) results in the same I(m)/Q(m) demodulated outputs.

Digital mixing is easily accomplished with the spectrum centered at  $F_{SS}/4$ . Sinusoidal mixing components at  $F_{SS}/4$  are one of three values: 1, 0, or -1. When received samples,  $x(n)$ , are mixed with these values, multiplication can be avoided. The sample value is either taken as-is (when multiplied by 1), not taken (when multiplied by 0) or sign inverted (when multiplied by -1). Quadrature parts are extracted from the received signal because the two digital mixers are  $90^\circ$  out-of-phase. A Finite Impulse Response (FIR) lowpass filter (LPF) is then used to attenuate 'spectral images' that were translated to  $F_{SS}/2$  in the mixing process. Since digital mixing is followed by an FIR LPF, every other filter coefficient is effectively zeroed while the non-zeroed coefficients are opposite in sign (Figure 4.8 (b)). In this way, the combination of digital mixing and lowpass FIR filtering is equivalent to an FIR BPF centered at  $F_{SS}/4$ . By retaining every fourth FIR sample result (highlighted in red), the frequency of I/Q results is reduced to 12.27 kHz (indicated by the change in sample index, 'm'). The sub-sampled spectrum, once centered at 12.27 kHz, is thereby demodulated to baseband. Because down-sampling retains only a fourth of the filtered I/Q results, actually performing all of these computations is seen as superfluous in practice. Therefore, down-sampling is done up-front. Samples are collected in a circular 'sample' buffer and processed in parallel at the down-sampled rate of 12.27 kHz. Figure 4.8 (c) shows how the quadrature digital demodulator was implemented in the micro-transponder. Notice that block diagrams (a) and (c) produce the same I and Q results.

The quadrature digital demodulator that Lyons demonstrates in his textbook uses an odd number of FIR filter taps. Doing so ensures that the filtered I and Q results are indeed  $90^\circ$  out of phase over the entire sampled spectrum. Unfortunately, bias is not completely notched by an FIR filter that sums an odd number of non-zero coefficients. For a mixing scheme that uses sampled sinusoids such as 1, 0, -1, 0, 1, ..., the summation of any 4 successive samples has a zero DC value. To ensure that this was the case, the size of the sample buffer is forced to be an integer multiple of 4. In this way any sample bias is easily removed, while keeping the magnitude of the spectrum intact. However, because the FIR BPF's coefficients are not symmetrical, the phase of



the filtered spectrum is compromised away from the  $F_{SS}/4$  passband. That is, I and Q are not exactly  $90^\circ$  out of phase. Fortunately, the design of the detector is kept simple and uses the magnitude of the quadrature parts and not the phase between them to determine if a 'signal' is received.

The detector computes the magnitude of the received samples by summing its squared quadrature components ( $I^2+Q^2$ ). This computation requires three operations: two multiplications and one addition. Because the Arithmetic Logic Unit (ALU) within the CPU of the MSP430 does not support multiplication, a dedicated hardware multiplier (peripheral) is required for this computation. Unlike the other peripheral modules used within the developed code, the action of the hardware multiplier is not transparent. The IAR C/C++ compiler simply replaces every instance of 'multiplication' with the equivalent machine code necessary to configure this peripheral. Unlike other peripherals used, the hardware multiplier's ISR is 'called' by the executing code and its result is then returned upon completion. The compiler takes into account the data type (size) of variables within all mathematical expressions and, in their place, substitutes the machine code necessary to compute the result. When downloaded to the target, the IAR IDE displays the equivalent disassembly code that the CPU executes for each compiled expression. In this way, the disassembly code shows how the MCU performs all operations including how the hardware multiplier is configured. The amount of CPU clock cycles required for any mathematical operation depends upon the type of operation and the number of bits used to represent the variables within the expression.

All real-time signal processing operations are conducted on variable values represented in fixed-point format. Received samples are converted to 12-bits and stored as 'words' within RAM (16 bits or 2 bytes). If the FIR BPFs' non-zero coefficients are equally weighted and have a magnitude of one, the maximum number of bits needed to represent each quadrature result will be

12 bits<sup>17</sup> plus one bit per every two (non-zero) summed sample values. Furthermore, the summed result will then need to be represented by a signed fixed-point format since the bias is removed. By restricting the data size of samples stored in the sample buffer to 16 bits, I and Q are represented as signed integers (one word = 16 bits). The square of the quadrature components (computed as  $I \times I$  or  $Q \times Q$ ) must therefore be represented by two words, i.e. a 'long' or 'double' data type. The hardware multiplier is therefore configured by the compiler for 32-bit multiplication. The number of CPU clock cycles required to perform a single instruction within the MCU is a function of the instruction type (format) and the addressing mode by which the operands are gathered. By careful inspection of the disassembly code and by referencing the MSP430 user's guide, the number of CPU clock cycles required for a compiled operation was determined to be: 51 clock cycles for a single 32-bit multiplication and 128 clock cycles for the entire magnitude computation. Because many CPU cycles are needed for a single multiplication operation, the number of multiplication operations is minimized to the two necessary to compute the magnitude. No additional multiplication operations were used when computing the quadrature components. The detector then compares the magnitude calculation to a threshold value (empirically selected in this case) and makes a binary decision: 'signal' or 'noise.' After six consecutive sub-sampled decimated counts of 'signal' the detector determines that the transponder is being interrogated by a 500  $\mu$ s 'burst.'

Because samples are gathered and processed four-at-a-time, the digital receiver demodulates and detects the sample set in parallel to the actions of the ADC12. All real-time signal processing is carried out before another four samples are gathered. Figure 4.9 displays the time constraints of signal processing events as carried out by the digital receiver.

---

<sup>17</sup> Because the analog receiver is clamped by diodes, only ~42% of the full dynamic range of the ADC is ever used. The subtraction of two samples can safely be represented by 11 (rather than 12) bits.

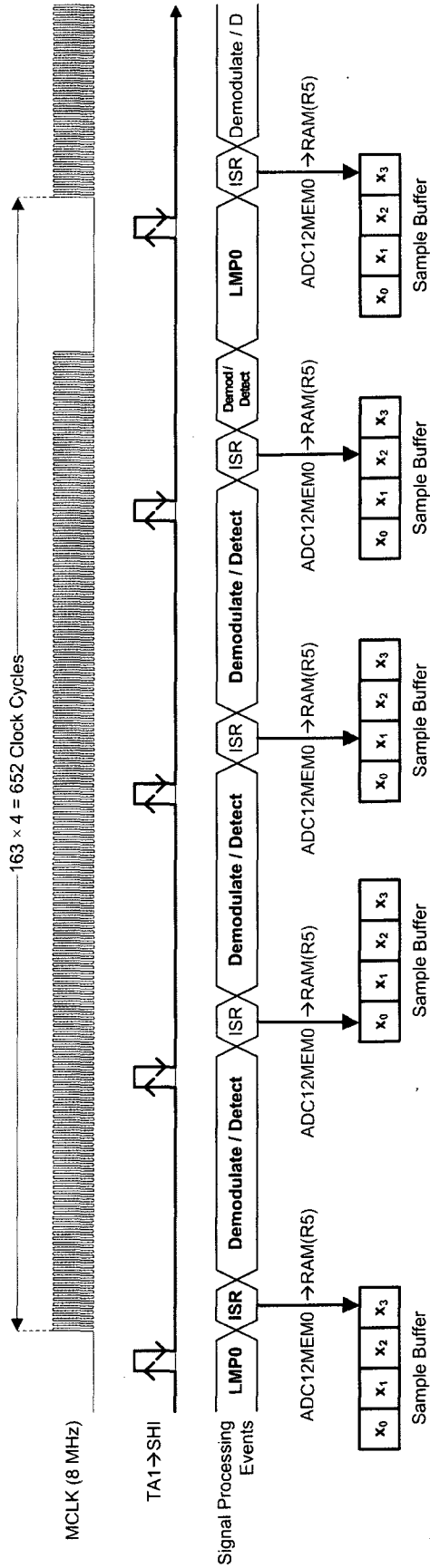


**Figure 4.9: Timing Constraints when Processing Samples in Real-Time**

Signal processing only takes place when the circular buffer obtains four new samples. Once collected, their values are processed in parallel to the collection of 4 new samples. Because storing the converted samples takes 25 MCLK cycles away from the CPU, signal demodulation and detection must be carried out within 552 MCLK cycles. The colors annotate the signal processing events of a collected sample set: grey indicates the processing of the current sample set, blue indicates the processing of the previous sample set, and red indicates the processing of the next sample set. 'Demodulate / Detect' events indicate the processing time that could be used when processing the current sample set. Once this routine is finished, the receiver is put into LMP0 to conserve power. This event stops the MCLK and is generically indicated in this figure.

Samples are collected and stored in a circular (sample) buffer in parallel to the real-time processing of the previously collected set. After the ISR of the fourth consecutively collected sample stores the result to RAM and gives control to the CPU, signal processing begins. Including overhead, each ADC12 ISR event takes a total of 25 CPU clock cycles to store the converted result, update the modulo pointer (R5), and return the CPU to AM (whether the processor is powered down or not). 4 additional clock cycles are required to test if the sample just collected was the 4<sup>th</sup> consecutive sample. Because the sample buffer is kept small (a minimum length of 4) and the FIR BPF's non-zero coefficients are equally weighted and have a magnitude of one, quadrature parts are extracted from the sample set in only 20 clock cycles. The detector then needs 128 additional clock cycles to compute the magnitude of the complex signal. This operation will invariably be interrupted by the ISR storing the next conversion result to memory (shown in Figure 4.9 as the red 'x<sub>0</sub>' going into the sample buffer). An additional 25 clock cycle ADC12 ISR event will commence. From inspection, x<sub>0</sub> must be used or moved before this ISR event occurs because a new value will be written in its place. The magnitude result is then compared to a threshold value (stored within RAM). Because the magnitude result is 32 bits in length (2 words), this comparison is variable. If the result is greater than the Most-Significant Word (MSW), then the comparison only takes 6 clock cycles. An additional 8 clock cycles is required to make the comparison of the Least-Significant Word (LSW). If the magnitude result is greater than the threshold, 'signal' is detected and the 'signal period counter' is incremented by one (4 clock cycles). Finally, the detector checks the 'signal period counter' and determines if a 'burst' has occurred. At an I/Q rate of 12.27 kHz, 6 consecutive 'signal' detector decisions constitute a ~500μs burst. This final comparison takes an additional 7 clock cycles. The entire critical path for real-time signal processing of the sample set takes 177 clock cycles. Dovetailed with the 4 parallel ISR events, the CPU will need to be active (in AM) for 277 of every 652 clock cycles (42.5%). For the remaining time the CPU can be powered down and the device can rest in LPM0, thereby reducing the current consumption of the device. When

receiving, the average current consumption of the MSP430 is reduced to ~1.5 mA by the following equation:

$$I_{RX}^{MCU} = (0.425 I_{AM}) + (0.575 I_{LPM0}) = (0.425 (3mA)) + (0.575 (378.3\mu A)) \approx 1.5mA$$

The up-front decimation is not only necessary (because the critical path takes longer than 163 clock cycles); it allows the MCU to be powered down for a majority of the time and therefore reduces the average power of device by 50% when receiving.

### **4.3 Transmitter Digital Design**

When a signal is detected by the digital receiver, power is shut down to the analog receiver sub-systems of the design and the routine for “transmitting a coded message” starts. This subroutine uses peripheral driven ISR techniques for power efficient and accurate generation of transmit signals, similar to those employed in the receiver’s digital design. The flow chart in Figure 4.10 describes the embedded code implemented by the micro-transponder when transmitting a coded signal.

The transmitter’s routine (1) disables the channel of the Grounding FET (2) enables the boost converter and waits for its transient startup, (3) enables the full-bridge driver, and (4) configures Timer A to output a PWM signal. An IFG for Timer A is enabled, whereby an ISR can control the generated PWM signal. Although the control of the PWM signals is kept simple in this design (‘on’ or ‘off’), the duty cycle, period, and phase could all be changed within the ISR design ‘on-the-fly’. This would enable the frequency or phase content of the encoded transmit signal to be discretely modulated. The DCO is set to 12 MHz and sources MCLK and SMCLK to the CPU and peripheral modules, respectively. This higher frequency allows for finer control of the carrier frequency at the expense of increased current consumption of the MCU. Since the majority of the power-demand in TX mode will be from the boost converter and driver of the LT3572 IC, a slight increase to the current consumed by the MCU at the expense of a more

accurate transmit signal was seen as a worthy trade-off. The execution of instructions and timing of the peripheral operations (when transmitting) is henceforth made with respect to this DCO frequency.

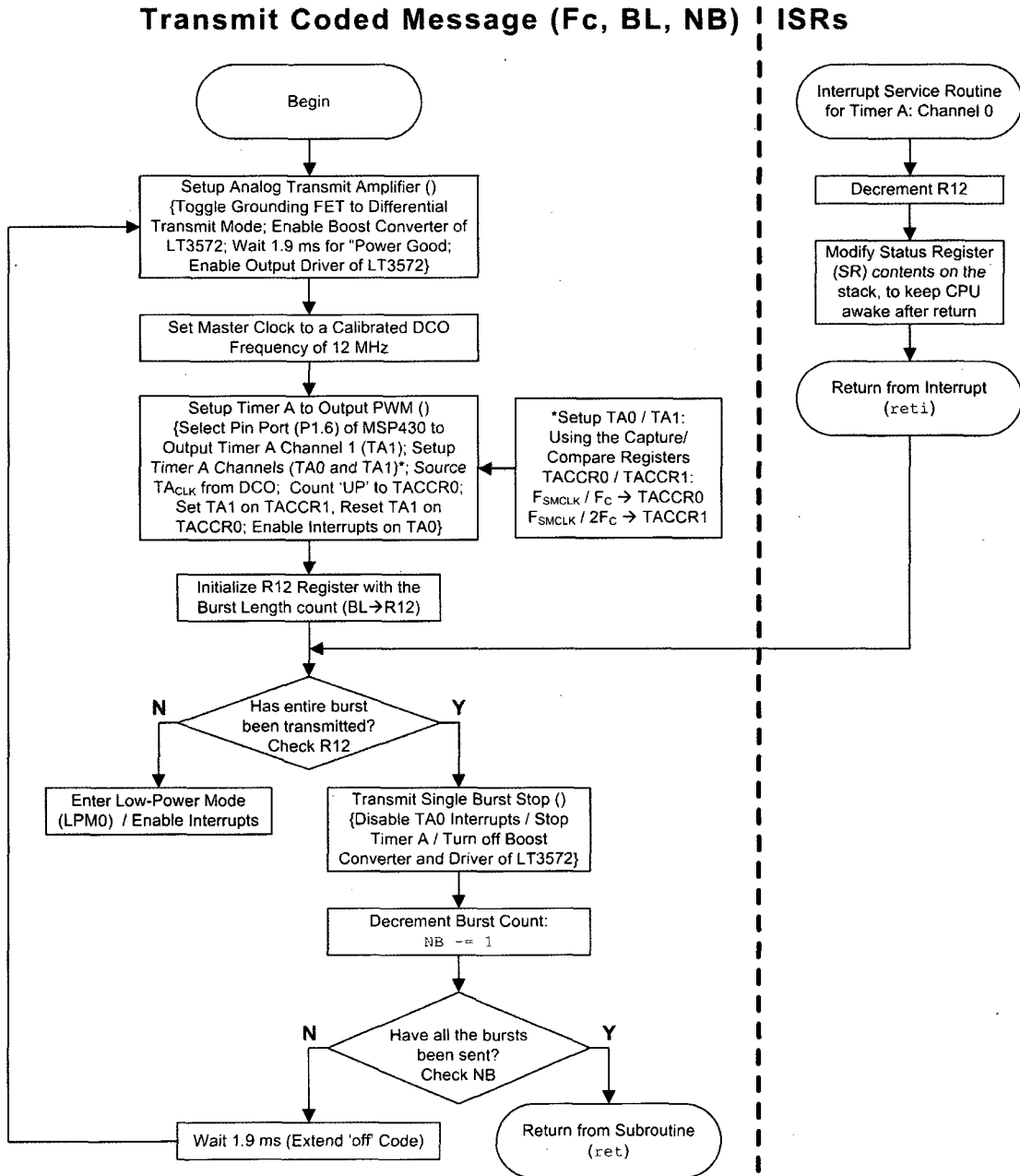


**Figure 4.10: Flow Chart of a Coded-Signal Transmission**

The transmitter's routine transmits a single CW burst within a loop controlled by Timer A. Its ISR keeps track of how many half cycles have been transmitted. Once the routine determines that the entire burst has been transmitted it checks whether the entire code of sequential CW burst's has been transmitted. If it has then it returns control to the receive algorithm. The critical path is indicated in red.

Timer A is then configured to output the PWM signal onto the port pin that connects the MCU to the PWM input of the LT3572 IC (Figures D.1 and 3.13, respectively). The Burst Length (BL) count variable is then loaded into one of the CPU's general purpose registers that can be passed-to and modified-by an ISR (R12 in this case). Timer A's ISR simply decrements this variable and returns code execution to the CPU. The CPU checks if R12 is fully decremented. If not, the CPU is put to sleep (in LPM0) until another IFG is set by Timer A, indicating that another PWM cycle has been transmitted. If the entire burst has been transmitted (indicated by R12 being decremented to zero), the timer is stopped and the LT3572 IC is powered down. The routine then decrements the Number of Bursts (NB) variable, and determines if all bursts have been transmitted. If not, a 'wait' routine extends the 'off' code and transmission begins again. When all CW bursts have been transmitted, the transmitting routine returns control to the main (receiving) algorithm.

Timer A is configured to generate a 160 kHz ~50% duty cycle pulse train. Figure 4.11 shows how Timer A is configured and the output signal that it creates.

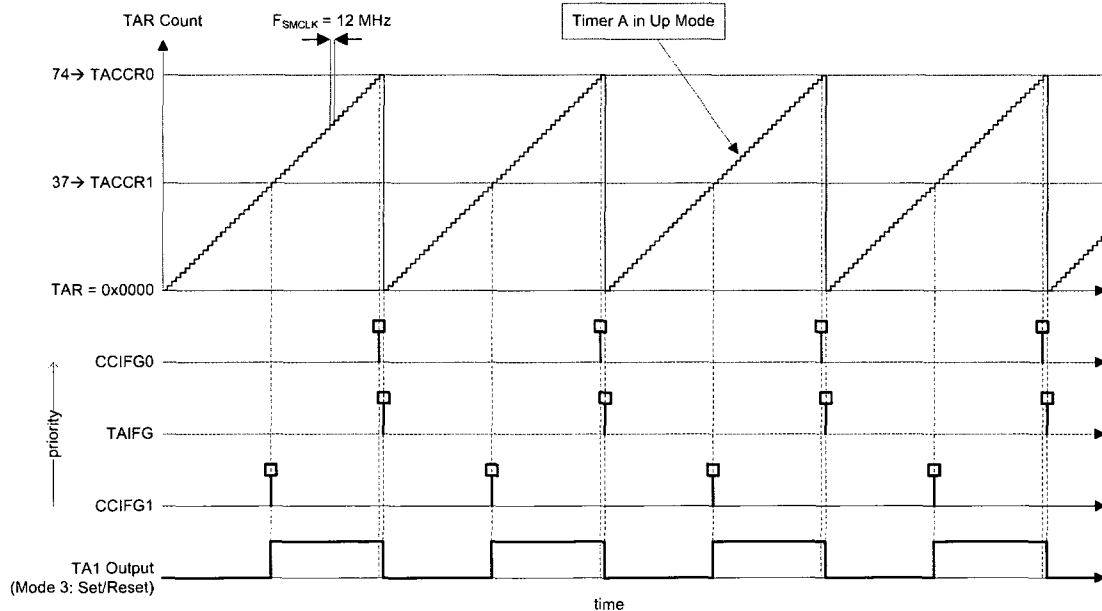


**Figure 4.11: Producing a 50% Duty Cycle 160 kHz Signal with Timer A**

Channel 1 of Timer A is directly output onto the port pin connecting the MCU to the transmit switching amplifier. When enabled by the MCU, this amplifier drives the transducer with the signal created by Timer A as controlled by the transmit algorithm.

Timer A is configured to count up to the value stored in the first capture/compare register (TACCR0). Since the count starts at zero, the period of the output signal is one greater than the integer stored in TACCR0. With the DCO sourcing SMCLK at 12 MHz and with the TACCR0 set to 74, the output (carrier) frequency is 160 kHz. When the TAR count reaches the value stored in TACCR0, the Capture and Compare Flag for the timer's first channel (CCIFG0) is set. This IFG has highest priority and is not vectored (requiring no additional clock cycles to decode the source of the IFG via a look up table). Thus, the CCIFG0 is enabled in the design. When this IFG event occurs, the CPU returns control to the ISR after 7 additional clock cycles: 1 is required for the CPU to wake up from LPM0 and re-establish MCLK, while another 6 clock cycles are necessary before the ISR address can be pushed into the PC and servicing can start. The duty cycle of the timer's output can be controlled for channels other than zero, thus channel one is used. The value stored in TACCR1 controls the IFG for channel 1 (CCIFG1). For Timer A operating in mode three, the output of channel 1 (TA1) is set upon CCIFG1 and reset upon the timer count returning to zero (a TAIFG event). With TACCR1 set to 37, the TA1 output will be set (high) 50.7% of the time and reset (low) 49.3% of the time. Because TACCR0 is even (resulting in TAR counting an odd number of clock cycles), the duty cycle cannot be exactly 50%. However, the synthesis of two other in-band carrier frequencies, each with a 50% duty cycle, can be configured with an SMCLK sourcing Timer A at 12 MHz:  $F_C \approx 157.9$  kHz (from TACCR0 = 75 and TACCR1 = 38) and  $F_C \approx 162.2$  kHz (from TACCR0 = 73 and TACCR1 = 37).

Because the encoded signal is kept simple in this design (either 'on' or 'off'), the critical path of the ISR based code flow affords the CPU to be shut down for a majority of the time. The CPU need only be active for 24 out of every 75 clock cycles in this design. When transmitting, the average current consumption of the MSP430 is thusly calculated to be ~1.7 mA:

$$I_{TX}^{MCU} = (0.32 \times I_{AM}) + (0.68 \times I_{LPM0}) = (0.32 \times 4.25mA) + (0.68 \times 510.5\mu A) \approx 1.7 mA$$



However, because the LT3572 IC demands much more power, optimization of current consumed by the MSP430 in TX mode is seen as being secondary to functionality. Subsequent functional improvements to the digital transmitter design will result in increases to the average current consumption.

#### **4.4 Turnaround Time Latency and Uncertainty**

When used for tracking its position, knowing the transponder's turnaround and reply latency is critical in estimating range. To ensure an accurate estimate, the turnaround time ( $T_{TA}$ ) should be fixed and possess as little variability as possible. Fortunately, the actions of the microcontroller are highly predictable. Because the MCU detects received signals and generates the reply waveform itself, an analysis of the code flow that results in an encoded transmission will determine the reply delay ( $T_{RD}$ ) of the device. A careful analysis of the disassembly code will afford us this knowledge.

Upon 6 consecutive 'signal' detections, the MCU will shut down the receiver, turn on the transmit IC, and generate a PWM signal that is differentially applied to transducer. Detector decisions occur once in every four new samples collected. Because the sample buffer (being of length four) only retains these new samples, there will be no overlap in signal processing. The decision to reply will therefore be based on only 24 samples. For now, let us focus on the latency of the reply upon collection of the 24<sup>th</sup> sample and the processing of the 6<sup>th</sup> 'signal' set. The ADC12 conversion latency of the 24<sup>th</sup> sample will be 13 ADC12CLK cycles and 6 MCLK cycles. Synchronous events could extend this latency by as much as 1 ADC12CLK cycle and 1 MCLK cycle (Figure 4.3). To store this sample within the circular buffer and return control to the signal processing routine, another 19 MCLK cycles elapse (within the ADC12 ISR). It was previously determined that 177<sup>18</sup> clock cycles are needed to process the data within the sample buffer. Because this action takes longer than 163 clock cycles, one additional ADC12 conversion ISR

---

<sup>18</sup> Eight less if the MSW of the magnitude result is greater than the MSW of the threshold value.

will invariably cause another 25 clock cycles to elapse before code flow is directed at stopping the receive routine. It takes another 25 clock cycles to shut down power to the receiver and disable the SAR-ADC. The transmit routine then begins. From the start of this routine to the time in which control is given to Timer A to output the PWM, 134 clock cycles plus 1.9 ms elapse. Only 36 of these 134 clock cycles will occur at 8 MHz while the other 98 will occur at an MCLK frequency of 12 MHz. Timer A will begin latching the output of the MCU after 37 additional SMCLK cycles (Figure 4.11). Upon collection of the 24<sup>th</sup> sample, the fixed reply delay ( $T_{FRD}^{24}$ ) of the transponder is analyzed to be ~1.95 ms:

$$T_{FRD}^{24} = \frac{13}{F_{ADC12CLK} = 5MHz} + \frac{288}{F_{MCLK} = 8MHz} + \frac{98}{F_{MCLK} = 12MHz} + \frac{37}{F_{SMCLK} = 12MHz} + 1.9ms$$

This delay will vary because of the variability associated with the MCU converting and storing the 24<sup>th</sup> sample and processing the 6<sup>th</sup> ‘signal’ set:

$$T_{RD}^{24} = T_{FRD}^{24} + T_{VDC}^{24} + T_{VDS}^{24} + T_{VDP}^6 = T_{FRD}^{24} + T_{sync}^1 + T_{sync}^2 - T_{MSW}$$

Where:

$$T_{sync}^1 = \frac{0 \text{ to } 1}{F_{ADC12CLK} = 5MHz}, T_{sync}^2 = \frac{0 \text{ to } 1}{F_{MCLK} = 8MHz}, \text{ and } T_{MSW} = \frac{0 \text{ or } 8}{F_{MCLK} = 8MHz}$$

Variability associated with converting and storing the other 23 samples as well as the variability associated with the other 5 ‘signal’ detections will not affect the reply latency of the transponder. These samples were, again, collected at the sub-sampled rate of 49.08 kHz and processed in non-overlapping sets of four. Including the fixed delay of the first 23 samples collected, the code flow / process latency of a reply decision is analyzed to be ~2.42 ms (+325 ns or -1 μs):

$$T_{RD} = T_{RD}^{24} + T_{FD}^{1 \rightarrow 23} = T_{RD}^{24} + \frac{23}{F_{SS}} = T_{RD}^{24} + \frac{23}{49.08kHz} = T_{RD}^{24} + 468.6 \mu s$$

This process latency represents the minimum (analog) turnaround time associated with the device. That is, if the start of the analog CW burst happened to be captured by the first sample and if the threshold of the detector were set such that processing of this first sample set resulted in

a ‘signal’ decision by the detector, then the turnaround time of the device would equal the reply delay just calculated. Unfortunately, because the analog signal is sampled and the threshold level might have caused the detector to erroneously miss a ‘signal’ decision, the turnaround time latency could extend by another decimation/signal processing cycle:

$$T_{TA} = T_{RD} \rightarrow T_{RD} + \frac{1}{F_{SS}/4} = T_{RD} \rightarrow T_{RD} + 81.5 \mu s$$

Assuming that this variability is random and distributed, the turnaround time of the transponder is analyzed to be **~2.46 ms ( $\pm 41.4 \mu s$ )**. This calculation was verified empirically. By interrogating the transponder at a fixed rate and measuring the (analog) turnaround time of the device using an oscilloscope, the reply latency of the device was observed. Jitter in turnaround time did not exceed the variability calculation. Although this jitter is seen to be a function of the signal processing, it should be noted that the band-limited nature of the front-end (transducer and analog BPF filter alike) ultimately limits temporal resolution of the design. More frequent sampling and signal processing might improve this variability (at the expense of current consumption) but the design is ultimately constrained by the rising edge of the CW burst.

## CHAPTER V

### INITIAL RESULTS AND FUTURE DIRECTIONS

#### **5.1 Proof of Concept**

To demonstrate that the micro-transponder could automatically reply to an interrogation, the prototype was placed within an underwater acoustic test-tank at some distance from a free-running transmitter (Figure 5.1). This transmitter was configured to send a query signal with an acoustic signature that would, in turn, cause the micro-transponder to reply with its encoded message. A Reson TC4034 reference hydrophone was placed between the transmitter and the micro-transponder to objectively observe their acoustic ‘conversation.’ The shielded hydrophone cable was fed into a VP2000 Voltage Preamplifier / Bandpass Filter which provided the observed signal with 50 dB of gain within a 100 kHz – 250 kHz passband. This filtered / amplified signal was then fed into an oscilloscope for visualization and data acquisition. Since the hydrophone was placed within the direct Line-of-Sight (LOS) of the transmitter and the micro-transponder, the oscilloscope would first record the transmitter’s query waveform and a few milliseconds later record the micro-transponder’s coded reply. The goal of this test was to verify that the prototype transponder would reply to a direct LOS interrogation at a predefined repetition rate of once a second. Because sound was reflected within the tank, the query signal was not the only recorded waveform observed. Acoustic multipath from the water’s surface, the bottom, and sides of the pool, were recorded as well. Therefore, this test setup provided a controlled emulation of a highly cluttered underwater environment. Despite these multipath sources, the prototype transponder should provide a single reply for a single interrogation.

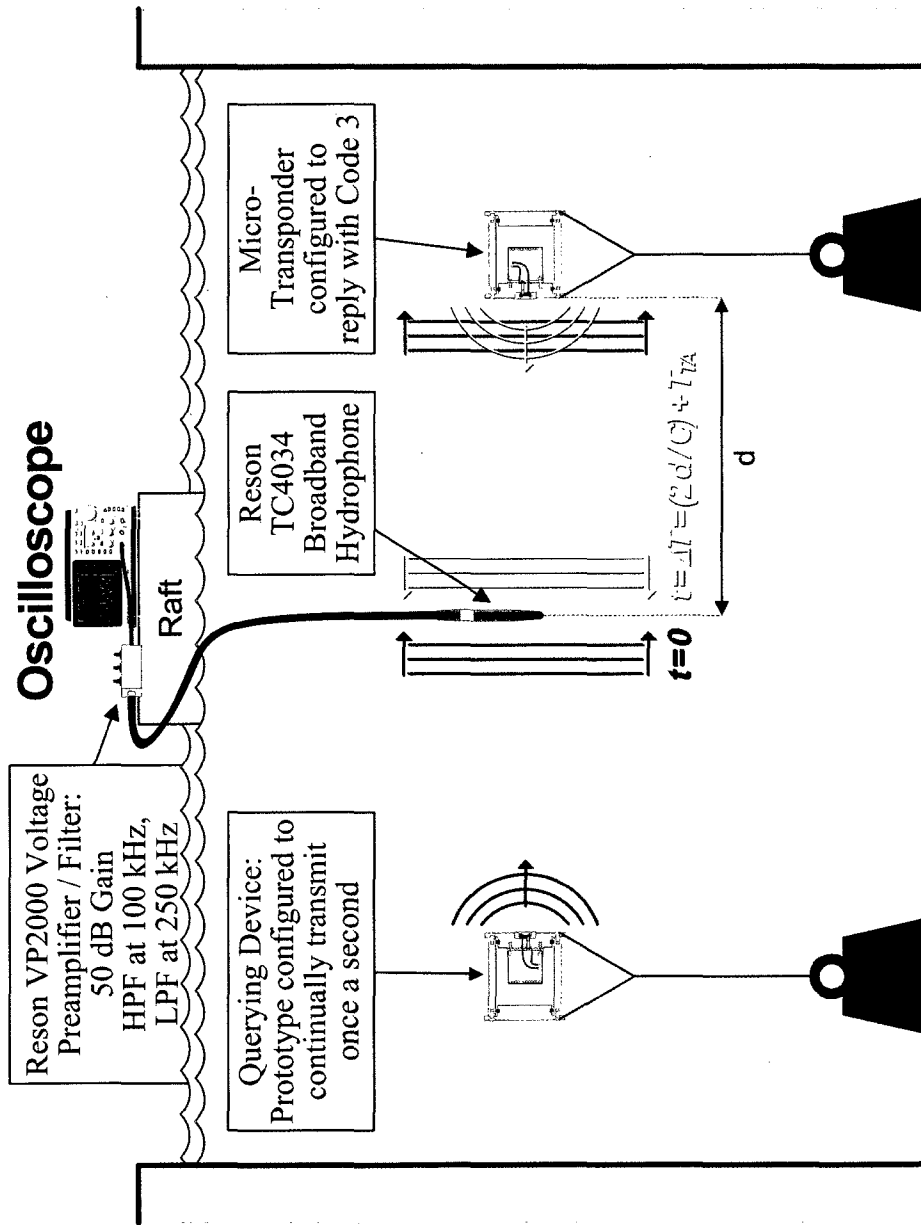


**Figure 5.1: Data Acquisition Methodology for Testing the Functionality of the Transponder**  
 To demonstrate the functionality of the prototype, the test setup shown here was used to validate the design. On the left, a prototype was configured to continually transmit. On the right, the micro-transponder is configured to reply with its coded message. A TC4034 hydrophone was placed between them to record their acoustic conversation.

The transmitter was configured to send 80 cycles of a 160 kHz CW burst once a second. The query waveform is first observed by the TC4034 hydrophone and recorded by an oscilloscope (Figure 5.2). It then travels another  $\sim 4.5$  m to interrogate the micro-transponder.

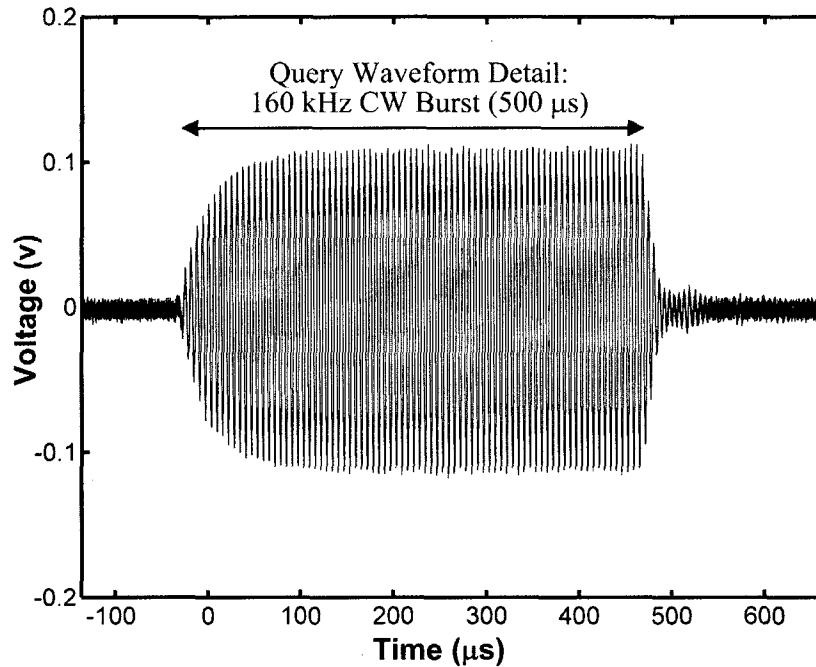


**Figure 5.2: Query Waveform used to Interrogate the Micro-Transponder**

Since the micro-transponder is designed to detect such a signal, it should therefore turnaround and reply with its ‘coded’ message<sup>19</sup>. The oscilloscope triggers off of the query; the time differential between it and the transponder’s reply (as observed by the hydrophone) is the delay of the remaining acoustic path divided by the sound-speed plus the turnaround time of the transponder’s circuitry. Since the hydrophone is placed within the LOS of the transmitter and the transponder, the remaining acoustic path (assuming a uniform sound-speed) is the remaining path of the TX inquiry as it travels toward the prototype transponder (distance ‘d’ in Figure 5.1) and the path of the transponder’s reply as it travels back to the hydrophone (again, distance ‘d’). The micro-transponder’s functionality is validated in Figure 5.3 by showing the receive record with and without the transponder placed in the test tank.

<sup>19</sup> Code 3 used in this test and is characterized by three 160 kHz, 500  $\mu$ s CW Bursts separated by  $\sim 3.8$  ms.

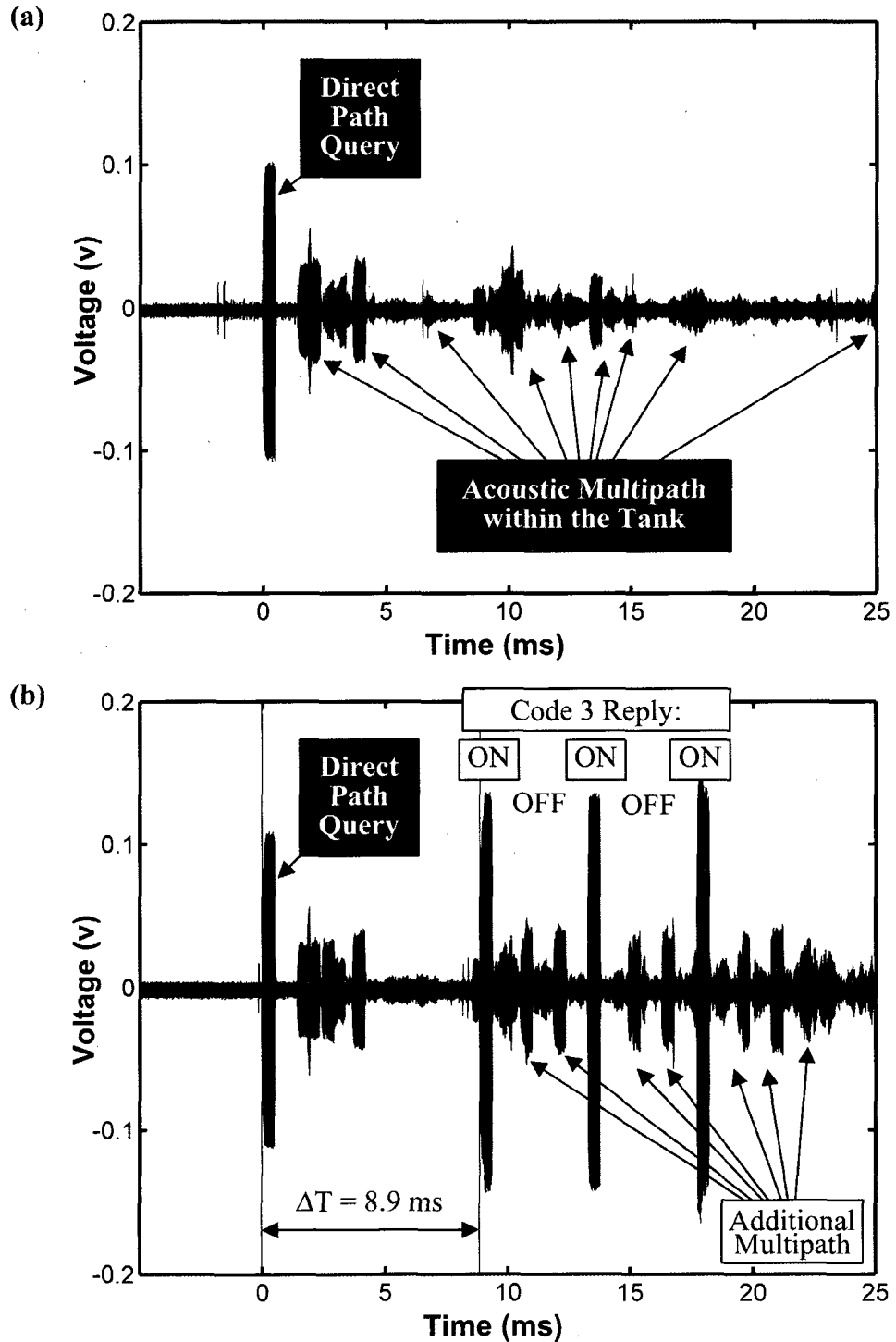


**Figure 5.3: The Acoustic Conversation as Observed by the TC4034 Hydrophone**  
 (a) The waveforms received by the TC4034 when the micro-transponder is absent from the tank. The direct path of the query and its subsequent multipath reflections are observed in this record. (b) When placed in the test tank, the micro-transponder replies with its coded message after receiving and processing ( $T_{TA}$ ) the query. This propagated signal reaches the hydrophone with a delay of 8.9 ms ( $\Delta T$ ).

## **5.2 Performance Specifications of the Prototype Micro-Transponder**

The performance of the micro-transponder prototype is highlighted throughout the text. This section summarizes the key features of its design. The energy consumed by the micro-transponder is a function of the duty cycle with which the transponder responds to interrogations. The RX and TX power-demands of the sub-systems of the design are analyzed throughout the text and summarized in the Table 5.1.

**Table 5.1: Power-Demand of the Transponder’s Sub-Systems for TX and RX Modes**  
When transmitting, the micro-transponder demands ~1.2 W to generate a coded reply at a source level of 167 dB re 1  $\mu$ Pa at 1 m. When receiving, the micro-transponder demands 6.2 mW to identify an acoustic interrogation.

	Power-Demand (mW)	
	Transmit Mode	Receive Mode
LDO $V_{REF}$	0.003	0.051
Analog Receiver	0.000	1.630
Analog Transmitter	1221.254	0.022
Power Supply	0.030	0.030
Microcontroller	5.100	4.500
Total Power-Demand	<b>1226.387</b>	<b>6.233</b>

1680 mWh stored within the micro-transponder’s battery provides energy for its RX and TX operations. The maximum lifespan of the micro-transponder (always receiveing) is 11.2 days. If it were continually interrogated at a 0.15%, duty cycle, the micro-transponder’s average power-demand increases to 8.06 mW and its lifespan decreases to 8.7 days. The other attributes of the design are summarized as:

- Size: L: 50 mm  $\times$  W: 37 mm  $\times$  H: 10 mm
- Weight: 43.7 g (in air)
- Acoustic Operating Band: 155 – 165 kHz
- Source Level: 167 dB re 1  $\mu$ Pa at 1 m
- Turnaround Time (Uncertainty):  $T_{TA} = 2.46$  ms ( $\pm 0.04$  ms)
- Firmware Updatable



### **5.3 Future Directions**

The ultimate goal of this project was to develop technology that could be used by researchers. To this end, improvement in both the function and the form of the prototype micro-transponder must be made. Changes to the existing design should better suit its use in field tests. The following physical (or hardware) improvements aim at packaging the micro-transponder and deploying it in the field:

1. Integrating an 'on' / 'off' switch that will enable efficient top-side deployment of the transponder.
2. Removing test and development connectors from the PCB design itself.
3. Integrating a watertight JTAG connector that will enable data to be uploaded and downloaded before and after its deployment.
4. Encapsulating the entire tag in urethane will minimize the size of the prototype tag.

The following software updates intend to improve the dynamic performance of the micro-transponder when deployed:

1. Extending the length and/or weighting of the I/Q FIR BPF will significantly improve out-of-band noise suppression.
2. Implementing adaptive control of the detector's threshold level will improve the ability of a transponder to distinguish signal from noise as the tag moves about the water column.
3. Implementing an intelligent selection of an analog RX 'tap' based on peak signal levels calculated by the MCU.
4. Implementing an encoding scheme for uniquely identify multiple micro-transponders.
5. Implementing a polling routine will extend the effective deployment duration of the tag itself. By putting the transponder into a low-power (sleep) state, the average power will proportionally decrease by the duty cycle with which it "polls" or "receives" signals within the water column.

## **5.4 Final Conclusions**

Tank test results validate the functionality of the prototype. Because its on-axis operation was evaluated and directionality measured, the performance of the micro-transponder in other orientations can be predicted. These results show how the micro-transponder might be used to uniquely identify targets within the water column. With appropriate packaging, this prototype may be used in various underwater tracking applications, including unobtrusively tracking marine mammals. The micro-transponder's transmit and receive circuitry have been scaled to operate over a maximum range of 500 m and should acoustically identify the positions of seals as they dive into a school of fish. Such data would allow researchers to interpolate the dive track of a species in a spatio-temporal scale appropriate for identifying behavioral characteristics of the animal itself. Likewise, these data could be correlated with other analyses including, but not limited to, prey patch size and density, water salinity, water temperature, acoustic sound-speed, and water flow.

Because the micro-transponder's functionality is largely hardware independent, firmware updates could expand the capabilities of this technology. The temperature sensor within the microcontroller itself could be polled and its data encoded in the micro-transponder's reply. Similarly, by integrating pressure and conductivity sensors into the design, the sound-speed at the transponder's location could be encoded and telemetered to querying sources. Internal memory within the microcontroller itself could be utilized for data logging. This data might be saved and transmitted at times convenient for researchers to collect such data. Additionally, in its current form, the micro-transponder could be configured to be an echo-sounder. By processing the time of arrival differentials of the transmitted signals, the transponder (in echo-sounder mode) could approximate distance to other targets, such as the sea surface. Depth data could be collected and logged accordingly, encoded, and transmitted to a querying source. Through additional improvement of the existing design, further advancements in underwater technology could potentially be achieved.

## LIST OF REFERENCES

- Airmar. 2000. "Sensor Design Fundamentals." Airmar Technology Corp. #17-1205.
- Arnold, G. A., and H. Dewar. 2001. "Electronic tags in marine fisheries research: a 30-year perspective." Pages 7-64 in J. R. Sibert and J. L. Nielsen, editors. Electronic Tagging and Tracking in Marine Fisheries. Kluwer. Academic Publishers, Dordrecht, The Netherlands.
- Bierl, Lutz. January 2000. "MSP430 Family Mixed-Signal Microcontroller Application Reports." SLAA024. Texas Instruments Incorporated. January 2000.
- Carter, Bruce. August 2002. "Chapter 17: Circuit Board Layout Techniques." Op-Amps For Everyone – Design Reference. Texas Instruments. Advanced Analog Products. SLOD006B.
- Channel Industries. "Piezoelectric Ceramic [Product Catalog]." Channel Industries, Inc. [http://www.channelindustries.com/includes/chan\\_cat.pdf](http://www.channelindustries.com/includes/chan_cat.pdf).
- Chase Jr., Jay V. February 1985. "A Tracking and Telemetry System for Severe Multipath Acoustic Channels." *The Journal of the Acoustical Society of America*, Volume 77, Issue 2.
- Davies, John H. 2008. MSP430 Microcontroller Basics. Elsevier LTD.
- Davis, R. W., Hagey, W., and Horing, M. 2004. "Monitoring the behavior and multi-dimensional movements of Weddell seals using animal-borne video and data recorder." *Mem. Natl Inst. Polar Res., Spec. Issue 58*. 150-156.
- Davis, R. W., L. A. Fuiman, T. M. Williams, M. Horning, and W. Hagey. 2003 "Classification of Weddell seal dives based on 3-dimensional movements and video-recorded observations." *Marine Ecology Progress Series*. 2003. 264:109-122.
- de Moustier, Christian. January 26, 2005. "Environmental Acoustics Air – Water II." OE / EE 7-895 Special Topics. Class notes.
- Jung, Walter G. July 2002. Op Amp Applications. "Practical Problems in Filter Implementation." Analog Devices Inc. Section 5-7.
- Kugelstadt, Thomas. February 2000. "The operation of the SAR-ADC based on charge redistribution." *Analog Applications Journal*. SLYT176. Texas Instruments Inc. 10-12.
- Linear Technology Corporation. 2007. "LT3572: Dual Full-Bridge Piezo Driver with 900mA Boost Converter." LT0408 REV A. <http://cds.linear.com/docs/Datasheet/3572fa.pdf>.
- Lyons, Richard G. 2004. Understanding Digital Signal Processing. Second Edition. Prentice Hall Professional Technical Reference. Pearson Education, Inc.
- Mitson, R.B and Storeton-West, T.J. November 1971. "A Transponding Acoustic Fish Tag." *Radio Electronic Engineering*, vol. 41, no. 11. 483-489.

- Niknegad, A. M. 2008. "Review of Resonance and Tuned Amplifiers." EECS 142. Lecture 5 Notes. UC, Berkeley. <http://rfic.eecs.berkeley.edu/142/pdf/lect5.pdf>.
- Panasonic. January 2000. "Panasonic Lithium Batteries Handbook 2000." Matsushita Battery Industrial Co., Ltd. [www.battery-kutter.de/assets/pdf/panasonic/lithium.pdf](http://www.battery-kutter.de/assets/pdf/panasonic/lithium.pdf).
- Quiring, Keith. 2006. "MSP430 Software Coding Techniques." MSP 430 Application Report SLAA294A. Texas Instruments Incorporated.
- Richardson, W.J., Greene, C.R., Malme, C.I., Thomson, D.H., 1995. Marine Mammals and Noise. Academic Press. 212.
- Schusterman, R. J., Kastak, D., Levenson, D., Reichmuth, C. J., and Southall, B. L. 2000. "Why pinnipeds don't echolocate." J. Acoust. Soc. Am. 107(4), 2256-2264.
- Sedra, Adel S. and Smith, Kenneth C. 1998. Microelectronic Circuits. Fourth Edition. Oxford University Press.
- Texas Instruments Incorporated. 2008. "MSP430x23x, MSP430x24x(1), MSP430x2410 Mixed Signal Microcontroller." SLAS547B.
- Texas Instruments Incorporated. 2008. "MSP430x2xx Family – User's Guide." SLAU144E.
- Texas Instruments Incorporated. May 2001. "Ultralow-Power 50-mA Low-Dropout Linear Regulators." SLVS210D. <http://focus.ti.com/lit/ds/symlink/tps77001.pdf>.
- University of Rhode Island. 2009. "Animals and Sound in the Sea: Sound Production and Reception." <http://www.dosits.org/animals/produce/2f.htm>.
- Wilson, Oscar Bryan. 1988. Introduction to Theory and Design of Sonar Transducers. Peninsula Publishing.

## **APPENDICES**

## APPENDIX A

### THE PROTOTYPE MICRO-TRANSPONDER

#### A.1 Potted Transducer Interfaced with the PCB Design

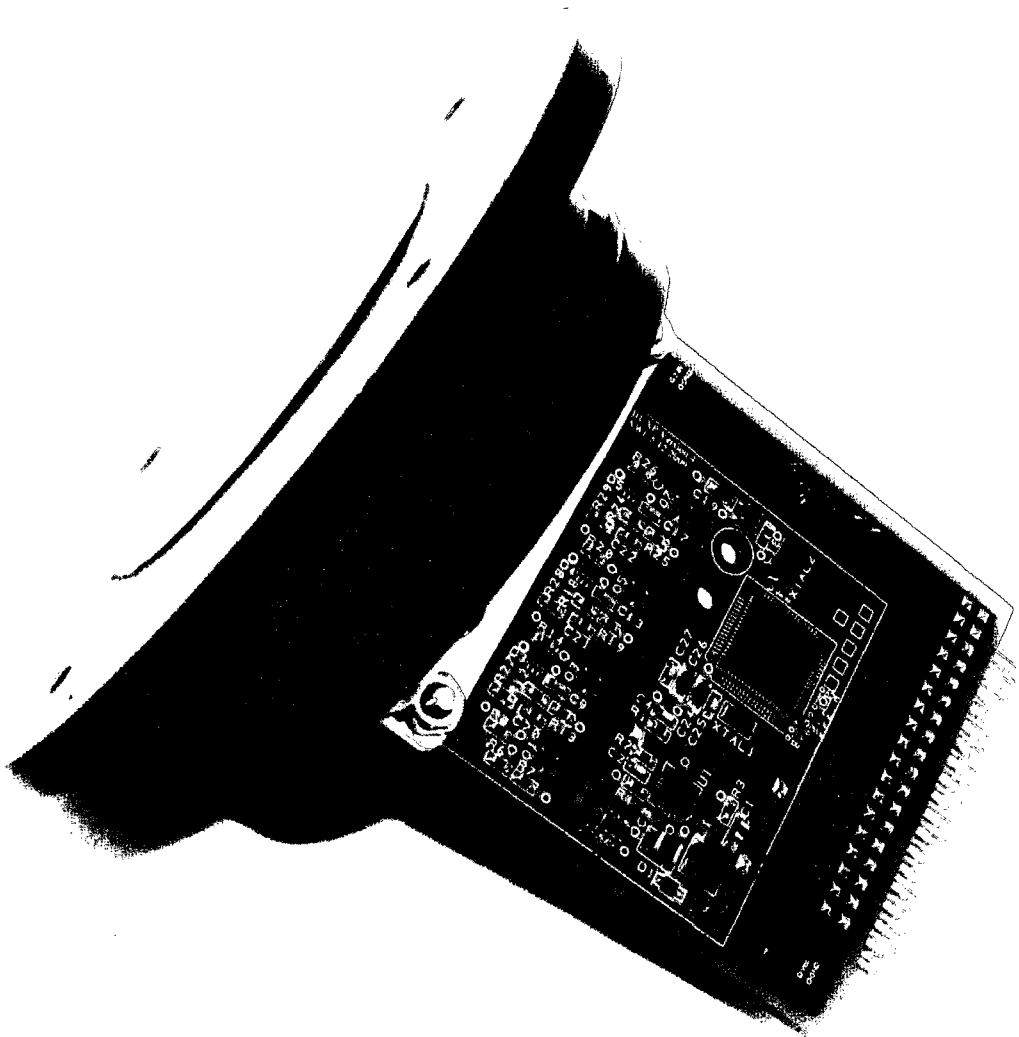


**Figure A.1: Prototype Transponder (PCB Top Shown)**

The prototype micro-transponder circuitry is interfaced with the transducer assembly, which was mounted and potted within a cavity of a pressure-housing lid. The lid was machined by Paul Lavoie and also includes an o-ring seal, aluminum mount for the PCB, and the two leads that provide electrical continuity between the piezoelectric ceramic and their respective connectors on the PCB.

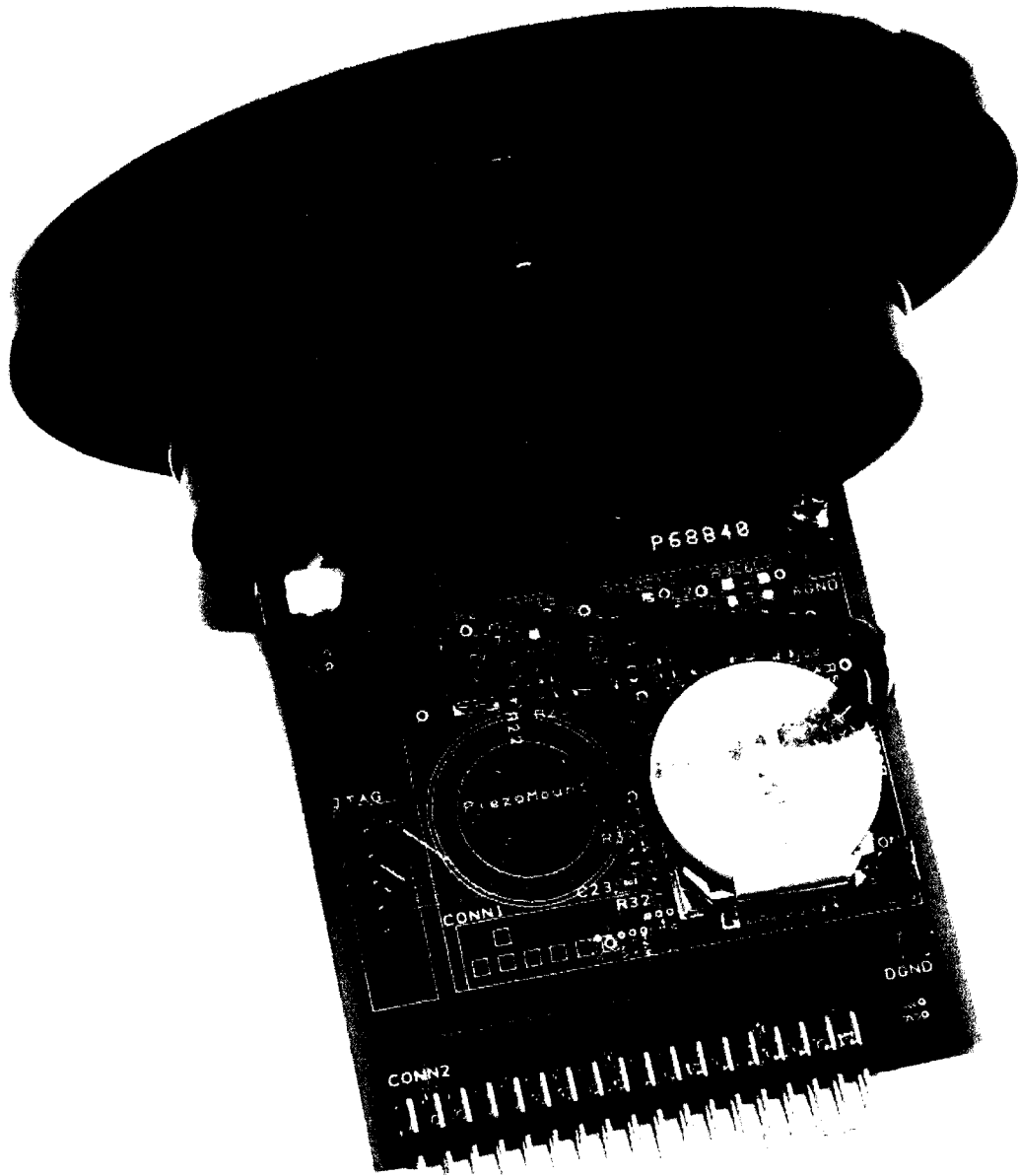


**Figure A.2: Prototype Transponder (PCB Bottom Shown)**

For test and development, the transducer assembly was integrated within the pressure-housing lid rather than being mounted on the PCB (as seen by the omission of the 'PiezoMount'). The black lead is connected to a #4-40 screw, which extends through the lid and holds the brass mount of the transducer assembly in place. The mount is interfaced to the negative electrode of the piezoelectric transducer and thus the black lead is connected to the negative-transducer net-connection on the PCB. The red lead is fed through the lid (via a hole) and soldered directly to the positive electrode of the piezoelectric transducer. Epoxy provided strain relief for this lead and was also fed into this hole. This lead is connected to the positive-transducer net-connection on the PCB.

## A.2 The Pressure Housing for Prototype Development

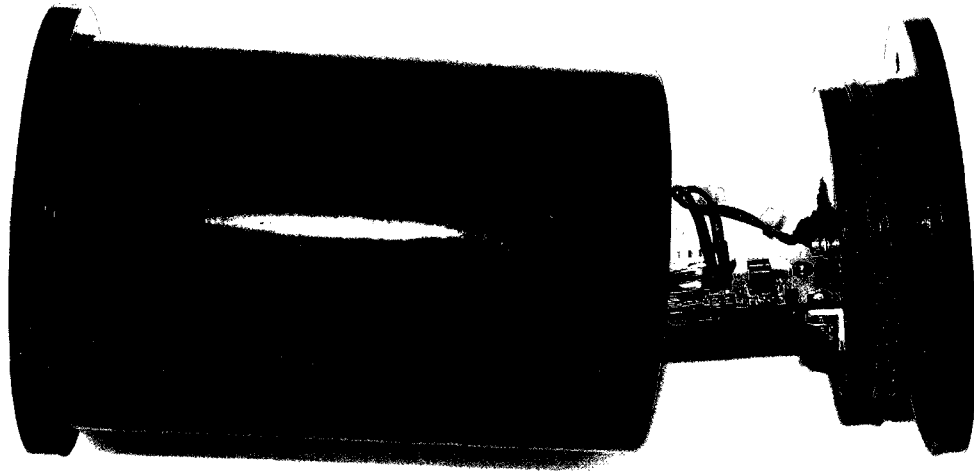


**Figure A.3: Pressure Housing (Side View)**

To test and develop the prototype design, the transducer was potted within the lid of a pressure housing that enabled the rest of the circuit to be mounted within.



**Figure A.4: Assembled Pressure Housing**

The assembled pressure housing in this figure shows how the prototype circuit was encased.



## APPENDIX B

### THE TRANSDUCER ASSEMBLY

#### B.1 Piezoelectric Ceramic



**Figure B.1: Piezoelectric Ceramic with Soldered Electrode**

A #24 AWG (red) lead is soldered directly to the positive electrode of the piezoelectric ceramic.

#### B.2 Construction of the Assembly

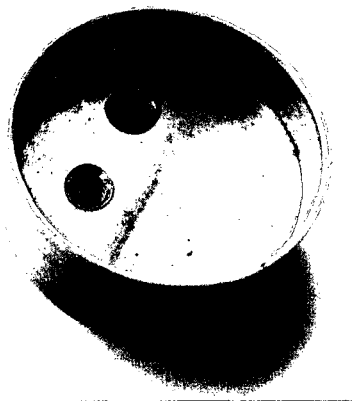


**Figure B.2: Machined Brass Mount used to House the Transducer Assembly**

A brass mount, machined by Paul Lavoie, houses the entire assembly and provides a through-hole for the positive lead and a screw-hole for mounting.

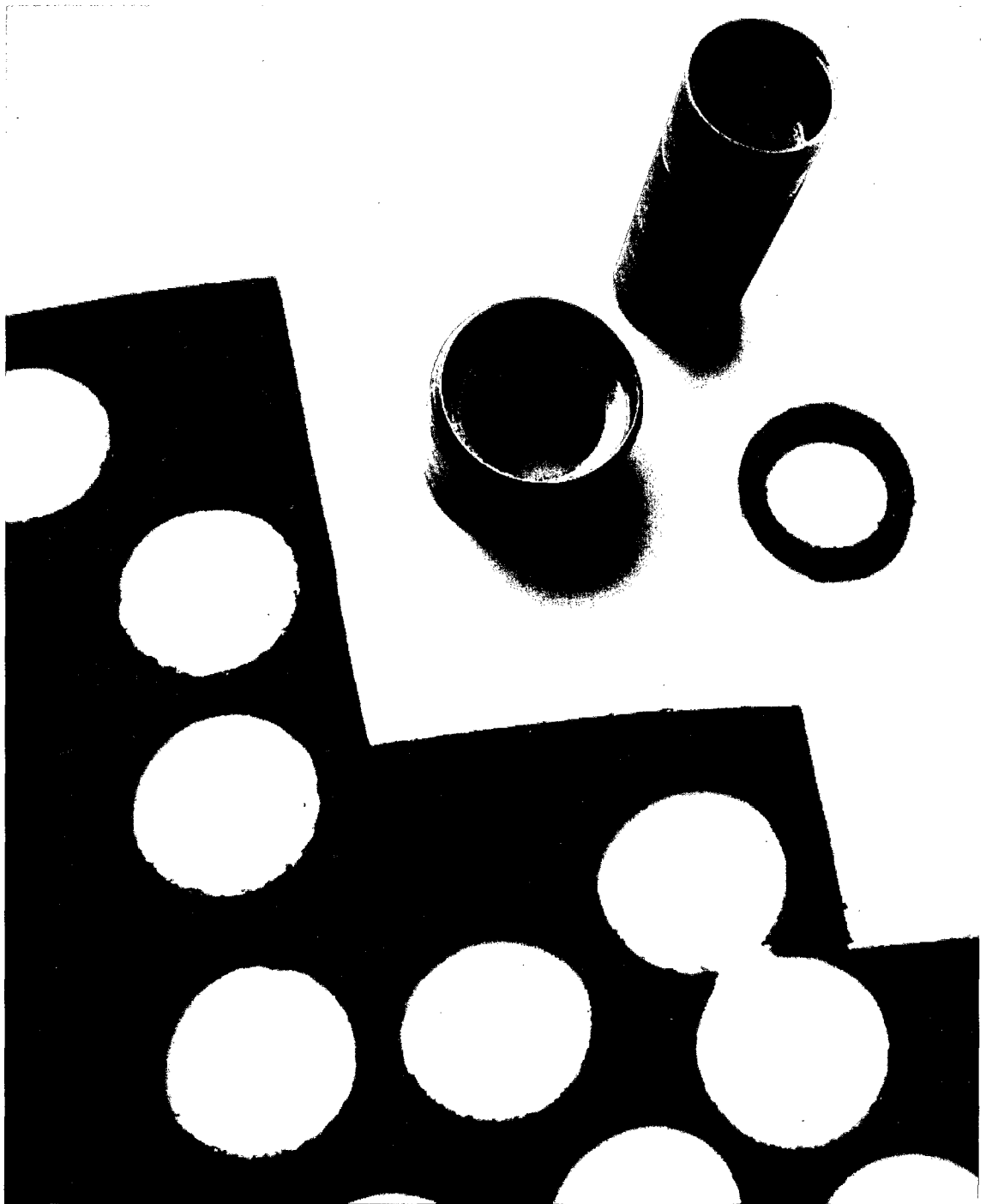


**Figure B.3: Punch Used to Cut 1/16" Corprene Sheet for the Transducer Assembly**  
A corprene punch tool, machined by Paul Lavoie, was used to cut both the disks and annuluses of corprene. These disks and annuluses were used within the transducer assembly for acoustic absorption and provided a backing the piezoelectric ceramic.



**Figure B.4: The Brass Mount and The Corprene Sections Surrounding the Ceramic**  
The disks and annuluses of corprene surround the internal faces of the piezoelectric ceramic. The red plus sign indicates the polarity of the ceramic.

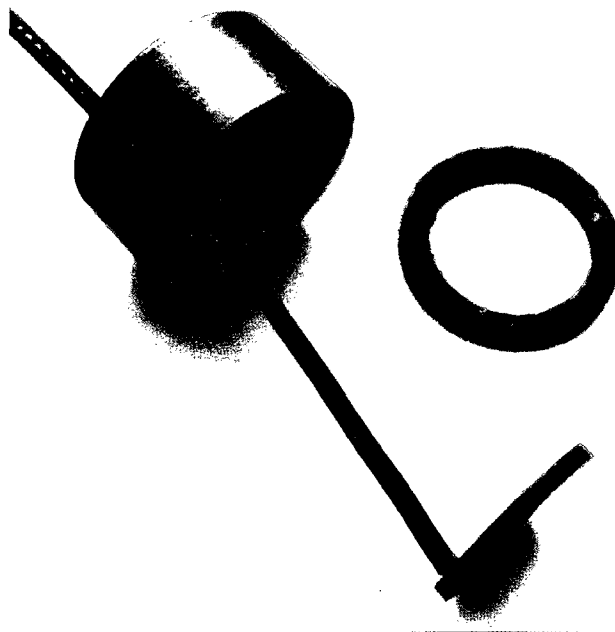


**Figure B.5: Assembling the Transducer**  
The soldered ceramic (positive electrode) is fed through and sits on the corprene backing that lines the brass mount as seen in this figure.

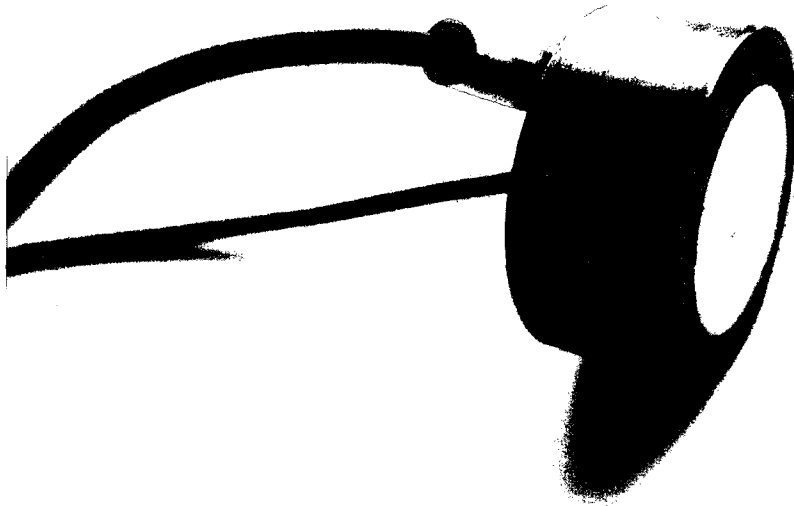


**Figure B.6: Assembled Transducer (Front View)**

The transducer assembly with the outward (projecting) face of the piezoelectric ceramic is shown in this figure.

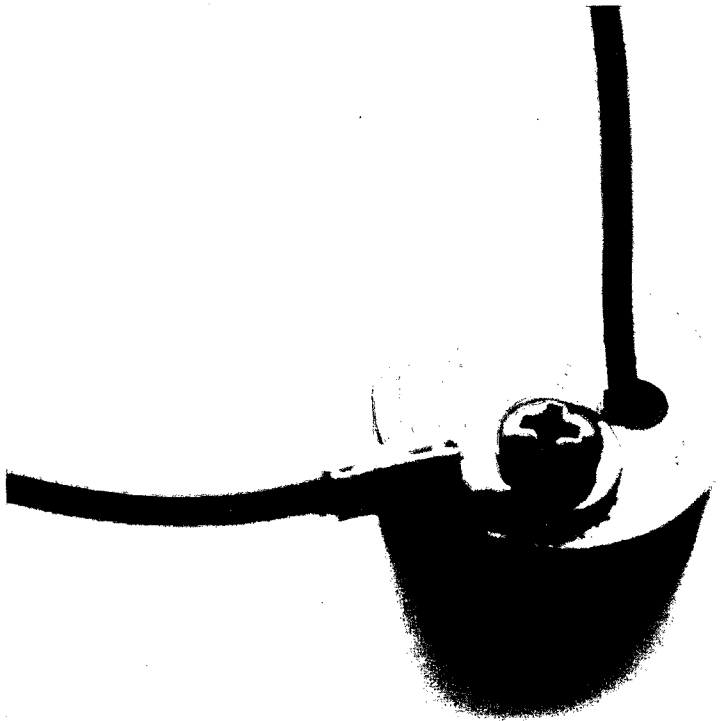


**Figure B.7: Assembled Transducer (Back View)**

The backside of the transducer assembly is shown in this figure. The red lead is fed through the transducer assembly while the black lead is crimped to a connector that is held in place between a washer and a #4-40 screw.

### B.3 Potting

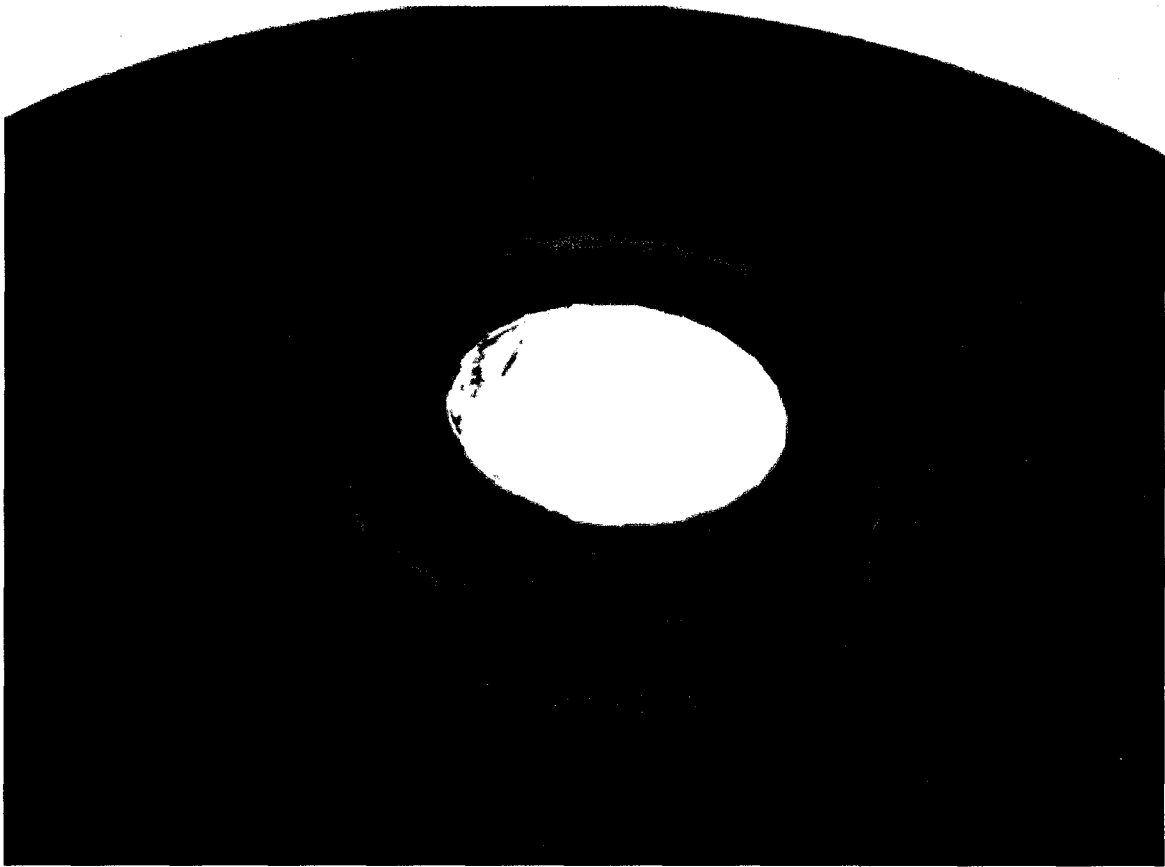


**Figure B.8: Transducer Assembly Mounted to Pressure-Housing Lid (Pre-Potting)**

A cavity within this lid, machined by Paul Lavoie, provided a mold for the urethane potting material. The surfaces of this cavity were roughened for better adhesion of the potting material. The surface area of the cavity was also extended, for the same reason, and prompted the machining of the unique cavity-pattern as seen within this figure. Conductive foil was adhered to and provided electrical continuity between the negative-potential electrode of the ceramic and the brass mount.

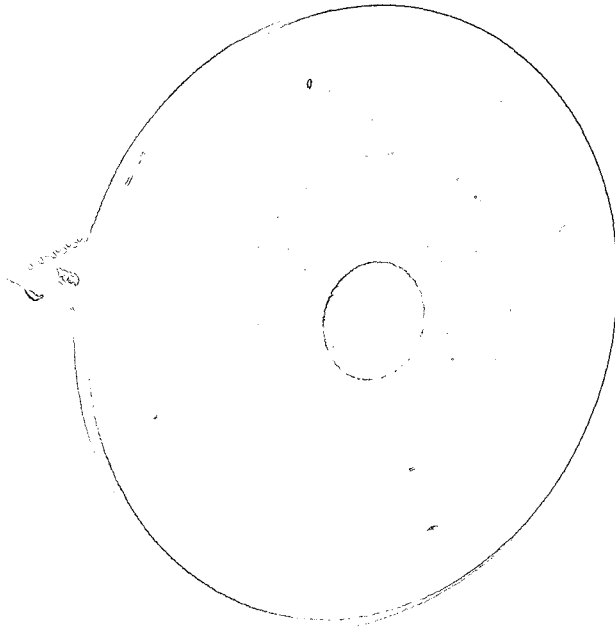


**Figure B.9: Potted Transducer Assembly within Pressure-Housing Lid**  
The outward-projecting face of the potted transducer is shown within this figure.

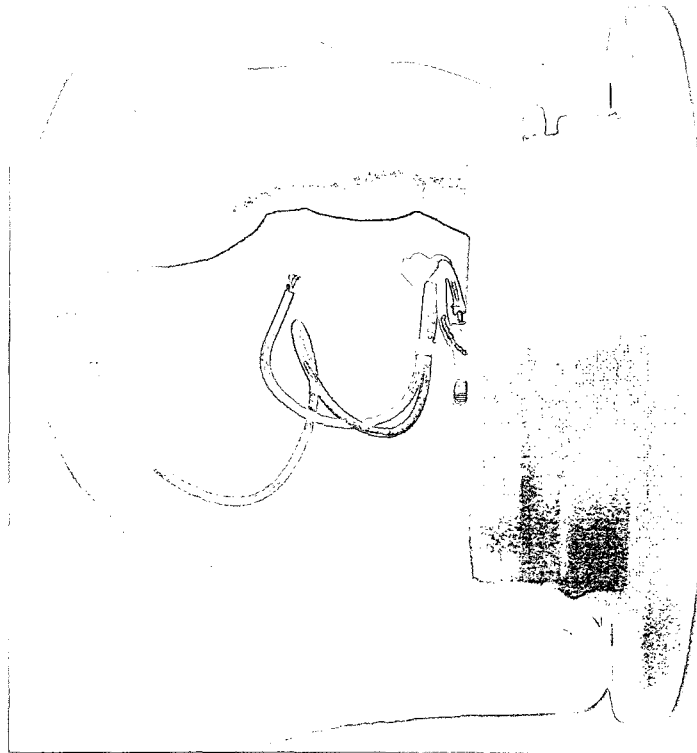


**Figure B.10: Side View of Pressure-Housing Lid**  
The side view of the pressure-housing lid shows how the leads of the transducer assembly protrude through and sit within the pressure housing.

## APPENDIX C

### CONFIGURATION OF CALIBRATION EXPERIMENTS

#### C.1 TVR / Beam Pattern Measurement Test Setup

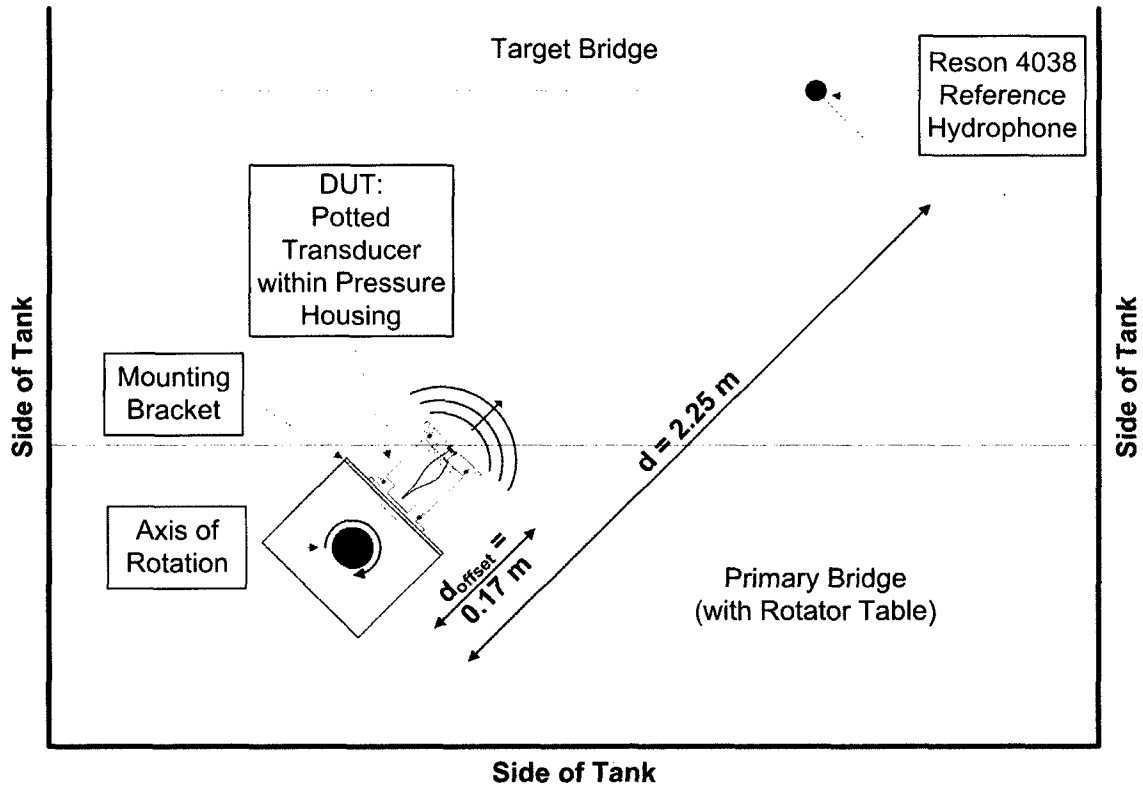


**Figure C.1: Overhead View of the Calibration Setup at the Klein Test Tank**

The test setup, shown in this figure, was used to make Transmit Voltage Response (TVR) and directivity measurements of the transducer designed and built for this project. A Reson 4038 reference hydrophone was used as a calibrated receiver. The beam pattern measurement was corrected for parallax angles and transmission loss differences because the transducer was mounted at an offset distance ( $d_{\text{offset}}$ ) from axis of the rotational pole.

## C.2 Data Acquisition Methodology and Self-Reciprocity Test Setup

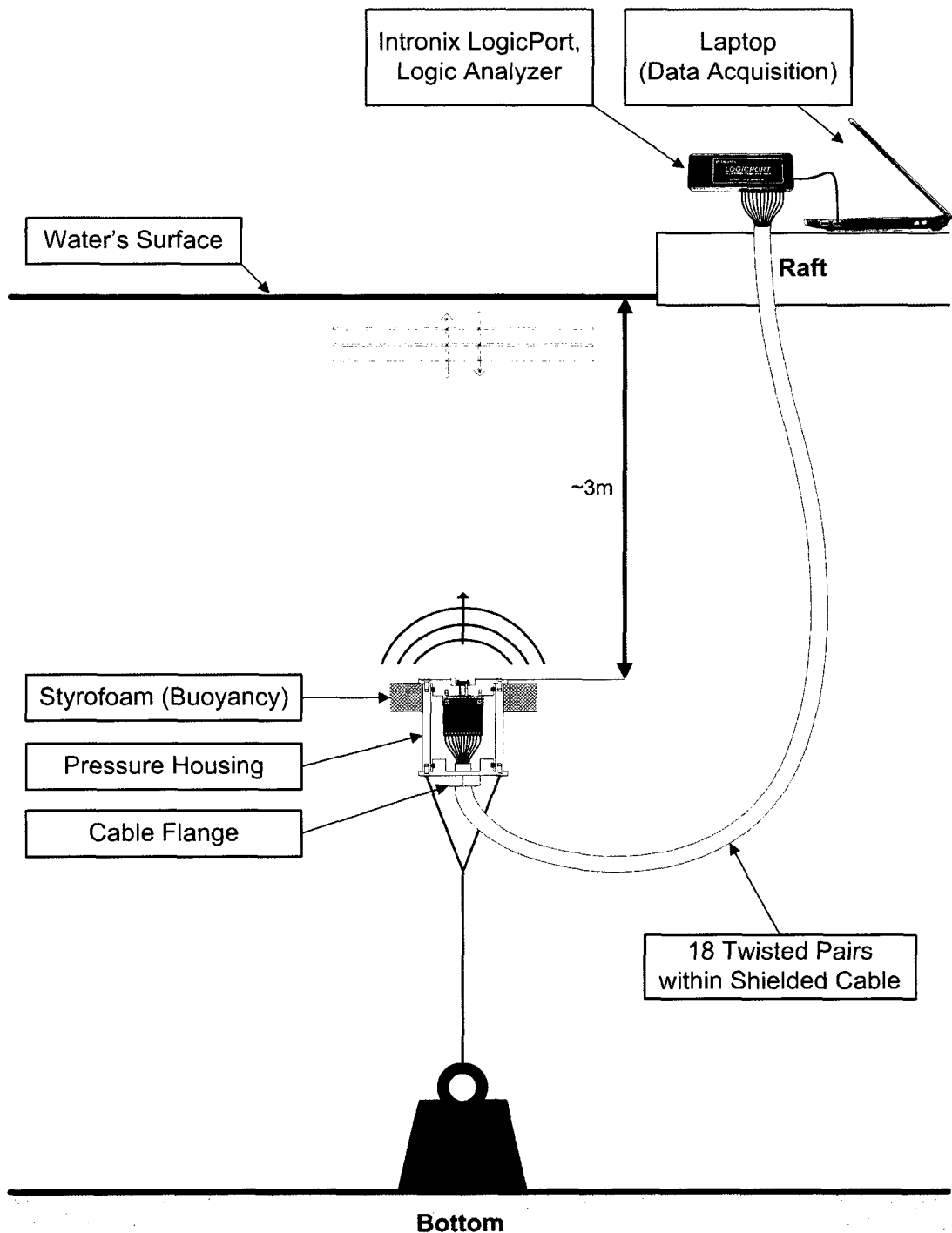


**Figure C.2: Side View of Tank Test Setup used to collect Sampled Waveforms**

To collect digitized RX waveforms within the test tank, the prototype circuitry was programmed to transmit a free-running CW burst once a second and wait for the surface reflections to travel back. The RX signals were then converted into samples and output onto the cable connecting the PCB to the top-side data acquisition software.



## APPENDIX D

### THE MSP430F249 MICROCONTROLLER

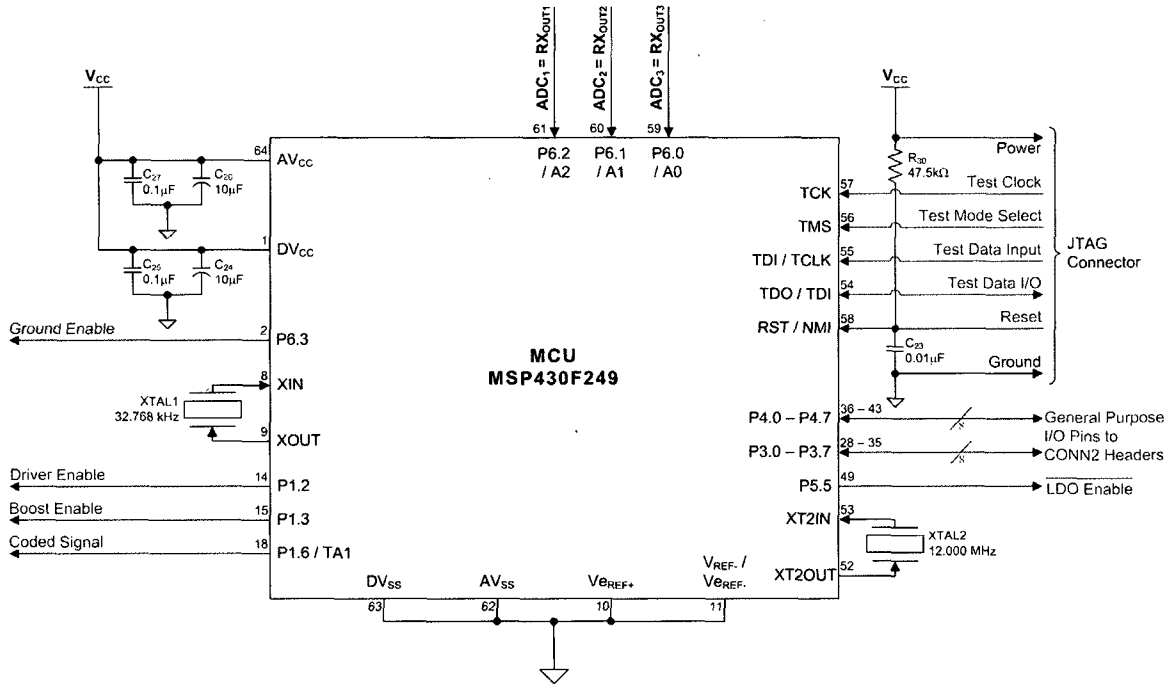


**Figure D.1: Circuit Topology of the Microcontroller**

The MCU is interfaced to the digital and analog sub-systems of the design. These connections are annotated by the green and blue lines, respectively. The digital connections control the RX and TX functions of the design. ‘GND\_EN’ controls the gate of the Grounding FET used to switch between RX and TX modes. ‘LDO\_OFF’ enables power supplied to the analog RX circuitry. ‘BOOST\_EN’ and ‘DRVN\_EN’ control the boost converter and full-bridge driver of the transmit power-amplifier, respectively. Additionally, the MCU generates the modulated code-signal that is amplified by the TX-amplifier that then drives the transducer. Received signals are amplified and filtered by the analog receiver and interfaced with the MCU through the three ADC inputs (ADC<sub>1</sub>→ADC<sub>3</sub>). These input ‘taps’ correspond to increasing gain realized by cascaded sections of analog receiver. The discrete components that support the MCU include power-supply bypass capacitors (C<sub>24</sub>→C<sub>28</sub>), a low frequency crystal (XTAL1), a pull-up resistor (R<sub>30</sub>), and a shunt capacitor (C<sub>23</sub>). Bypass capacitors are required for regulating both the digital and the analog supply voltages of the MCU. A 32.768 kHz low frequency crystal is used for timing of the MCU when powered down in LMP0. A JTAG connector is used to communicate with the MCU and allows firmware to be uploaded. It is interfaced with the MCU using pins 54-58. The MCU is reset by applying active-low to pin 58. A pull-up resistor and shunt capacitor are used to regulate this pin high. Headers on the PCB connect several I/O pins to the MCU for test and development.

## APPENDIX E

### PRINTED CIRCUIT BOARD LAYOUT

#### E.1 Component Placement

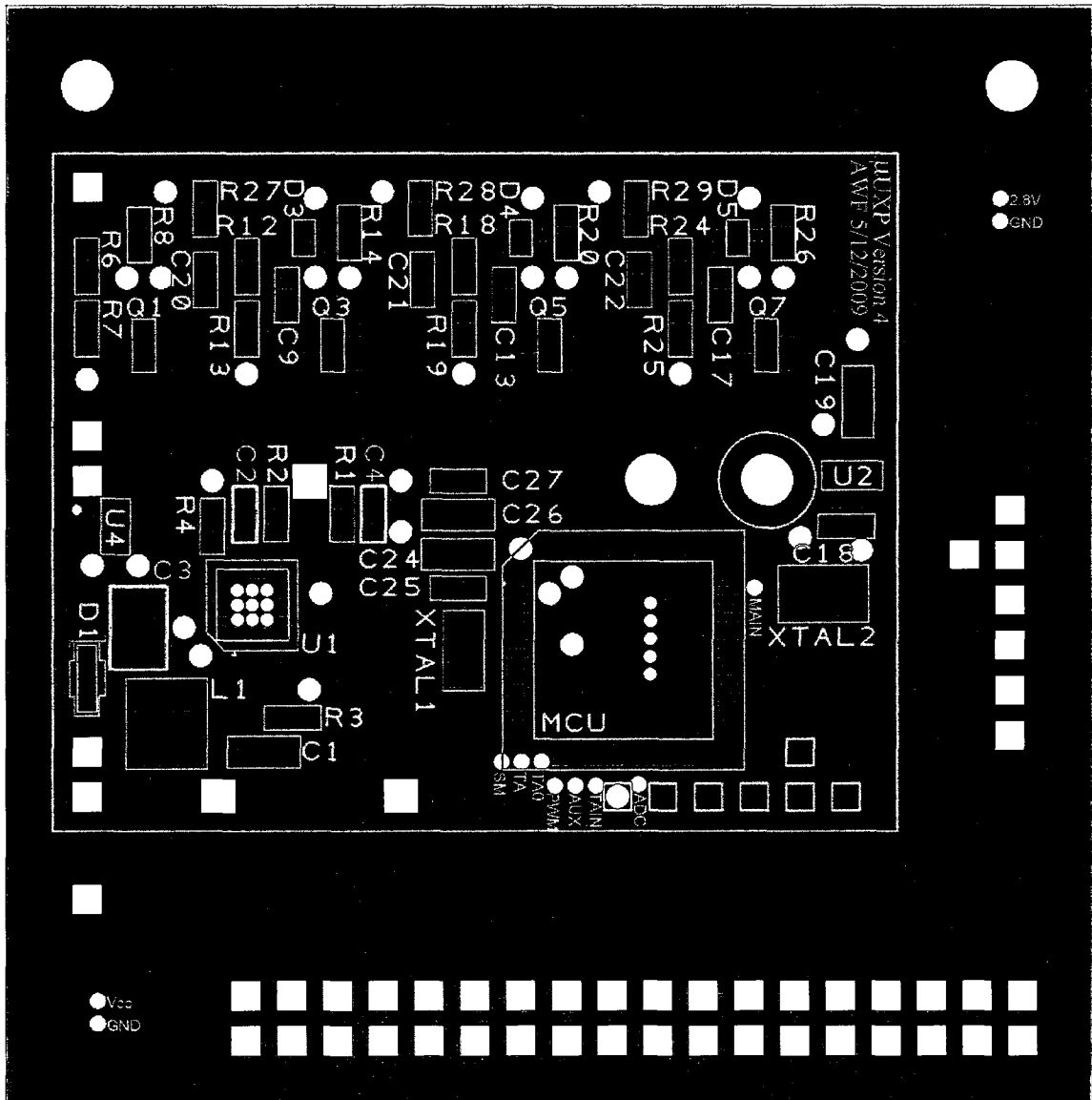
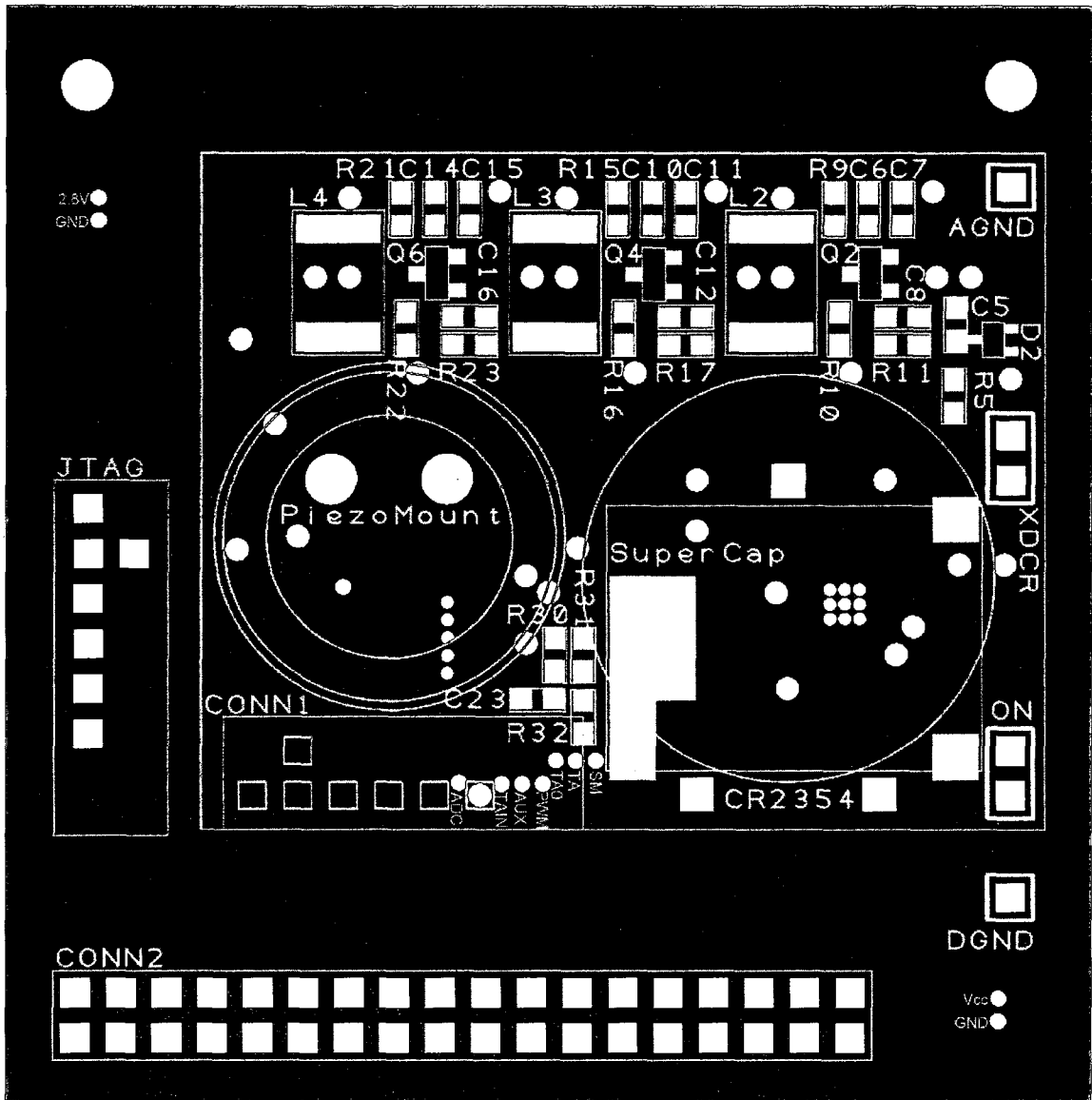
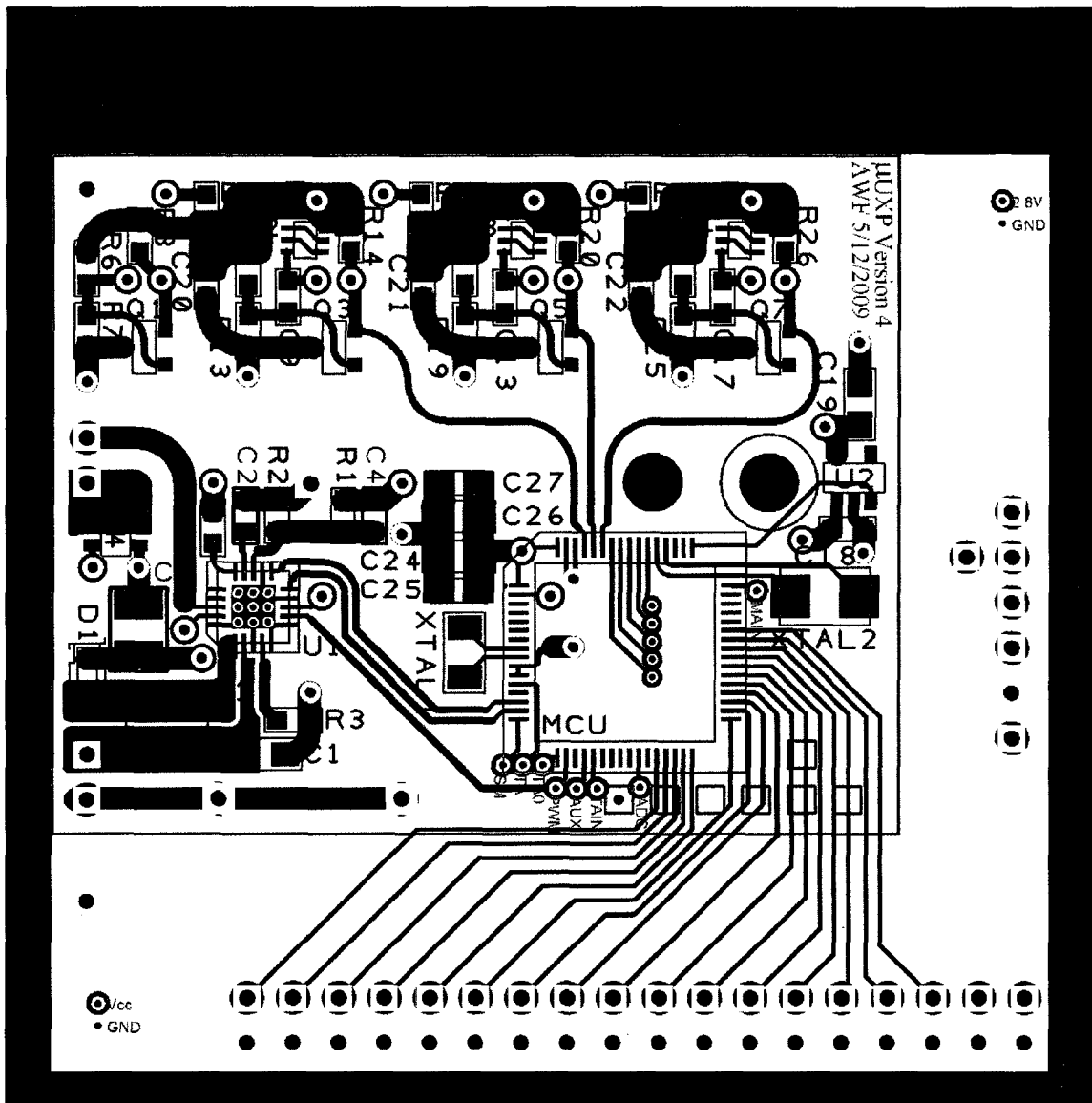


Figure E.1: Reference Designation of Discretes Placed on the Top of the PCB  
This figure shows the locations of the circuit elements that sit on the top side of the PCB. Their reference designations are shown in blue and silkscreened as such when fabricated. The pads of these components are shown in orange and solder mask is understood to be placed on locations other than these pads and the yellow areas which correspond to vias.



**Figure E.2: Reference Designation of Discretely Placed on the Bottom of the PCB**  
 Inverted in CAD to afford a “bottom-up” perspective, this figure shows the locations of the circuit elements that sit on the bottom of the PCB. Their reference designations are shown in blue and silkscreened as such when fabricated. The pads of these components are shown in orange and solder mask is understood to be placed on locations other than these pads and the yellow areas corresponding to vias.

## E.2 Four Layer PCB Design



**Figure E.3: Top Two Layers of the PCB Design**

This figure shows the interconnections of the circuit elements that sit on the top side of the PCB. Their reference designations are shown in blue and silkscreened as such when fabricated. The pads of these components are shown in dark red while the connections are routed out of the top-layer of copper and annotated in light red. The second layer of copper is shown in green. This layer represents ground for the design and is the return path for the signals sent on the top layer. Again, the vias are outlined in yellow.

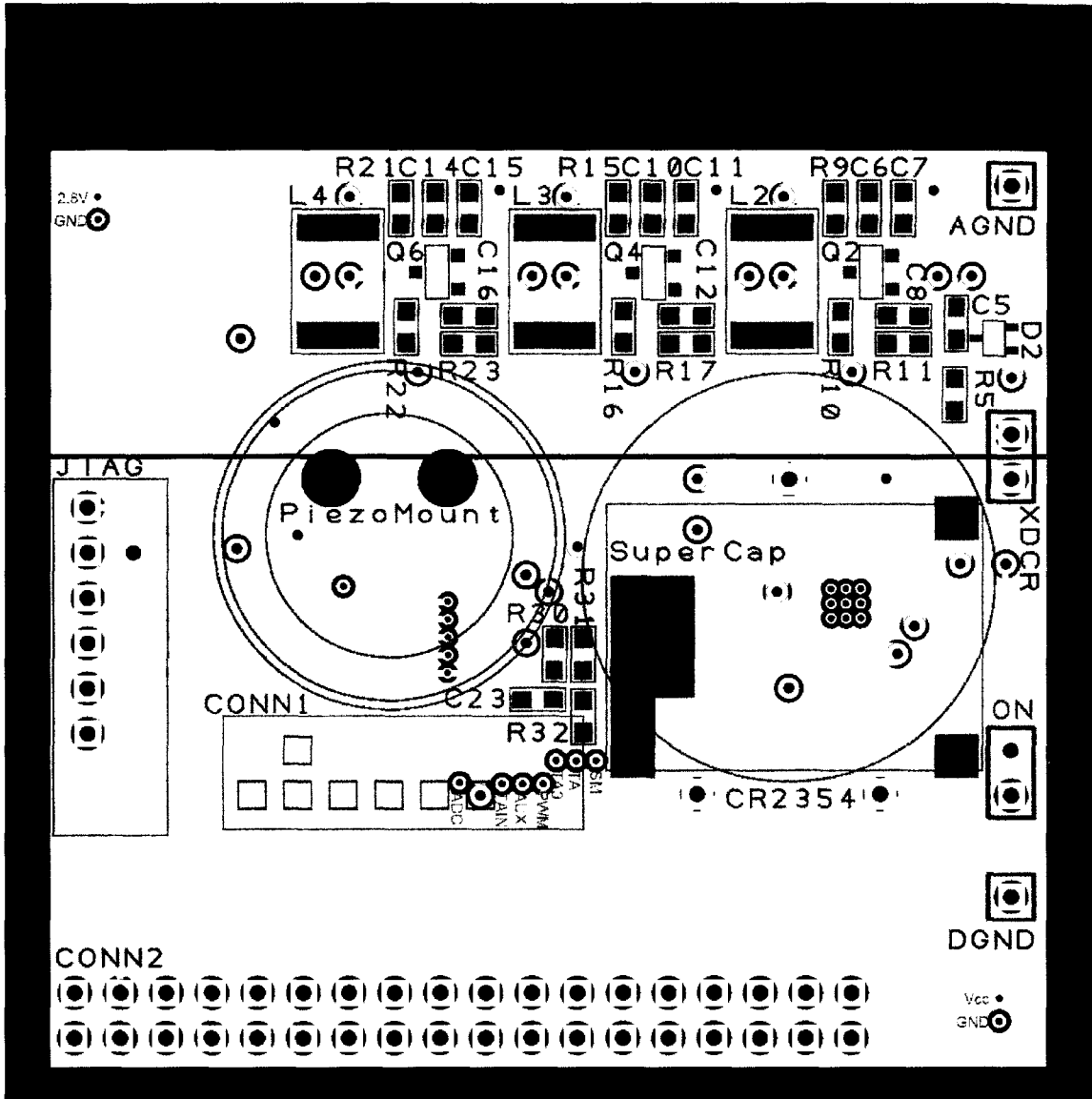


**Figure E.4: Bottom Two Layers of the PCB Design**

Inverted in CAD to afford a “bottom-up” perspective, this figure shows the interconnections of the circuit elements that sit on the bottom of the PCB. Their reference designations are shown in dark blue and silkscreened as such when fabricated. The pads of these components are shown in dark orange while the connections are routed out of the bottom-layer of copper and annotated in light orange. The third layer of copper is shown in light blue. This layer is split and represents  $V_{CC}$  and  $V_{REF}$  in the design and is the return path for the signals sent on the bottom (4<sup>th</sup>) layer. Again, the vias are outlined in yellow.

### E.3 Fabricated PCB

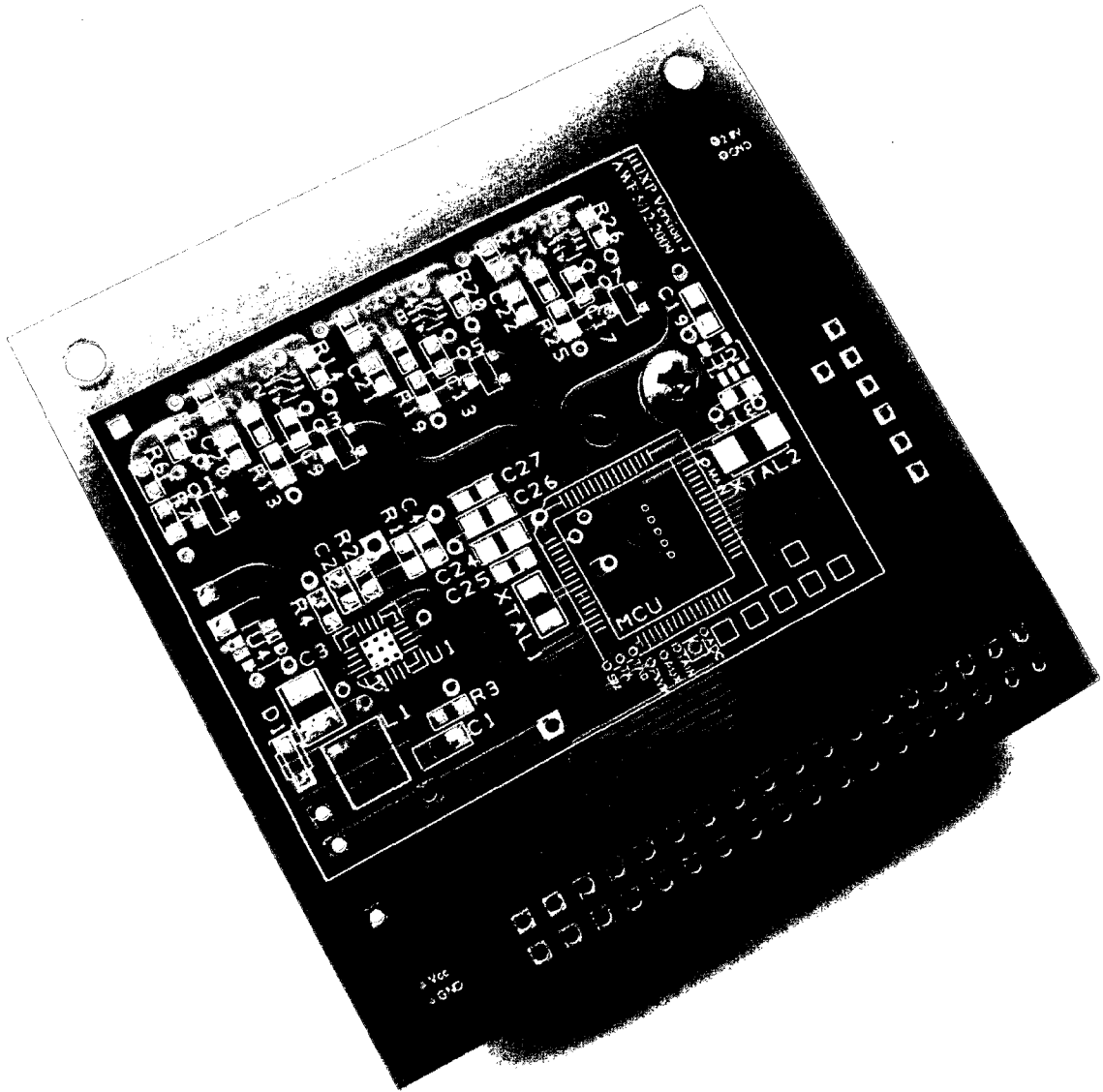


**Figure E.5: Top of the Fabricated PCB, Screw holding the Transducer Assembly**  
The top side of the fabricated PCB is shown. A #4-40 screw holds the transducer assembly in its place (on the other side of the board).

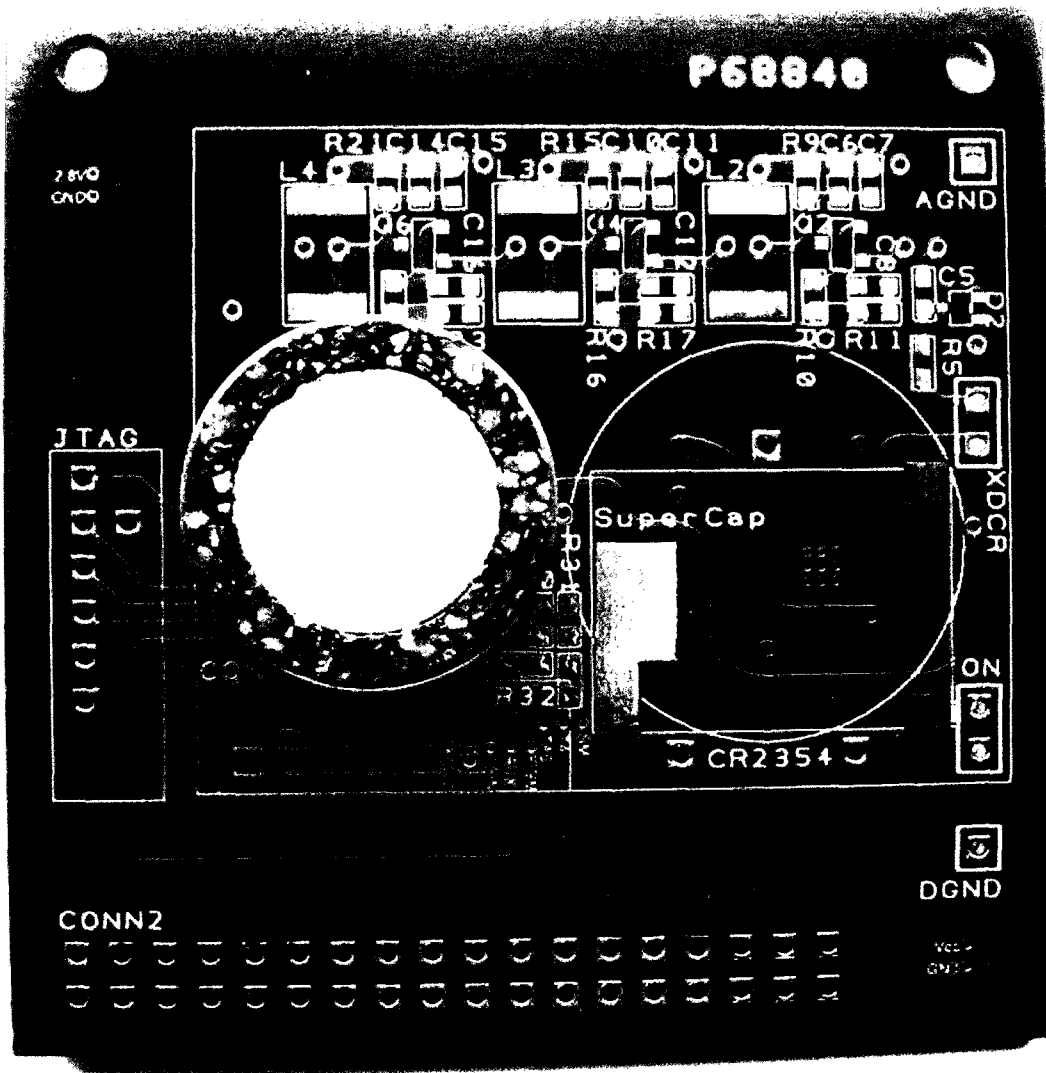


**Figure E.6: Bottom of the Fabricated PCB with Mounted Transducer Assembly**

The bottom side of the fabricated PCB is shown. Circuit elements are not populated on the PCB in this figure. The mounted transducer assembly is shown and represents the eventual position of the transducer (future work).